MST TECHNICAL DESIGN CONSIDERATIONS

R. N. Dexter
D.W. Kerst
T.W. Lovell
S.C. Prager
J.C. Sprott

PLP 965

December 1985

Plasma Studies

University of Wisconsin

Preface

The design of the MST (Madison Symmetric Torus) experiment is an ongoing process which began more than a year ago and will continue throughout the construction for several years. The project is predicated on a schedule which involves design and construction done in parallel, as made possible by the construction of various parts in series. This report describes considerations which have entered the design to date. All sections are necessarily incomplete and will evolve and change continuously as the design proceeds. The enclosed information should be interpreted accordingly. Concomitant with early documentation of this design information, is a rough appearance which includes unprofessional figures and imperfect phraseology; however, the technical content does accurately reflect the status and philosophy of the design at this point in time during the project.

MST Design Group

December 5, 1985

TABLE OF CONTENTS

MST TECHNICAL DESIGN CONSIDERATIONS

1. Introduction

1.1 Objectives

The primary objective of the MST (Madison Symmetric Torus) experiment, as described in detail in the original proposal, is to examine the effect of the boundary condition of the RFP on stability, fluctuations, sustainment, confinement and transport. The close-fitting conducting shell is believed to be essential to the very existence and sustainment of the RFP state through its role in stability and the dynamo effect. However, it also constitutes a major constraint on RFP reactor design. In order to achieve the objective of MST we have designed the device for expeditious exchange of the plasma boundary (shells of different thickness and spatial structure) and for easy diagnostic access for measurement of relevant quantities such as fluctuations. In order that comparison of plasmas bound by different shells be a valid exercise, it is necessary that the plasma physics not be dominated by extraneous effects; and to this end, we have taken into account the experience on the various RFP devices around the world to design a high quality device with minimal field errors, high cleanliness, up-to-date methods for voltage programming, gas-handling, and so on.

The second planned objective of MST, to be implemented later in the program, is to track stability and confinement as the plasma configuration is varied from RFP to non-reversed pinch to tokamak. Such a comparative study will enhance understanding of axisymmetric toroidal confinement in general, as well as the RFP in particular. This second objective has no impact on the engineering design presently undertaken since it only calls for an additional power supply to increase the toroidal magnetic field to attain the tokamak configuration. If this configuration scan were not proposed, the present design would remain the same.

1.2 Expected Parameters

Assuming a state-of-the-art approach to the many details that affect machine operation such as vacuum surface conditions and magnetic field errors, the machine performance will be determined primarily by its size (major and minor radius) and by the available volt-second swing of the iron core. Since our goal is not to test scaling laws or to achieve record parameters, we need only convince ourselves that for a range of plausible assumptions, the expected parameters are adequate for the proposed research. In this section we present our best estimate of the performance capability of the machine with a thick, 32-cm radius shell. In the next section we will examine plausible but more conjectural possibilities.

The electrical performance of the machine (plasma current waveform) has been deduced from an electrical circuit model similar to that used by Culham and Los Alamos and described in detail in section 3.4.1. The physics input to the model which is subject to debate is the plasma resistance (both during startup and in the flat top), the internal plasma inductance (as determined by the current density profile), and the coupling of the poloidal and toroidal field circuits through the plasma. In all cases, we have scaled geometrically from a 200 kA, ZT-40 discharge, assuming a modified Bessel function model with a similar current-density profile. The prediction is that the discharge will carry 400 kA for a nominal 40 msec duration. From the current and the size one deduces the plasma parameters from empirical scaling laws (T_e/I_p = const, β_p = const, $\tau/T_e^{3/2}a^2$ = const, $V_\ell a^2 T_e^{3/2}/I_p R_o$ = const), and the results are shown in Table 1.1.

1.3 Performance Limits

The ultimate machine performance would presumably occur for the no-shell case with a full a = 52 cm radius plasma. In this case the inductance is estimated to be 1.7 μH, and thus allowing 0.3 webers resistive loss during startup and ramp up, the ultimate current limit for our 2.0 volt-sec core is ~1 MA. For such a case, the current would be ramped up to its peak value in ~20 msec, whereupon the core would saturate, and the current would decay with the L/R time of the plasma which could be as long as 60 msec. If the empirical scaling laws continue to apply, one might then expect T_{eo} = 1 keV and τ_E = 20 msec.

TABLE 1.1

ESTIMATE OF RFP PLASMA PARAMETERS

Major radius:	R_o = 1.56 meters
Minor radius:	a = 0.32 meters
Toroidal plasma current:	I_p = 400 kA
Electron temperature:	T_{eo} = 400 eV
Electron density:	$n = 3 \times 10^{19}\ m^{-3}$
Confinement time:	τ_E = 2 msec
Plasma inductance:	L_p = 2.7 μH
Poloidal flux:	Φ = 1.1 volt-sec
Toroidal loop voltage:	V_ℓ = 20 volts
Nominal pulse length:	T = 40 msec
Average toroidal field:	$\langle B_\phi \rangle$ = 0.19 tesla
Toroidal field at wall:	$B_{\phi W}$ = -0.016 tesla

On the pessimistic side, if the plasma resistance were twice as high as predicted, corresponding approximately to no a^2/R_o enhancement over ZT-40, we would still expect to achieve 200 kA, 20 msec discharges with the a = 32 cm radius shell. Thus the volt-second limit in MST would be no more severe than the liner heat load limit in ZT-40, and we would have approximately the same range of plasma parameters available to us. We believe that such parameters would be adequate for carrying out the proposed research as described in the next section.

1.4 Expected Performance and Scientific Goals

There are two criteria which are generally used to determine whether an experiment of this nature will meet the scientific goals. The first is to evaluate parameters (usually dimensionless) which are believed at present to be important for the physical processes under study. The second is to require that the plasma parameters in an overall sense are competitive with present day devices and not pathological in any way that would render the results obsolete in the future. Both the expected parameters of section 1.2 and the worst-case parameters of section 1.3 meet these two criteria.

RFP phenomena are usually interpreted using resistive MHD theory. The dominant parameter of relevance is the magnetic Reynolds number $S = \tau_R/\tau_A$, the ratio of the resistive diffusion time to the Alfvén transit time. This number must be much greater than one for the relevant instabilities (such as tearing modes) to be manifest. Experience of those who run nonlinear MHD simulations of RFP dynamics

is generally that S must be at least 10^3 in order that the instabilities not be resistively damped. For both the expected and worst-case parameters S will be close to 10^5.

The other strict MHD requirement is that the discharge pulselength τ be long compared to a reconnection or resistive relaxation time, which is often believed to be the time scale for dynamo action. In expected and worst cases the pulselength is about two orders of magnitude greater than the reconnection time. It is also highly desirable that the pulselength be at least as long as the resistive diffusion time so that the dynamo will be evident. For the expected case the pulselength will be about twice τ_R. For the worst case τ is about $3\tau_R$, an improvement since as the temperature drops, τ_R also drops.

In terms of overall parameters, MST will be competitive with today's state-of-the-art RFP devices. Tokamak experience indicates that this level of parameters (multi-hundred eV temperature, multi-hundred kA current) provides physics information, particularly MHD physics, which remains relevant even in the presence of TFTR-scale experiments.

Thus, there is no doubt that the full range of parameter predictions allow the scientific studies to proceed; attainment of the expected case (400 kA for 40 msec) is not essential, and even the reasonably anticipated worst case (200 kA for 20 msec) will suffice.

It should finally be noted that the large vacuum vessel design allows the size, shape, position etc. of the plasma to be altered at a later date should new information favor a particular plasma type. This designed flexibility will guarantee the machine relevance in the future as new data unfold in the community.

1.5 Management Plan

A separate management plan for this project has been prepared, and this plan describes the administrative and technical responsibilities needed to maintain progress on the construction-phase experiments in the Levitated Octupole, on the MST design and fabrication, and costs and schedules. A detailed discussion need not be repeated here.

2. Technical Design of MST

2.1 Summary of Technical Design

The completed design for a plasma discharge chamber will be submitted to OFE and an OFE-sponsored design review team for approval before fabrication begins. This section is intended to summarize the major design problems, the solutions we have adopted, alternative schemes still being considered, and unresolved issues. More detailed discussion on each point will be found in subsequent sections. Section 2.2 completes the details of fabrication, and Sec. 3 provides details on considerations which influenced the design. In Sec. 3 we also describe facets of the operations and data acquisition in which the original proposal review team expressed interest or concern.

2.1.1 High-Voltage Startup and Gap-Protection Issues

The most serious questions relating to the design arise from the perception that for some period of time during the RFP startup, loop voltages up to the kilovolt level must be provided. In addition, sudden current termination may induce multi-kV loop voltages. While we still believe that low-voltage startup may be possible, the use of high voltage has been used as a design goal, and we hope, through construction phase experiments, to determine its necessity. In our design, voltage gaps are within the vacuum vessel; if plasma reaches an area of high voltage there is serious risk of arcing. Two alternative protection schemes are being explored:

(1) A continuous, non-vacuum liner formed of 0.01 inch stainless steel with tubulations insulated from the shells through which the plasma region is pumped via the vacuum containment vessel (VCV) - shell interspace. This solution would keep plasma from reaching voltage gaps, but assembly becomes complex, making multiple shell segmentation desirable. Initial proposed designs called for two toroidal segments. Our present proposal calls for six toroidal segments. This method has further attractive implications for gap protection. If the full loop voltage is divided across six gaps, the breakdown protection per gap is greatly simplified. If a loop voltage of 900 volts were reduced to 150 volts per gap, that would be well within the range of our successfully tested gap protection methods on Tokapole II.

(2) Multi-segmented shells without continuous liner form the alternative shell scheme which appears greatly preferable from the assembly/disassembly viewpoint. Since our proposal review we have taken a number of steps to become informed on protection of gaps in the presence of plasma. A sequence of gap-test experiments was initiated within Tokapole II, and an advanced gap protection design is being installed in the Levitated Octupole tank. While details are presented in later sections, we have concluded that advanced gap protectors combined with multiple shell segments to reduce the voltage per gap will provide a solution to the risk of gap arcs at high loop voltage without the use of a continuous liner.

Since we have approximately two years before a selection of a gap-protection and assembly scheme for shells must be made, we will continue to test gaps in Tokapole II, the Levitated Octupole tank, and with a "gap-tester" which has already been inserted for gap studies within the Tokapole II discharges, while at the same time exploring the possibility of low voltage startup in the construction-phase experiments. This is therefore an unresolved issue which will be subject to our continual scrutiny.

2.1.2 Field-Error Issues

A major design constraint has been that we would not knowingly incorporate a field error which would have a non-negligible effect on the plasma physics. In Sec. 3.3 we discuss field errors, and in Appendix III we discuss advanced field error considerations. This concern has brought us to include long toroidal gap flanges, poloidal gap flanges, overlapping shells, small pumpports into the shell, conductor-modified pump ports in the vacuum vessel, and provision for error-correcting feedback coils in the design. While most of these design features have significant additional cost, the success of the boundary study could be seriously compromised if we were incautious about field errors. We are not aware of any significant field error for which we have not included a first-line remedy. We estimate that owing to errors generated by the toroidal and poloidal field systems, the m=0 component of the radial error field will be 0.005% of the poloidal field at the reversal surface, yielding an island width of 1 mm, and at the worst point in the plasma (the poloidal gap) the error

field is less than 1%, producing a magnetic surface distortion less than 1 cm. These numbers are derived in Sec. 3.3 and will be refined as the calculations proceed.

2.1.3 General Fabrication Issues

Subject to constraints arising from the iron-core dimensions and the field-error issues, the proposed vacuum containment vessel (VCV) has several fabrication problems which are primarily cost-related, and unresolved at this time. Owing to our use of the VCV for both poloidal and toroidal currents and formation of a quasi-stationary flux plot, we have attempted to maintain a wall thickness of at least 5 cm. The bulk of aluminum involved creates serious fabrication difficulties. We found, in exploratory work with interested vendors, that aluminum billets of a size needed for a half-vessel could not be forged. This necessitated forming an alternative plan of welding billets to form a machinable form. Although spinning aluminum is a successful fabrication scheme, in general, we found no enthusiasm for spinning a half torus with a 5-cm wall thickness. We are reluctant to reduce the proposed wall thickness for long-range physics reasons; a time-changing flux plot which differed for each shell configuration might compromise the conclusions of the boundary study.

As a consequence of many discussions with scientists and engineers at many institutions and as a result of numerous plant trips to fabricators and visits by domestic and foreign vendors, we prepared a set of alternative drawings and submitted formal requests for quotation

(RFQ). It was and is our belief that several fabrication schemes will provide a VCV with the tolerances needed for all physics goals. It is useful to note that a common problem with all fabrication schemes is that many linear feet of vacuum-quality welding of aluminum will be required. These welds are also subject to important tolerances associated with the avoidance of field errors which could arise from large-scale defects which altered the current flow patterns within the VCV. Welding porosity can produce serious virtual leaks as well. Welding the large poloidal flanges used for reduction of field errors could produce distortions which would be difficult to remove or machine away, toroidal symmetry being destroyed upon welding of the flanges. We believe that all likely bidders found the ultimate tolerances to be reasonable.

2.1.4 First-Wall Issues

We will have a continuing concern with the first wall of the shelled RFP. A problem is that whatever solution we find for a thick-shelled case should also credibly apply for thinner-shelled boundaries, else the variations in RFP behavior in the boundary study might be subtle reflections of the solid state physics and not of the conductive properties of the shells. Issues related to limiter vs. armor plate vs. liner, heat dissipation, and localized energy deposition are explored in Sec. 3. There are serious and unresolved problems here which are shared within the entire RFP community. For our shell design we are maintaining two alternatives described in section 3.6. If we utilize no liner in the shell, installation of

graphite armor plate has several attractive features. Preliminary studies will be made within the Levitated Octupole tank. A visit to OHTE to investigate their experiences was very fruitful, and we gratefully acknowledge the gracious assistance of Dr. Tamano and his associates. It is our belief that the use of a full graphite armor is conservative in that wherever the plasma might strike the wall, on whatever day, or whatever shell, the properties of the first wall are more likely to be similar over the course of a series of experiments. It is further our belief, based on the most recent experiences reported in the RFP community, that the use of graphite armor plate does not prevent attaining parameters which would be acceptable for our studies.

2.1.5 Miscellaneous Issues

Our desire to interchange shells easily has generated problems owing to constraints by the limited space available and the large bulk of the iron core, VCV, and shells. Details of the area preparation and site constraints are provided below. Here it may be noted that the space problems have been understood by the administration of the Physics Department, and timely cooperation is being displayed. The problem of shifting the core-keeper and upper half of MST to expose the open lower half of the torus for shell insertion has been considered. No unresolved problems remain, but the detailed plans and cost estimates are fragmentary at this time.

The attainable performance parameters depend critically on the volt-sec capability of the iron-core. Expected and worst case scenarios were described in Sec. 1. It was essential to confirm that

we had not erred in our estimates of the volt-sec limit of the core. To this end we have estimated from published B-H curves, then measured, the properties of the iron core of the Levitated Octupole -- the core to be used for MST. The results, as described in Sec. 3.4.4 are in remarkable agreement, and imply that we can comfortably design around a 1.9 volt-sec flux swing. The resulting constraints are not burdensome for our project goals.

2.2 Mechanical Design and Fabrication

2.2.1 Toroidal Vacuum Containment Vessel Design

2.2.1.1 Assembly Features for Existing Iron Core

Use of the existing iron core imposed several constraints on the VCV design. Obviously, the core window imposed limits on both the major and minor radii of the VCV. Also the core window limits the sizes of poloidal and toroidal flanges. In order to readily remove the upper half of the VCV (for example prior to shell installation) the poloidal field system (primaries and continuity windings) will have to slip over the vertical legs of the iron core. Provision will have to be made to provide adequate clearance and alignment during this operation. A very careful measurement of the core has been made to assure maintenance of minimum tolerances in this regard. The toroidal field feed, described in Sec. 3.3, was also constrained by the presence of the core. For example, the length of the toroidal feed cylinders was limited by the core window. Additionally, the number of individual feed connections was selected as an optimization of field error

minimization and necessary clearance of the lower core leg and poloidal field system.

2.2.1.2 Vacuum Seals

The VCV will be sealed both toroidally and poloidally with flat viton gaskets (see Fig 2.2.1.2.1.). The design of the VCV gasket system is essentially an upgrade of the system used with success on the Tokapole II device. In the poloidal field gap and the inner toroidal gap the gasket also serves as an insulator. The viton gasket will be cut and assembled from commercially available sheet stock. The gasket strip will be epoxied into a groove in a G-10 plate forming an assembly that can be fastened (in the case of the toroidal gaps) to one of the flanges easing disassembly and assembly alignment. The gasket will be compressed by an array of insulated bolts, allowing sufficient uniform pressure to assure a seal. Just outside the sealing surface in all flanges are an array of 1/4" through holes. The primary purpose of these holes is to facilitate localized leak checking of the seal, however, they may also be used for sense coils to measure field errors. Where the toroidal and poloidal gaps cross is a potentially troublesome region calling for a "triple joint". Fortunately, we have had experience with such joints in the original Octupole, the Levitated Octupole and Tokapole II. While some refinement in the line of special methods for adjusting local squeezing pressure may well need to be incorporated into the seal design, we are confident that such a seal can be reliably made.

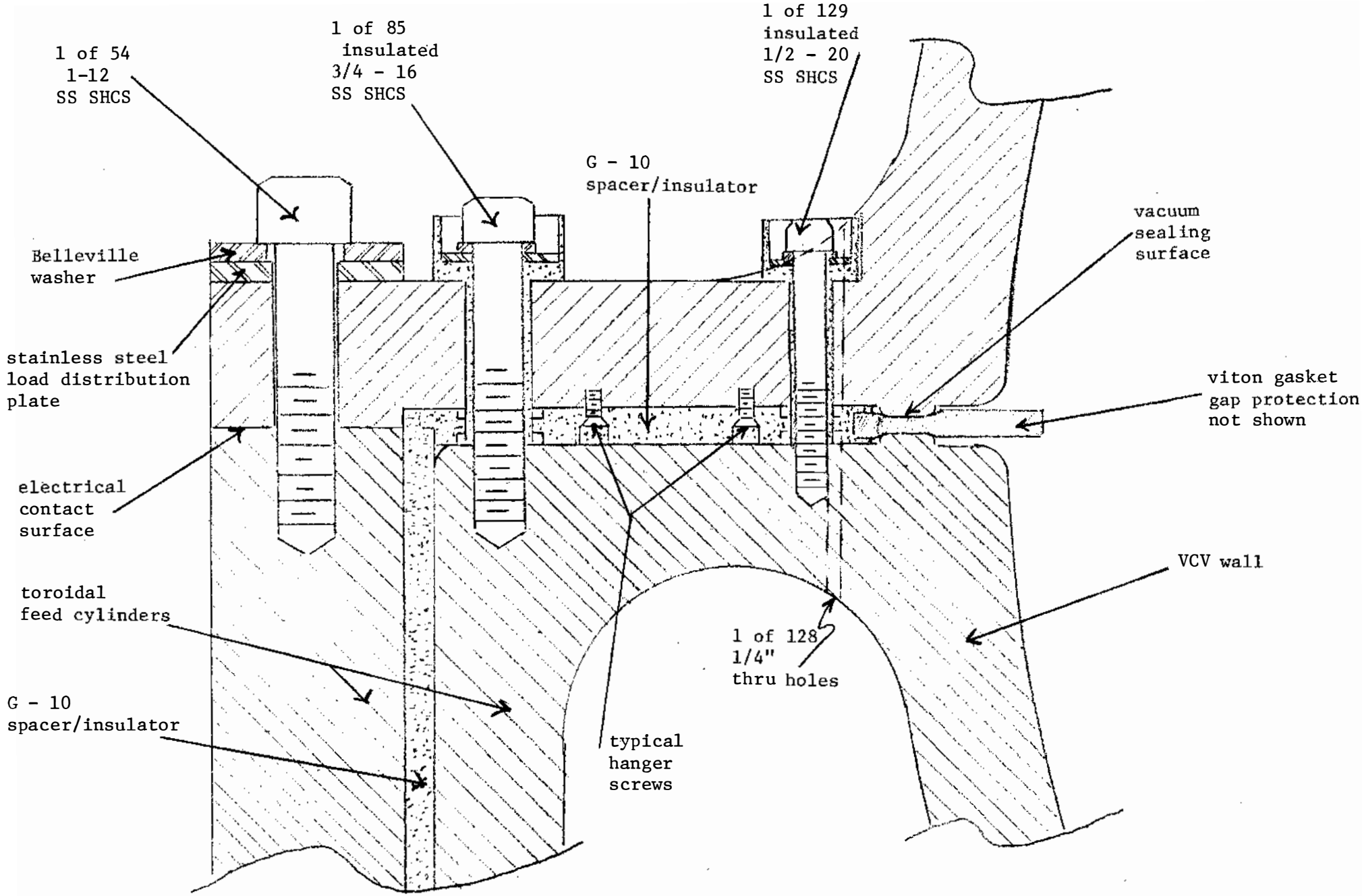

Note: 1", 3/4" and 1/2" SS SHCS thread into SS inserts

Fig. 2.2.1.2.1
Detail: inner toroidal feed flange and toroidal feed cylinder

2.2.1.3 Gap Protection

Even should we choose to use a continuous liner in the shell experimental series, the VCV gaps will require insulation and protection from the plasma. In the first year of operation we will not have a shell system installed, and the full poloidal field driving voltage will be exposed across the poloidal gap. As explained in section 3.8.6 we are engaged in a program of gap testing including the use of an advanced design in the construction phase experiments. Presumably a combination of gap design evolution and limiting of the plasma in the vicinity of the gap will be successful. This is a serious and primary concern, but we are moving forward in development of protection techniques. In addition to arc suppression, other constraints on gap protection design include requirements for disassembly along with the VCV halves and transition from poloidal to toroidal at the crossing points of the toroidal and poloidal gaps.

2.2.1.4 Provision for Stresses Under Normal and Fault Conditions

Investigations into the forces exerted by the fields under a number of operating conditions is well underway (see Figs. 2.2.1.4.1-2.2.1.4.8). A program of stress analysis, including computer modeling, will be undertaken as soon as the forces are all known. However the modest magnitudes of the forces thus far encountered reassures us that the heavy sections made necessary for electrical purposes will be more than adequate to resolve the mechanical forces. A special area of interest is the resolution of

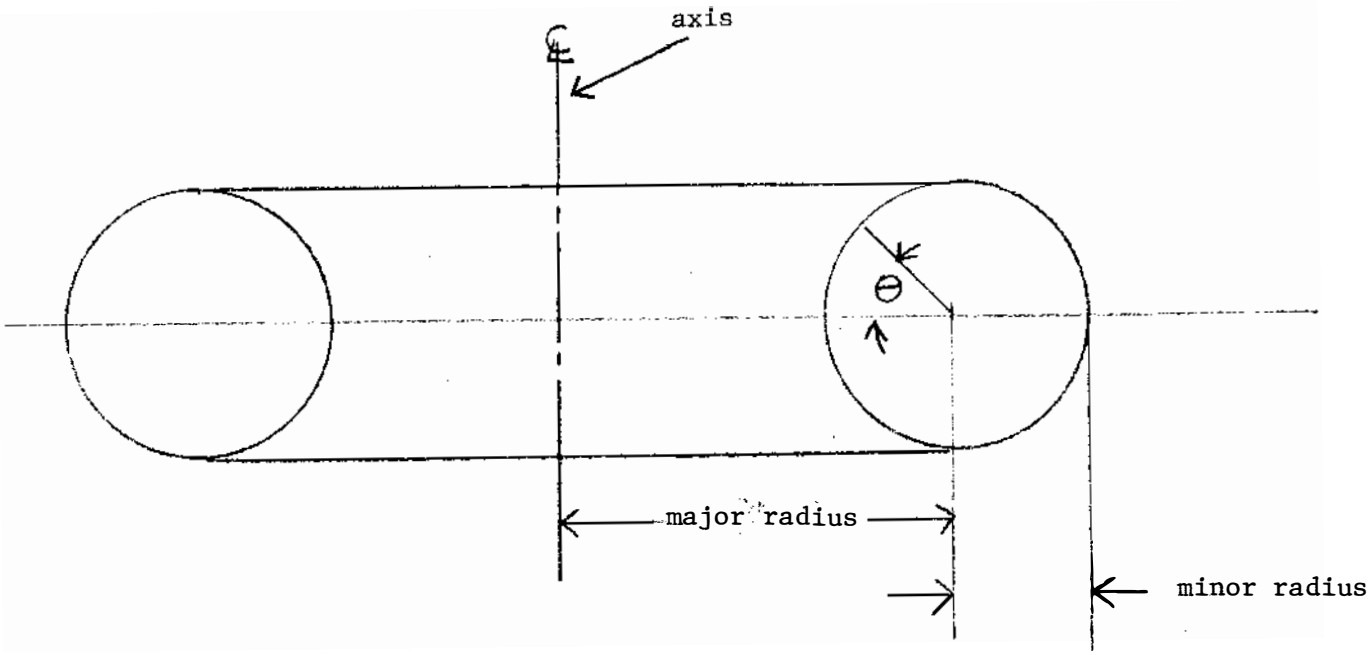

general nomenclature

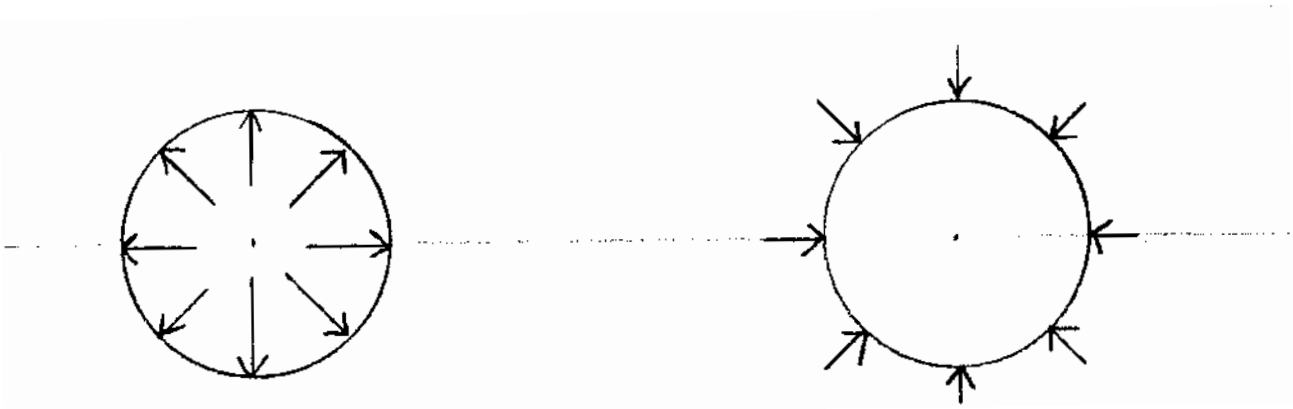

sense of positive pressure - VCV cases

sense of positive pressure - Linear cases

Fig. 2.2.1.4.1
Nomenclature

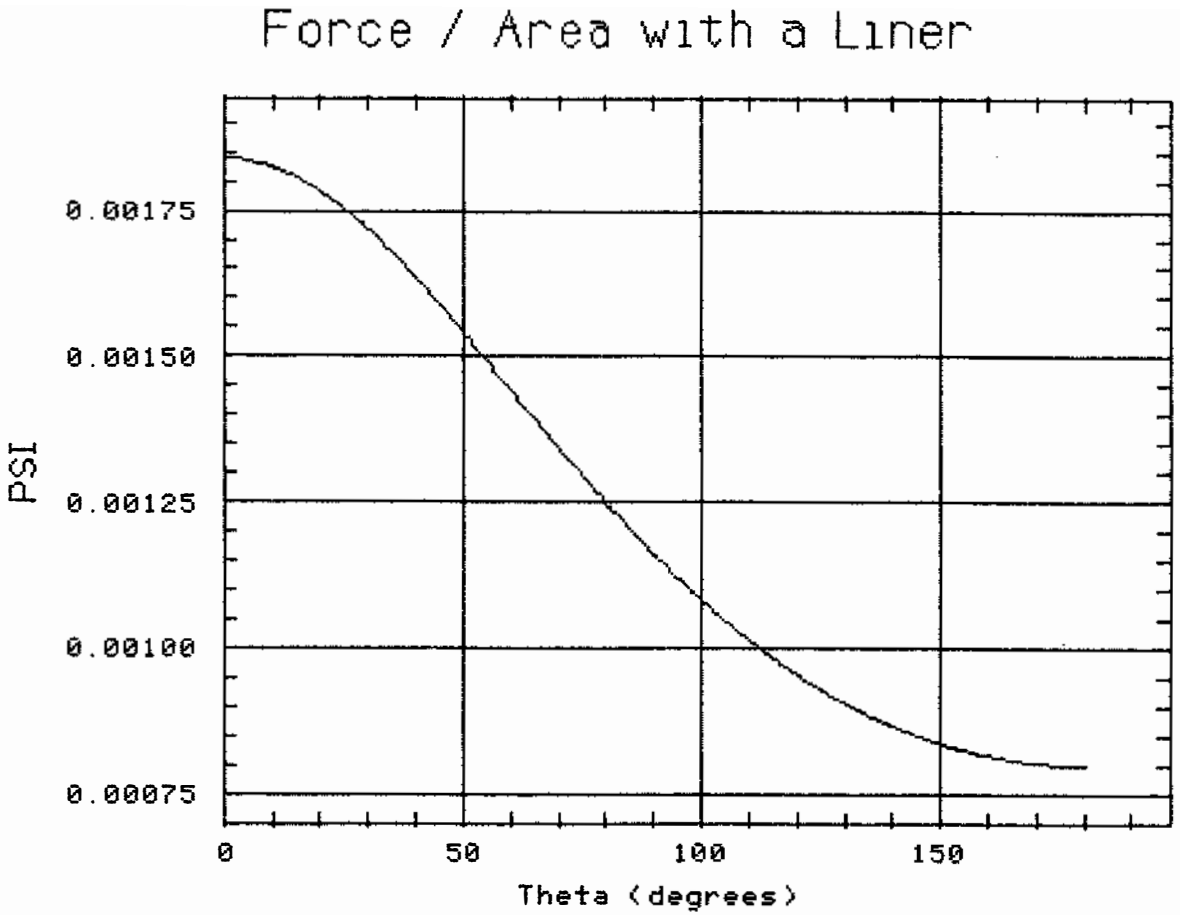

Fig. 2.2.1.4.2: Pressure on liner due to B_T field, no plasma, B_T at 1.56 m 500 g average pressure 0.001 psi, total force 38 lbs.

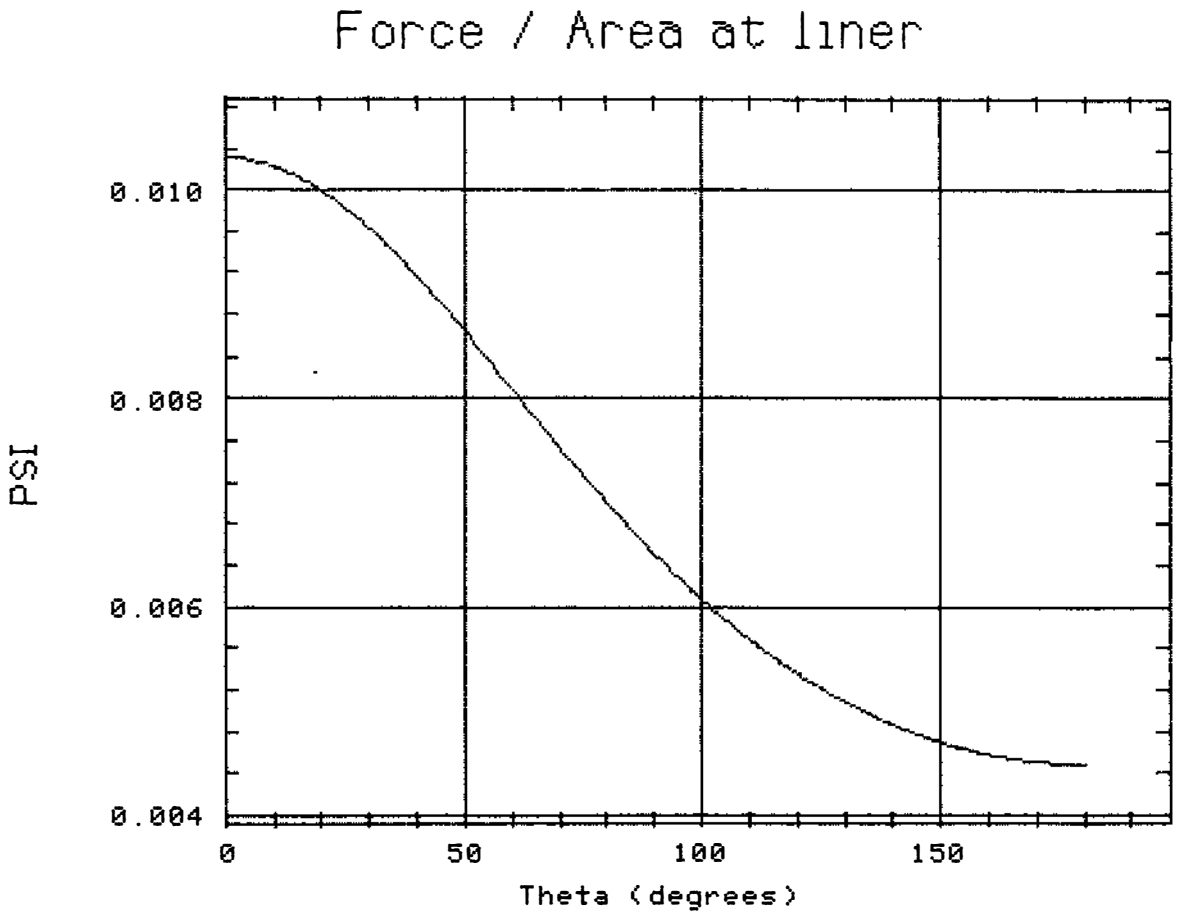

Fig. 2.2.1.4.3: Pressure on liner due to toroidal current, no plasma. Current 17 kA, average pressure 0.007 psi, total force 212 lbs.

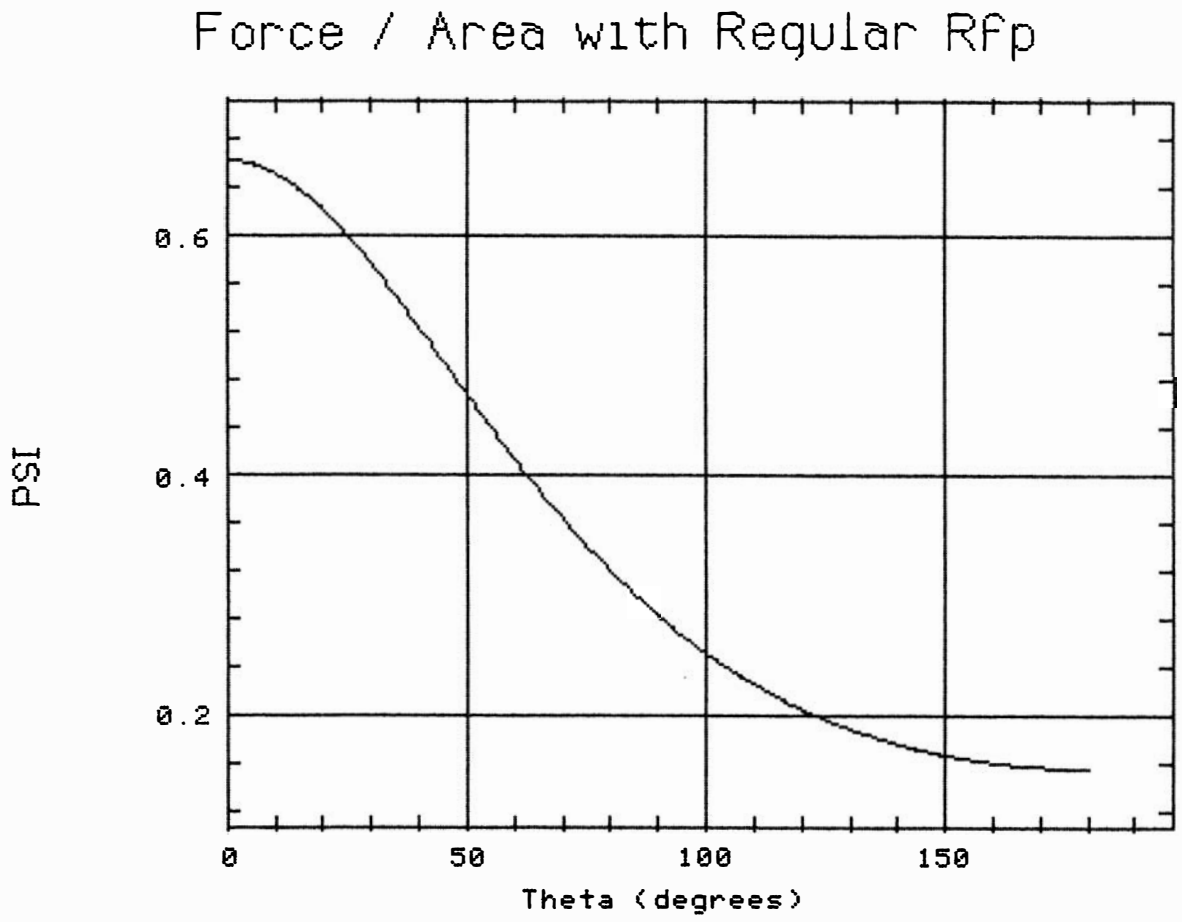

Fig. 2.2.1.4.4: Pressure on VCV due to B_T field for regular RFP parameters, no plasma. B_T at 1.9 m, 700 g, average force 0.34 psi, total force 1.6×10^4 lbs.

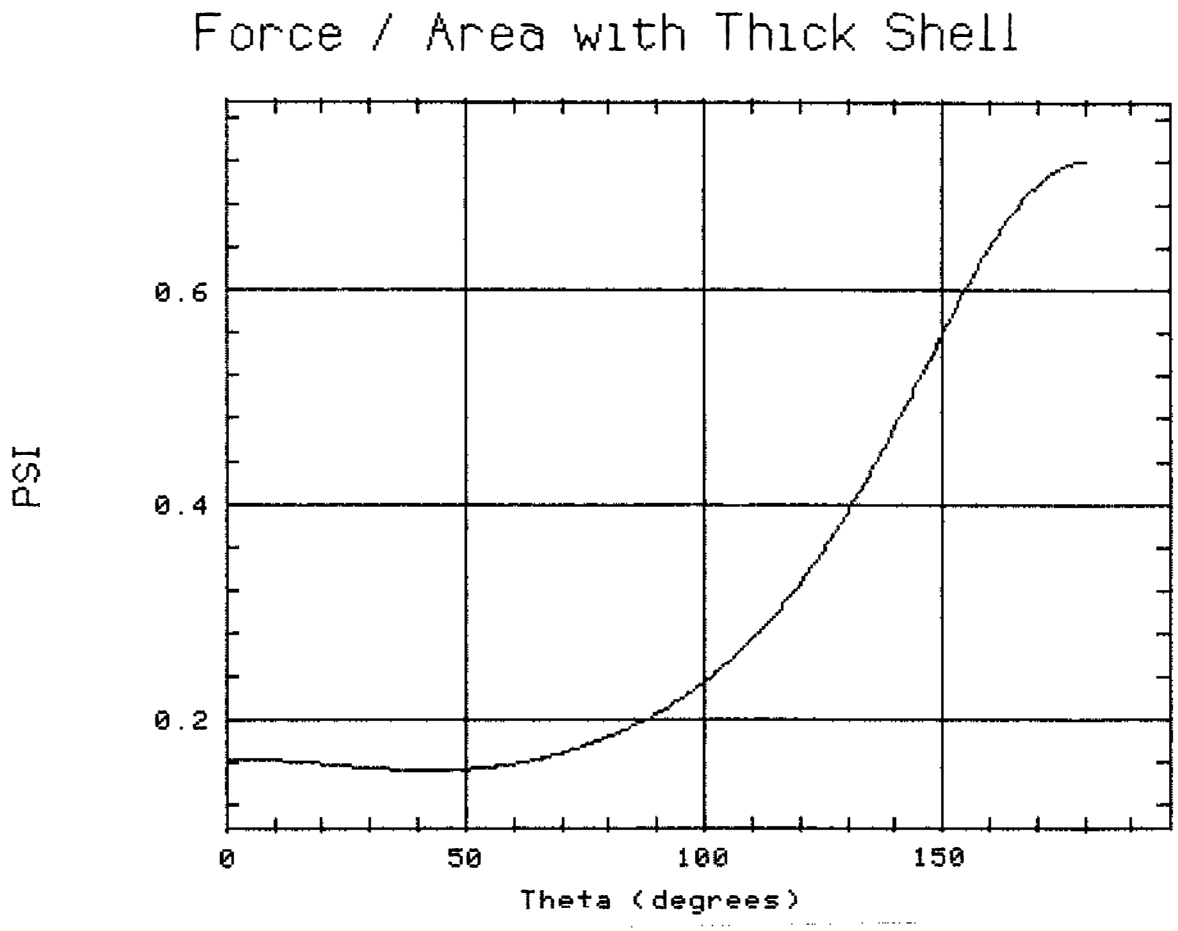

Fig. 2.2.1.4.5: Pressure on VCV due to poloidal current, thick shell system. Average force 0.3 psi, total force 1.5×10^4 lbs, total current 364 kA.

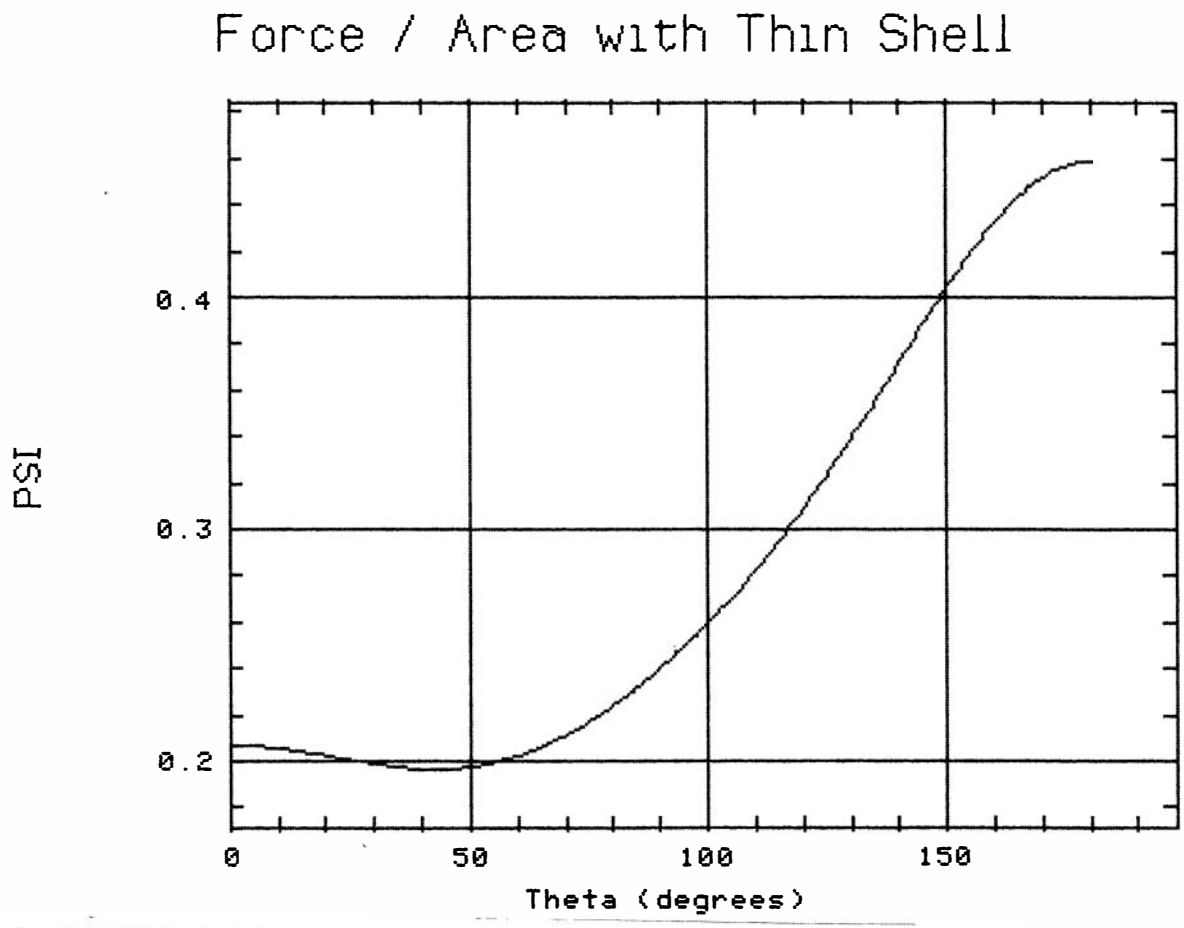

Fig. 2.2.1.4.6: Average pressure on VCV due to toroidal currents, thin shell system. Average pressure 0.25 psi, total force 1.3×10^4 lbs, total current 358 kA.

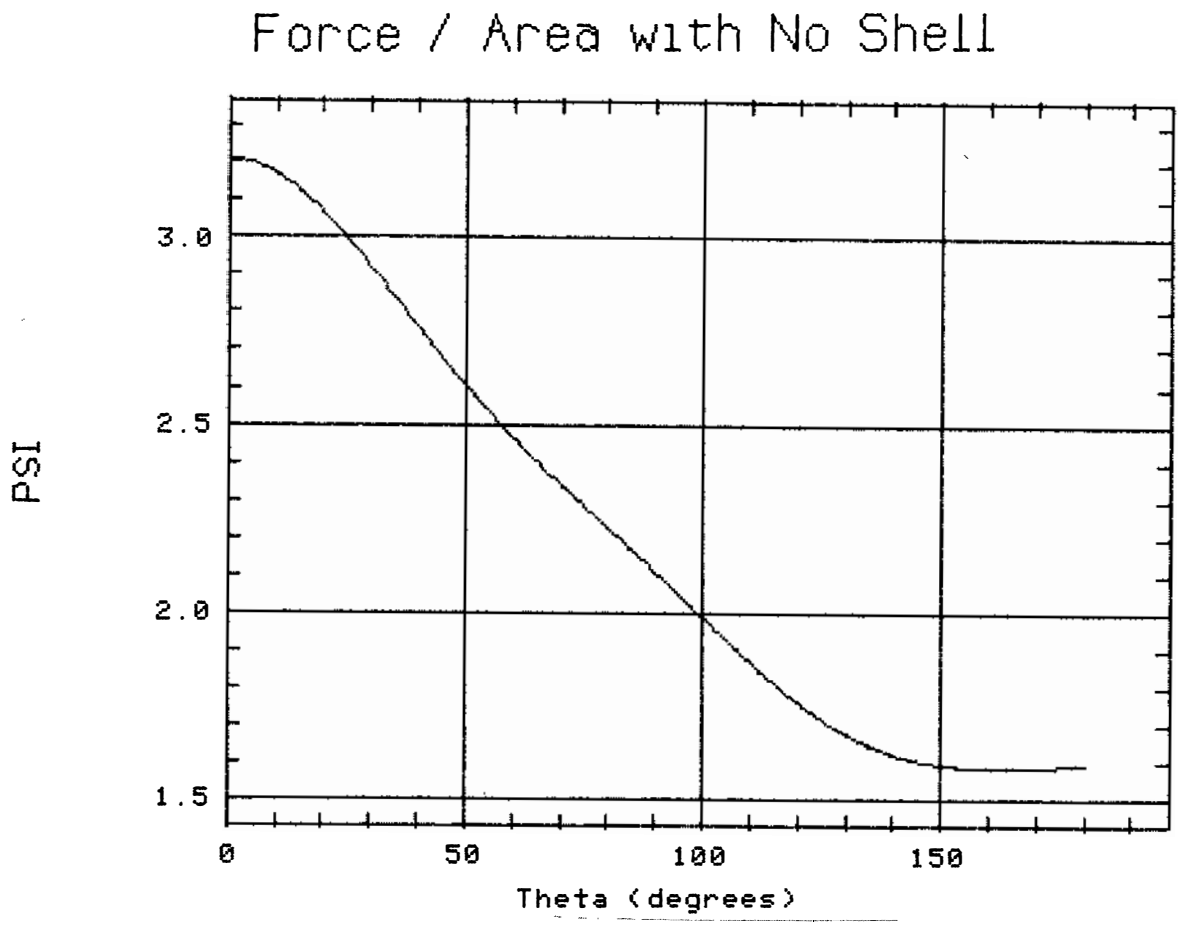

Fig. 2.2.1.4.7: Forces on VCV due to toroidal currents, no shell. Average force 2.2 psi, total force 1.1×10^5 lbs, total current 1.0×10^6 lbs.

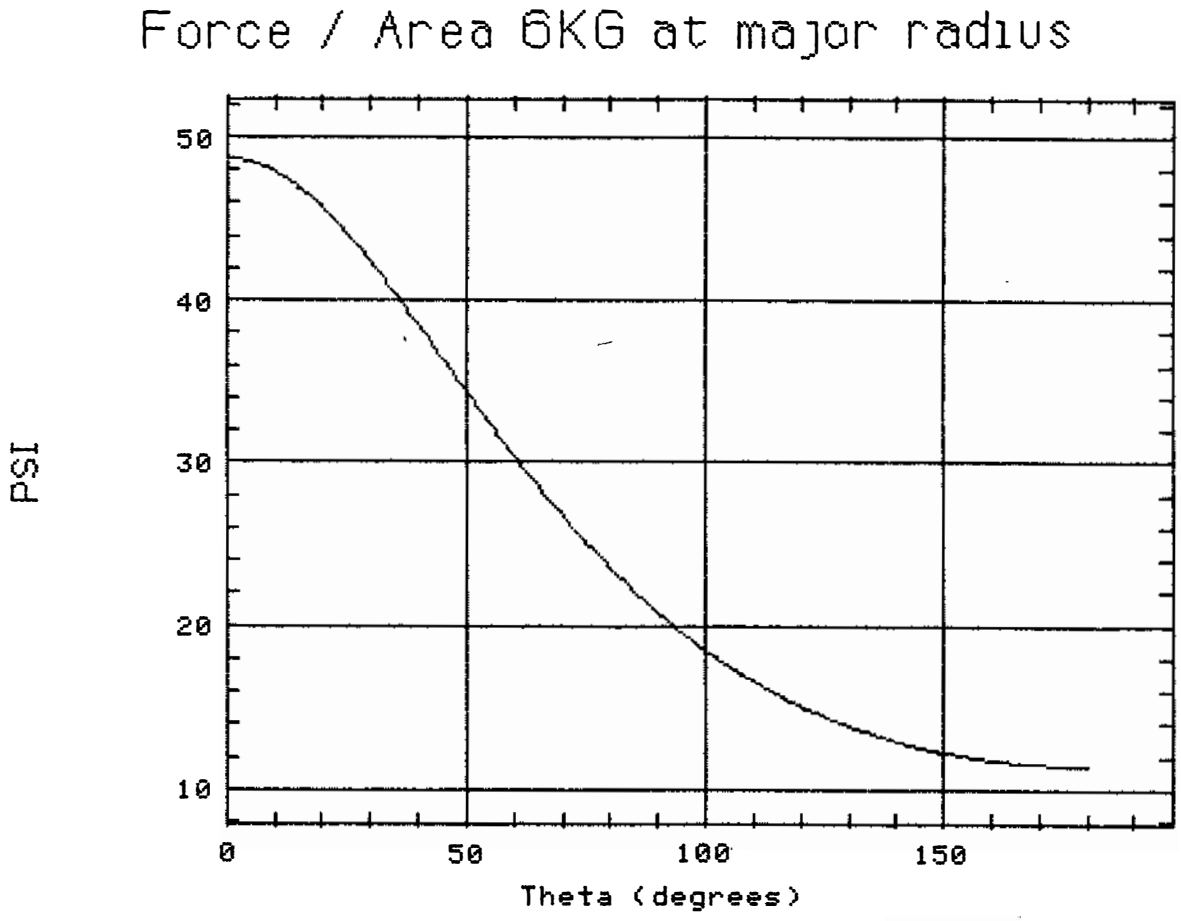

Fig. 2.2.1.4.8: Pressure on VCV due to 6 kg B_T at 1.5 m. Average pressure 25 psi, total force 1.2×10^6 lbs.

forces in the poloidal and toroidal flanges and feed cylinders (see Fig. 2.2.1.4.9). In addition to possible failure, flexure in these areas could lead to field errors and pulsed leaks. For this reason, all flanges and feed cylinders will be clamped with arrays of insulated tie bolts. Except for the middle row of bolts on the inner toroidal flange, these do not appear on present drawings since it was determined to be possible to add them at a later stage of fabrication, once appropriate numbers and location could be determined.

2.2.1.5 Incorporation of Tolerances from Field Error Considerations

While some of the tolerances in the VCV drawings stem from assembly, vacuum sealing surface, and electrical connection constraints, the tight tolerances in the gap regions are an effort to preclude errors in the field driving currents. It was calculated that the specified tolerances represented an optimal compromise of fabrication cost and field uniformity. Additionally, the G-10 plates previously mentioned as part of the gasket assemblies will provide positive spacing in the gap regions. Similar fiber glass spacing and insulation will be utilized in the feed cylinder gaps to enforce consistent spacing (see Fig. 2.2.1.2.1).

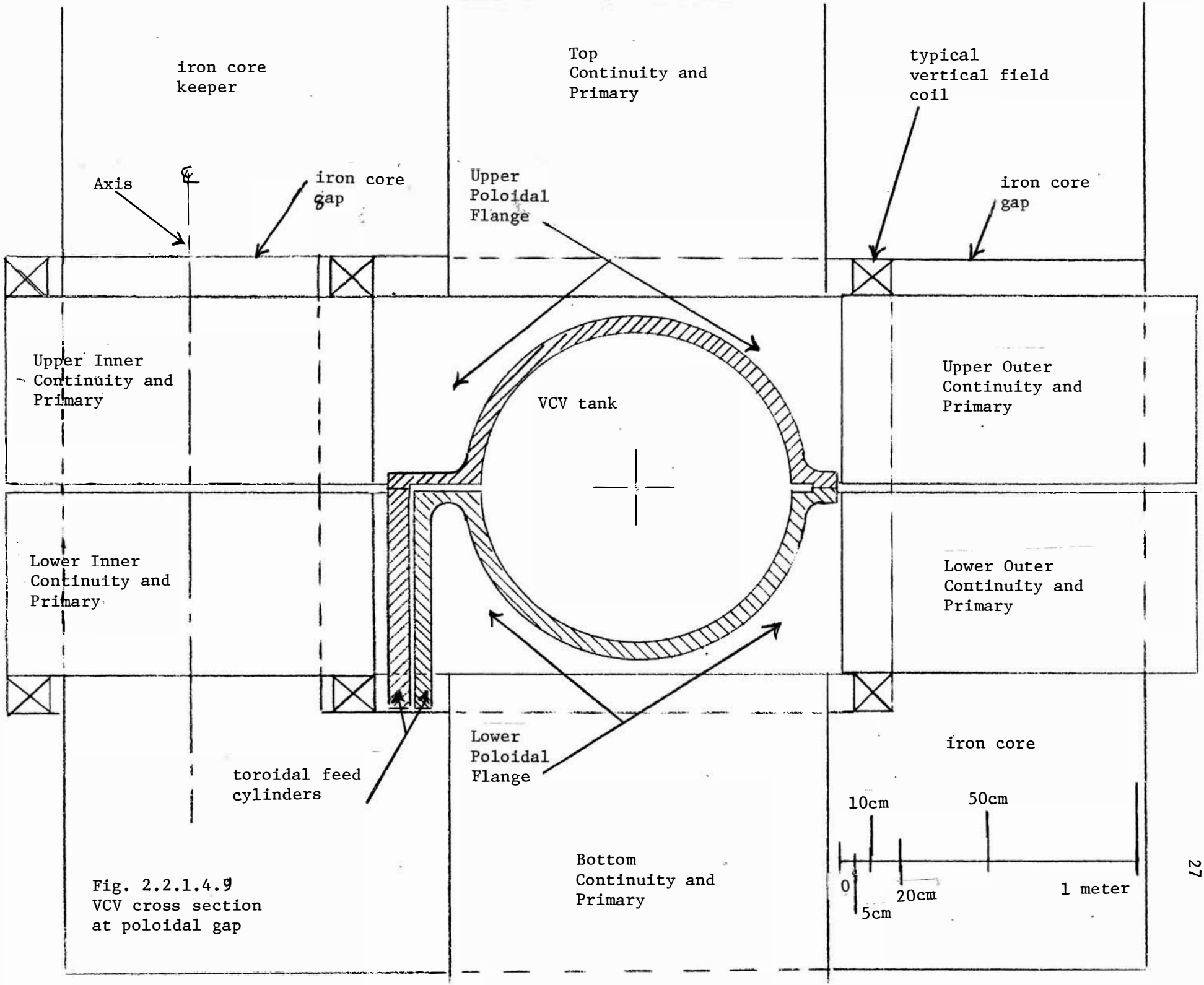

Fig. 2.2.1.4.9
VCV cross section
at poloidal gap

2.2.1.6 Mechanical and Electrical Properties of Poloidal and Toroidal Field Connections

As a general policy, most poloidal and toroidal field connections will be welded to prevent problems due to contact resistance variation (see Fig. 2.2.1.6.1). Several bolted joints are required, however, to facilitate disassembly. These have been designed to minimize current density and to maximize clamping force. The outer toroidal flange and the connection from the upper inner toroidal flange to the inner toroidal feed cylinder are examples of necessary bolted joints. Consequently they have been specified as having flat, well finished contact surfaces and an array of large clamping bolts. Clamping force will be maintained by the use of Belleville washers (see Fig. 2.2.1.2.1). Our experience has shown that successful aluminum-to-aluminum joints can be made provided the joint is prepared using Alcoa No. 2 compound. We will have clamping pressures of ~3500 psi which according to the Alcoa Bus Handbook should give a contact resistance of ~ 0.25 $\mu\Omega/cm^2$, but our experience has shown that aluminum/aluminum joints are often up to 10x worse. An innovative alternative that we are exploring is the fabrication of the appropriate parts from aluminum explosively clad with copper. This would result in a contact resistance of 0.5-1$\mu\Omega/cm^2$ and less trouble with joint preparation. Local contact resistance variations are shielded through the use of flanges between all such joints and the interior of the VCV.

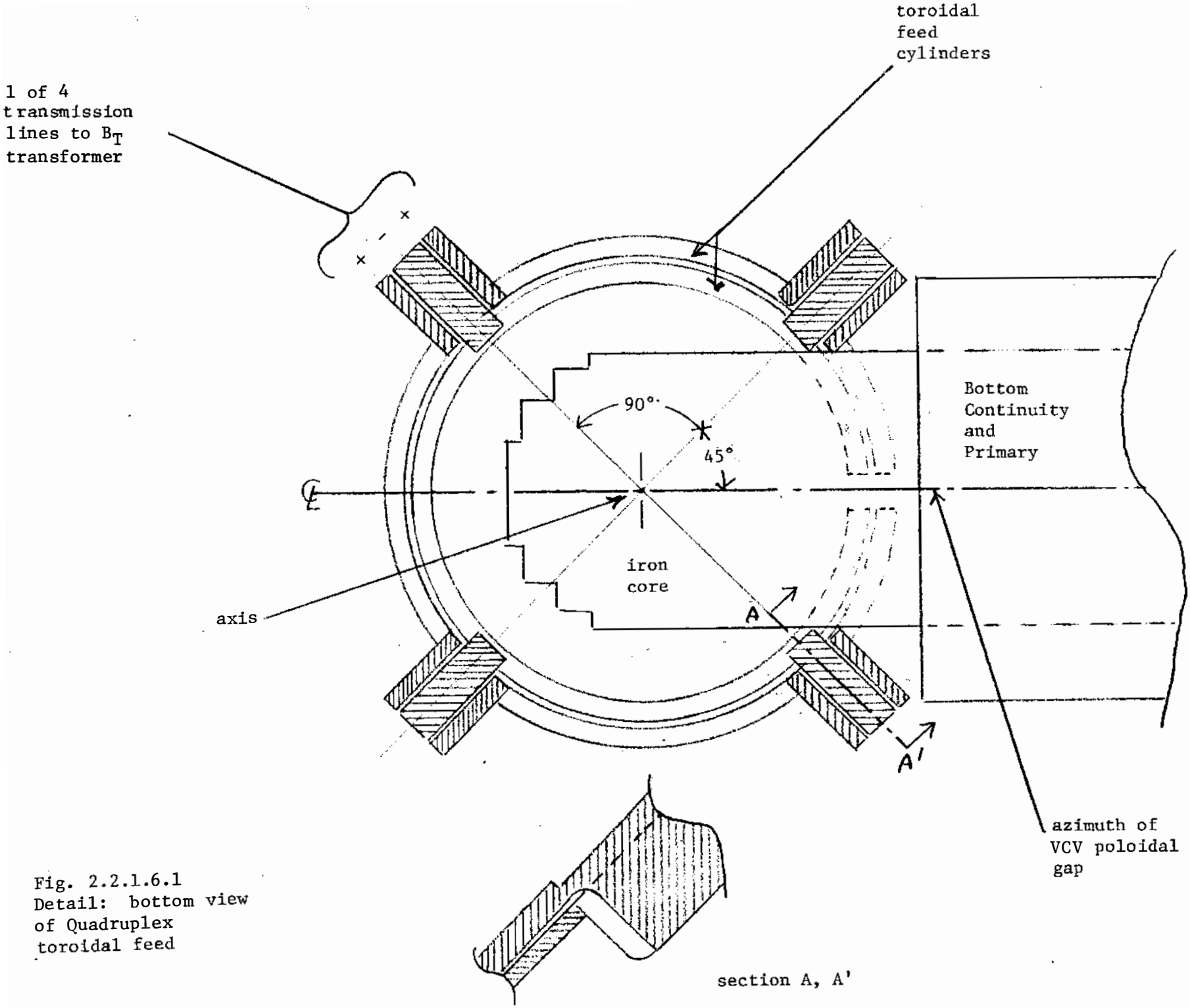

Fig. 2.2.1.6.1
Detail: bottom view
of Quadruplex
toroidal feed

2.2.1.7 Pump Holes and Diagnostic Ports

A major feature of this project is that a variety of shells, perhaps with liners, will be placed inside the VCV. Implications of this design feature are that the shells will be pumped out through a large number of small-diameter, line-of-sight holes. Inter-shell spaces will be pumped out with a larger number of smaller holes which are not in line-of-sight view of the plasma. The small holes are intended to reduce field errors but must be accurately aligned with apertures in the VCV used for probes or beam lines-of-sight into the plasma region. Troublesome features of these apertures for arc protection are discussed in Sec. 2.2.1.3 and 3.8. The line-of-sight apertures through the shell and VCV are machined subject to the complication that the shell axis is 6 cm outboard of the VCV symmetry axis. Vacuum vessel diagnostic portholes will be drilled through pointing towards the shell axis, or otherwise referenced to the shell axis, if chordal lines-of-sight, for example.

2.2.2 Vacuum Vessel Fabrication

2.2.2.1 Fabrication Methods

A survey of several fabricators revealed several acceptable schemes for the fabrication of the VCV. These schemes are indicated by the Request for Quotation document (Appendix V) and included drawings. This bid package was sent to 47 vendors, including five outside the U.S.

2.2.2.2 Selection of Method and Fabricator

Responses to our RFQ will be analyzed by a team from both the plasma group and PSL. Analysis criteria will include cost, time of delivery, and ability of responding fabricator. Additionally, any alternate fabrication proposal by any fabricator will be analyzed by the RFP Design Team for scientific suitability. If no responding fabricator can meet our criteria for the VCV assembly, PSL could, with the addition of a large vertical boring mill, fabricate the assembly from rough parts supplied by outside fabricators. The costs for this alternative are being prepared and will be compared with quotations for similar fabrication by outside fabricators. The close liaison we maintain with PSL would make this alternative appealing provided that costs are well defined.

2.2.2.3 Issuance of Purchase Order

Contingent on the release of funds by DOE based on the recommendations of the Design Review Committee, a purchase order for the selected fabrication will be issued as soon as possible. Since the bids have already been let, minimum delay can be expected in proceeding with fabrication.

2.2.3 Acceptance Tests

2.2.3.1 Design Acceptance

All design features and co-changes will be reviewed by the RFP Design Group and approved by the Principal Investigators, before being released for fabrication.

2.2.3.2 Preparation of Specifications and Drawings

All drawings and specifications for any part of the MST will be reviewed and approved by the Engineering Manager before being released for fabrication. This includes any supplemental material or changes.

2.2.3.3 Checking Against Specifications on Delivery by Outside Fabricators

As indicated in the attached quotation package (Appendix V) parts, subassemblies, and complete assemblies have been rather fully specified both by drawing tolerances and notations and by a document (the Request for Quotation). These specifications will be the basis for acceptance tests on all subcontracted fabrication. This will essentially be a two-part process. As indicated in the Request For Quotation, we are insisting on on-site liaison with any vendor making major parts. These personnel will not be authorized to provide final acceptance, but will be available to provide advisory opinions. This could reduce any problems due to misunderstandings. Final acceptance will be on delivery to PSL, including all the documentation specified in the RFQ.

Visual inspection, measurement, and review of the documentation will be made by a team of personnel from both PSL and UW Plasma Physics. Authorization for acceptance will only be made by the Engineering Manager.

2.2.3.4 Checking Against Specifications on Completion of PSL Fabrication

If PSL is engaged in fabrication of the VCV assembly from parts or subassemblies provided by outside fabricators, they will be subject to the same acceptance criteria as detailed in the RFQ. However, because of our close liaison with their operations, acceptance can be provided in a staged manner. Furthermore, it will be practical to institute a continuous quality assurance procedure consisting of regular visual inspection and measurement. However any authorization for acceptance will only be made by the Engineering Manager.

2.2.3.5 Acceptance of Finish Machining

It is our expectation that certain finishing operations such as port hole installation will be done at PSL no matter what scheme of fabrication is selected. Tolerances and other specifications will be indicated on approved drawings. These criteria will be checked by a team from the plasma physics group before initial assembly at PSL. Authorization for acceptance will only be made by the Engineering Manager.

2.2.3.6 Acceptance of Final Cleanup and Vacuum

It is expected that a final cleanup, assembly, and leak check will be made at PSL before shipment to Madison. This procedure will be supervised by personnel from the plasma physics group and carried out by a team from both plasma and PSL. Acceptance of this procedure will be authorized by the Engineering Manager only when a pressure of 2.0×10^{-7} Torr is achieved in the VCV and the tank is certified leak free to a sensitivity of 1×10^{-10} std cc/sec.

2.2.4 Area Preparation

2.2.4.1 Clearing Out the High Bay

RFP experiments will be performed in the Levitated Octupole tank for approximately two years. During this period, little area preparation can take place, and a tightly scheduled sequence of moves must occur. The Octupole must be decommissioned, and useful portions, such as pumps and valves, must be reserved. The second and third decks will be removed along with all electrical wiring and cabling. The data acquisition computer and all mobile apparatus associated with the plasma program will be removed from the High Bay. With the cooperation of the High Energy Physics Group the remainder of the High Bay will be emptied to permit entry of the movers. The High Bay must be kept open for approximately 6 months.

2.2.4.2 Removal of Levitated Octupole Tank

Movers will shift the 25-ton core-keeper to the floor and remove the four parts of the Levitated Octupole tank which will be preserved temporarily in storage with its original hoops and those optimized for construction-phase experiments; the continuity and primary windings being removed at this time.

2.2.4.3 Final Placement of Core

The core will be rotated, shifted, and elevated into the final position which will be determined by the many considerations discussed in Sec. 3.2.

2.2.4.4 Installation of Monorail for Core-Keeper Motions

The present core-keeper hoist is not suitable for the MST project since it does not permit clearing the core-keeper from full vertical access to the VCV. The 10-ton overhead crane is inadequate for core-keeper motions. The large vertical access of the High Bay does permit installation of a monorail crane which is to be supported near both load-bearing High Bay walls.

2.2.4.5 Installation of Columns for Core-Keeper Support

The orientation of the monorail will be established to permit translation of the core-keeper on the monorail tractor to a safe resting support formed of removable columns. The temporary resting place exposes the inside of the VCV since the upper half of the toroid will travel with the core-keeper. In this manner, access is optimized for installation of the various shells with which the boundary study are concerned.

2.2.4.6 Construction of Second Deck and False Floor

A full second deck will be installed at a height of approximately 8.5 feet off the floor, and at a height near the midplane of the MST. A false floor will be fitted (but not installed at this time) to clear the B_T core and transmission lines. The false floor will have an elevation of about 18 inches.

2.2.5 Delivery of MST

Since mechanical and vacuum testing of MST will be performed at PSL, the questions of delivery are very similar to actions which earlier took place when the Levitated Octupole was delivered from PSL and installed at the same location which MST will occupy.

2.2.6 Installation of MST

Many significant tasks in the installation of MST involving area preparation and subsystem development are included as tasks within the list of internal milestones shown in Appendix II.

2.2.7 First Shell Design

2.2.7.1 Resistive Liner

Should the continuous liner concept be chosen, such a liner could be fabricated from 0.010" stainless steel sheet segments welded together. Stainless steel would be selected for its strength, nonmagnetic properties, electrical resistivity, high temperature properties, and relative cost of fabrication. The thickness implies a penetration time of 70 μsec for the poloidal field and 330 μsec for the toroidal field. Such a liner would not have to support a vacuum, considerably simplifying its design. Assembly of the inner segments of a shell with vertical toroidal gaps would be difficult, but either deferring final welding of the liner until these segments are in place or using a pair of parallel rather than radial poloidal gaps would make this operation feasible. Table 2.2.7.1.1 summarizes some parameters of such a liner, Figs. 2.2.7.1.1 and 2.2.7.1.2 illustrate some features.

Table 2.2.7.1.1

MST Major Dimensions Summary

	VCV	OUTER SHELL	INNER SHELL	LINER	
RADII					
MAJOR	1.500	1.560	1.560	1.560	meters
MINOR					
INNER	0.520	0.365	0.330	0.320	"
OUTER	0.570	0.390	0.355	0.320254	"
THICKNESS	0.050	0.025	0.025	2.54x10-4	"
SURFACE AREA					
INSIDE	3.3754x10+1	2.2479x10+1	2.0323x10+1	1.9708x10+1	sq. m.
OUTSIDE	3.7932x10+1	2.4019x10+1	2.1863x10+1	1.9723x10+1	"
TOTAL	6.4547x10+1	4.6458x10+1	4.2187x10+1	3.9431x10+1	"
VOLUME	1.6137	0.5812	0.5273	5.0077x10-3	cu. m.
VOLUME ENCLOSED	8.0062	4.1024	3.3534	3.1532	"
MATERIAL	6061-T6 Al	6061-T6 Al	6061-T6 Al	Stainless Steel	
MASS	4.3731x10+3	1.5751x10+3	1.4291x10+3	4.0362x10+1	kg
HEAT CAPACITY	3.914x10+3	1.410x10+3	1.279x10+3	2.030x10+1	kJ/^{o}C
R toroidal	2.1908x10-7	6.5789x10-7	7.2512x10-7	1.3813x10-2	ohms
R poloidal	3.1043x10-8	3.9704x10-8	3.5827x10-8	5.9435x10-4	"
L toroidal				1.0x10-6	Henries
L poloidal	1.734x10-7			6.123x10-8	"
	1.513x10-7 w/ shell system				

Note: These figures neglect portholes, gaps, and flanges

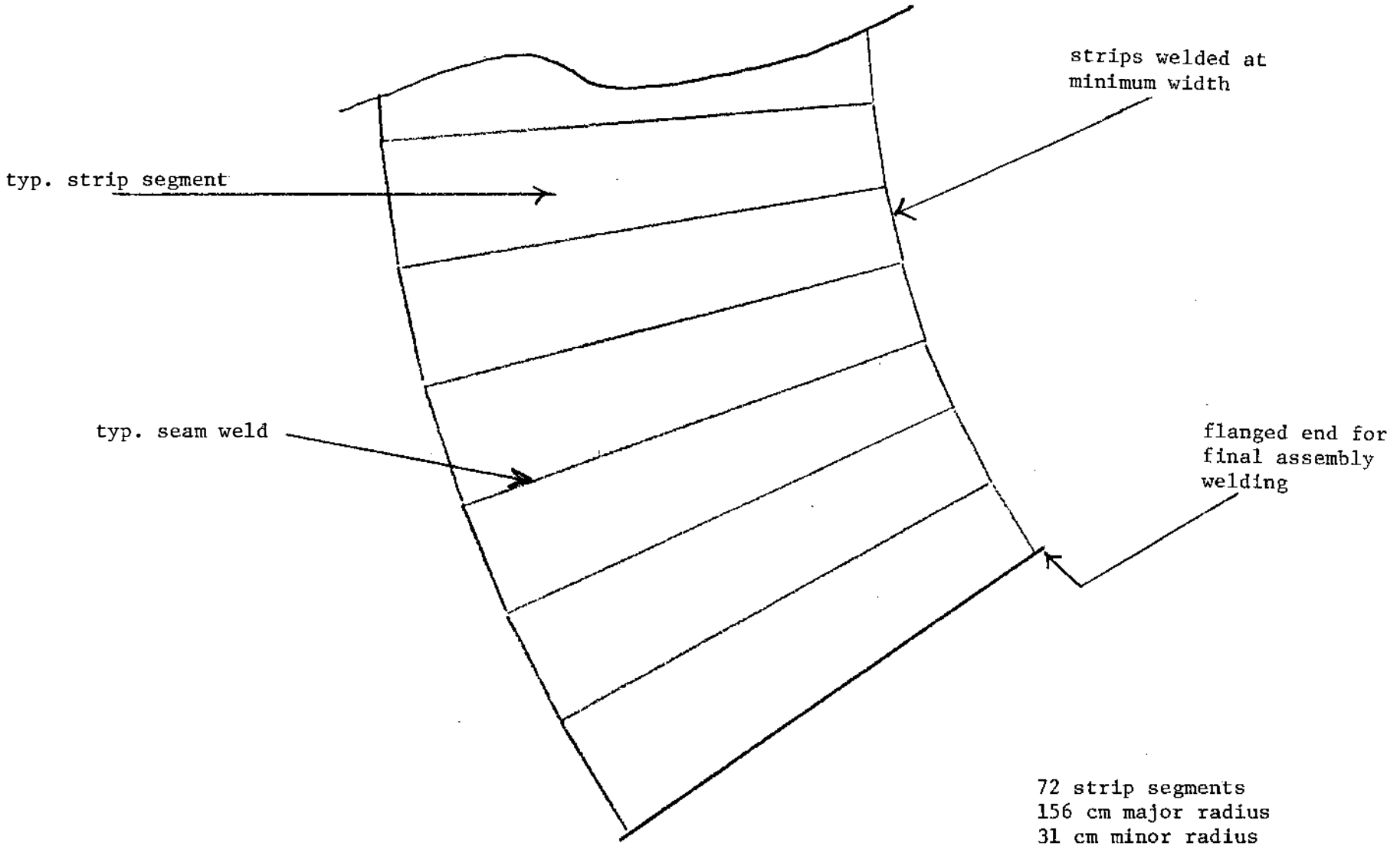

72 strip segments
156 cm major radius
31 cm minor radius
16.5 cm maximum width
10.74 cm minimum width
$\pm$.09 cm deviation from
radius
194.78 cm strip length

Fig. 2.2.7.1.1
development of
continuous liner
from flat strip

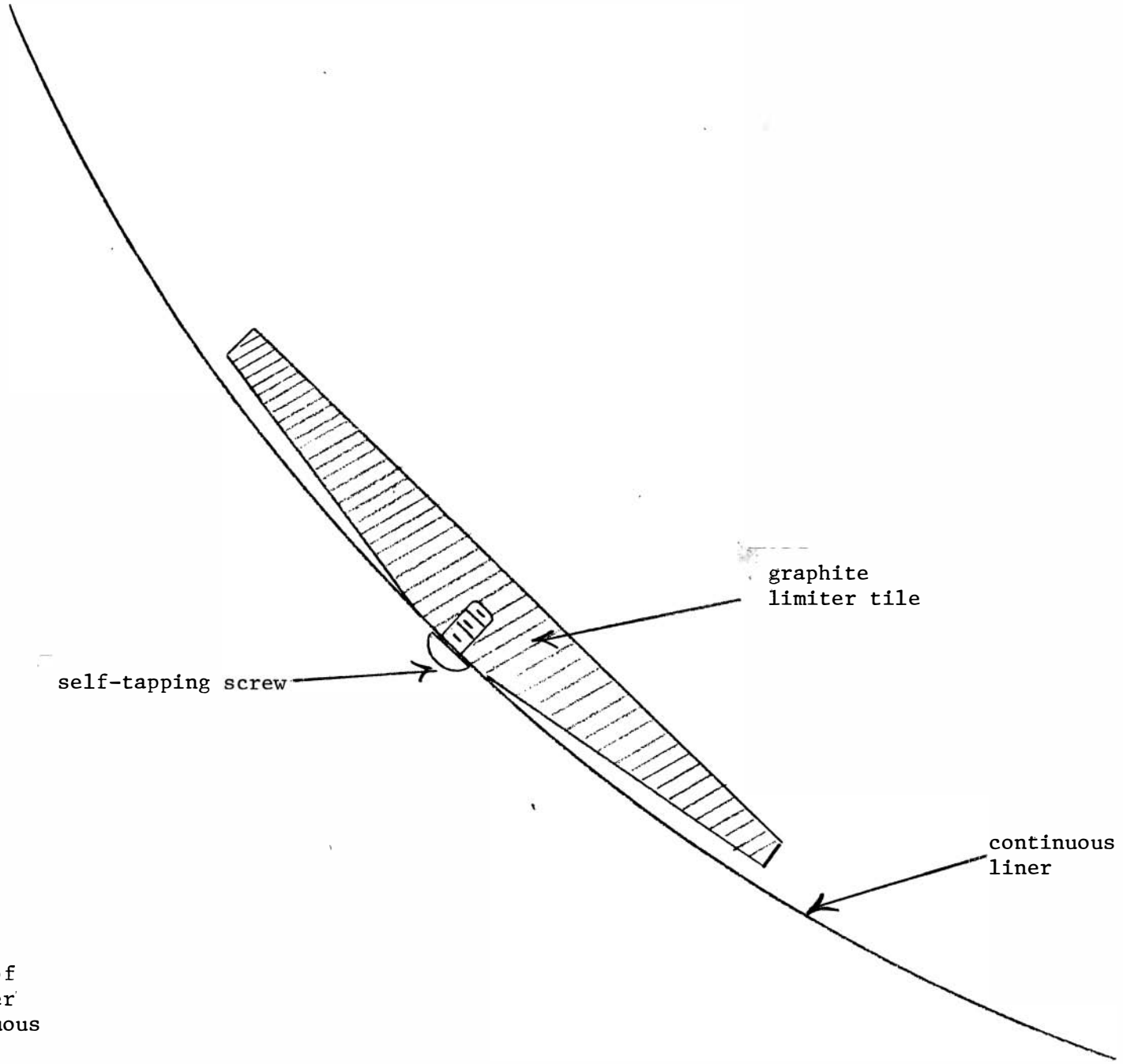

Fig. 2.2.7.1.2
typ. mounting of
graphite limiter
tile on continuous
liner

2.2.7.2 Overlapping Shell Concept

Our reference design (see Fig. 2.2.7.2.1) shows two separate coaxial shells with overlapping poloidal and toroidal gaps (see Fig. 2.2.7.2.2). As explained elsewhere the primary reason for this scheme is the reduction of field errors induced by gaps. In order to reduce the voltage on poloidal gaps, each shell is subdivided into six toroidal segments. In addition to gap voltage reduction, such a design will simplify fabrication and assembly. Some problems arise from the coaxial shell, overlapping gap concept however. Principal among these are shell-to-shell arcing and difficulty in pumping the intershell space. Computer simulations of the transient pressure behavior in such a system (see Sec. 3.9.7) have fortunately shown that it is possible to provide some pumping of the intershell space without the pressure rising significantly during a pulse. Each port hole in the shell system is provided with a stainless steel tube, close fitting to the inner shell and liner or first wall, and fitted with an insulating collar in the outer shell. Such a tube should be successful in preventing plasma and neutral gas from entering the intershell space. The simulation used 190 such tubes (34 - 3.18 cm dia, 98 - 2.54 cm dia, and 58 - 1.91 cm dia) 10 cm. long. This provided a 10,585 liter/second hydrogen pumping speed to the experimental volume. Additionally, the intershell space was pumped by an array of 192 .64cm-diameter holes in the outer shell with a pumping speed of 700 liters/second for hydrogen. The intershell pressure, presuming a base pressure in the 10-7 Torr region, barely rises into the 10-6 Torr region during the time of large voltages. Even if any microwave

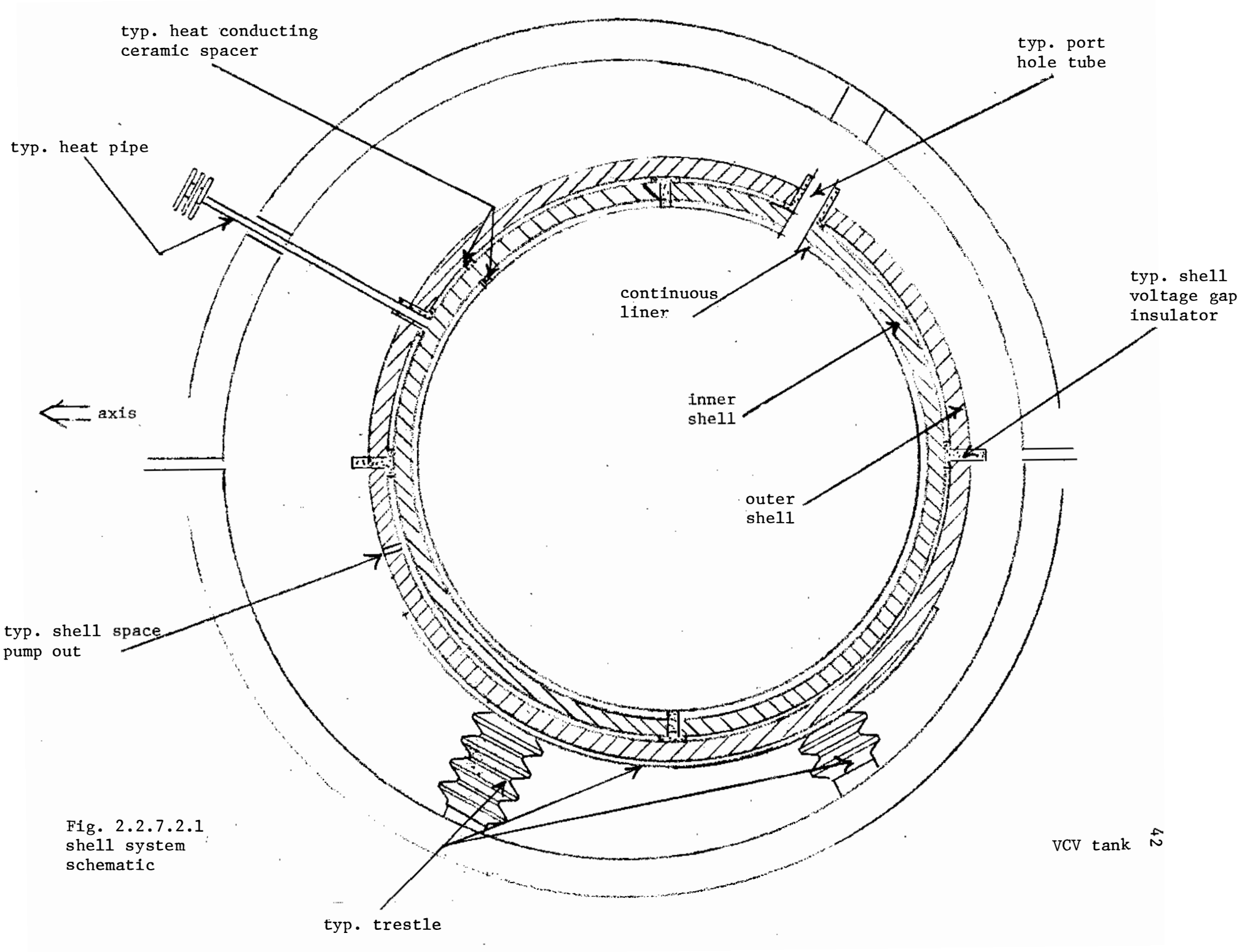

Fig. 2.2.7.2.1
shell system
schematic

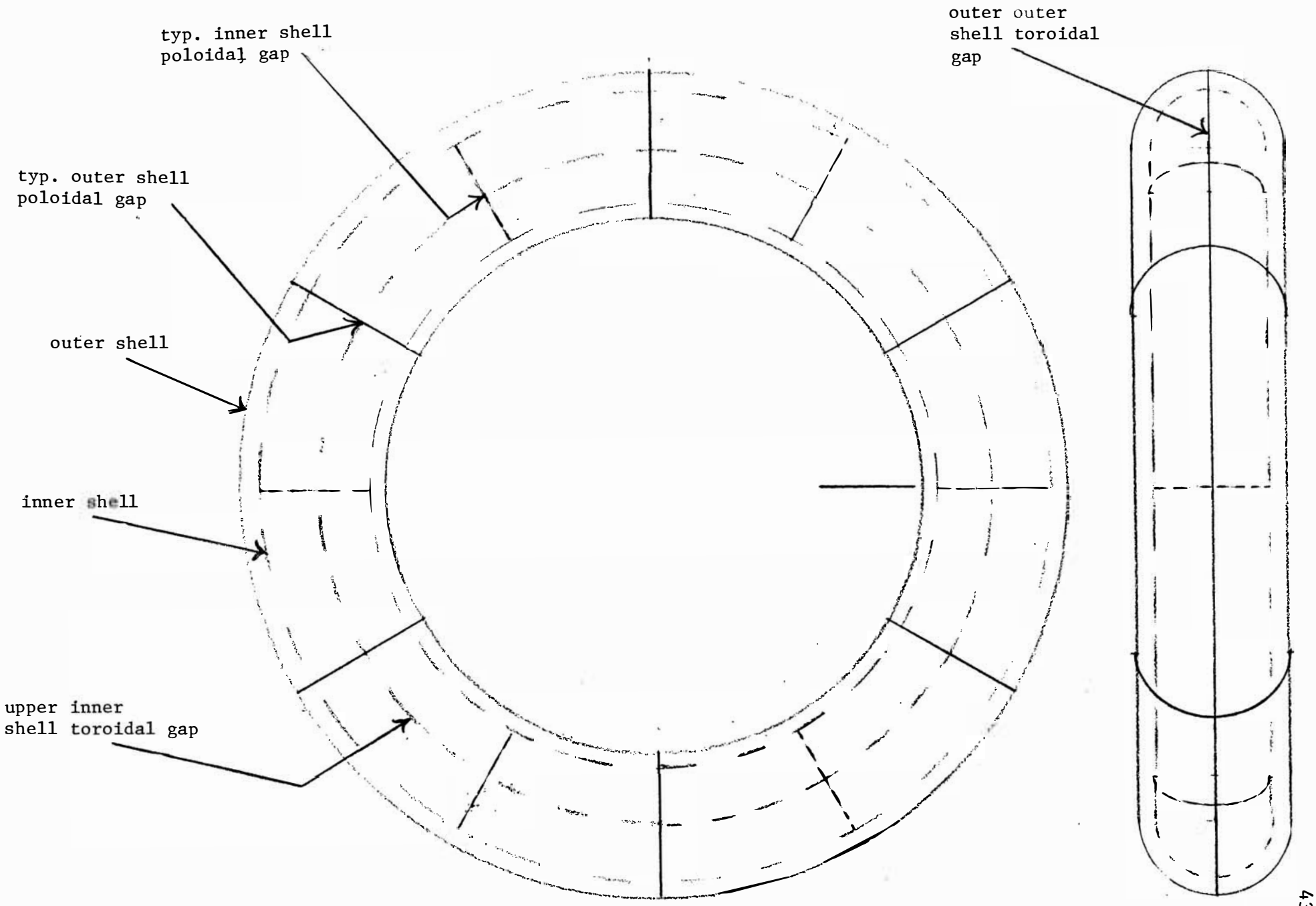

Fig. 2.2.7.2.2
shell system
gap layout

preionization were to find a resonance in the intershell region, this pressure is too low to cause serious problems. Another problem is maintaining electrostatic grounding of the shell segments. Electrostatic potentials might appear due to plasma losses or shell segment capacitive differences caused by diagnostic mounting.

Plasma loss charging current can be estimated by:

$$I_{\text{plasma loss}} = \frac{A_{\text{ports}}\, n_e\, V_{\text{plasma}}\, e}{A_{\text{liner inside surface}}\, \tau_e}$$

If $A_{\text{liner inside surface}} = 1.97 \times 10^5$ cm^2, $A_{\text{ports}} = 9.31 \times 10^2$ cm^2, $n_e = 3 \times 10^{13}$ cm^{-3}, $\tau_e = 2 \times 10^{-3}$ S, and $V_{\text{plasma}} = 2.96 \times 10^6$ cm^3, the $I_{\text{plasma loss}} \approx 34$ amperes or ~2.8 amperes/shell segment. The electrostatic grounding scheme must then be low enough impedance that these currents do not seriously change the shell segment potentials. One solution to this problem is to use a continuous liner or external resistors as a potentiometer to enforce the proper segment voltage distribution. Such a potentiometer could be grounded at one place to the VCV.

Heat deposited on the shell system by the plasma and eddy currents will have to be removed. As Table 2.2.7.1.1 shows, the shell system and liner have a large heat capacity, so the problem is reduced to providing cooling between plasma shots. At present this appears feasible through the use of heat-conducting electrically-insulating ceramic insulators to couple the shell segments thermally and heat

pipes to carry the heat out of the vacuum. Such a system would offer considerable simplicity and reliability when compared with the hazards and complications of running water cooling lines in the vacuum. Even in the absence of any conduction cooling, radiation will limit the average temperature difference between the liner and the wall to ~230°C, assuming 400 kJ/3 minutes = 2.2 kW and a surface emissivity of 0.1.

2.2.8 First Shell Fabrication

The method of fabrication of the first shell system will be selected through competitive bids and based on our experience in fabricating the VCV. Many of the methods, especially explosive forming, suggested for VCV fabrication would be very suitable for fabrication of shell segments. Final machining of segments will require a large vertical boring mill or a large CNC mill. PSL is presently engaged in acquiring a large CNC mill and may acquire a large vertical boring mill for VCV machining, consequently they will probably do the final machining. In any case, portholes and other details will be added by PSL, as well as fabricating the anticipated shell system assembly jig. An initial assembly of the shell system will be made at PSL before shipment to Madison.

2.2.9 First Shell Acceptance and Delivery

Tolerances and specifications for the first shell system will be developed in a manner very similar to those for the VCV. Acceptance procedures and criteria will also be similar.

3. Other Issues

3.1 Stress Analysis

3.1.1 Stresses Without Plasma or Currents

These are atmospheric pressure stresses on the VCV. A sample estimate of these stresses yields a maximum meridional stress of 219 psi and a maximum hoop stress of 84 psi with a maximum deflection of 0.003". This is a preliminary estimate based on a simple closed toroid and does not include any bending stresses in flanges etc. Obviously, it is clearly within the compressive yield strength of 6061T-6 aluminum (~35K psi).

3.1.2 Stresses With Currents

Forces for a number of conditions were shown in Figs. 2.2.1.4.2-2.2.1.4.8. One condition not yet analyzed for forces is possible field gradients across shell segments since plasma magnetic surfaces are slightly elliptical and the shells are circular. Careful analysis of all stresses is not complete.

3.1.3 Stresses During Disruptions or Arcs

Low impedance arcs of all the shell gaps would create a force on the shell system. This force might not easily be resolved by any practical trestle, and these faults must be avoided. Higher impedance arcs and partial arcs are being studied, and design features such as

insulated strapping around shell systems may be adequate. Based on reported Los Alamos ZT-40 results one of the primary problems with a plasma disruption may be enhanced gap voltages due to the large dI/dt. Our internal liner would limit the voltage during an instantaneous current termination of a 400 kA discharge to 5600 volts. There also may be large gradients in the magnetic fields across the shell segments.

3.2 Site Layout

3.2.1 Constraints by Magnetic Core Properties

The existing iron core will be incorporated into the MST, and it dominates the layout. It blocks nearly 60^{o} toroidal access, its window constrains the torus parameters, and, in addition, its position must be established in the limited space so that there is adequate diagnostic and operations access while preserving the overhead crane for moving shells in and out of the vacuum vessel. Further, since a major part of this project depends on convenient interchange of shells, the core keeper must be lifted and translated sufficiently to completely clear vertical access to the vacuum vessel. The core and keeper size then specifies a siting differing from that used for the Levitated Octupole in the same general area. The overall exploded layout is illustrated in Fig. 3.2.1.1 where the core and top half of the VCV have been lifted and translated. The new core for the toroidal field will be placed below the MST requiring that its elevation be raised by about 18 inches from its present height.

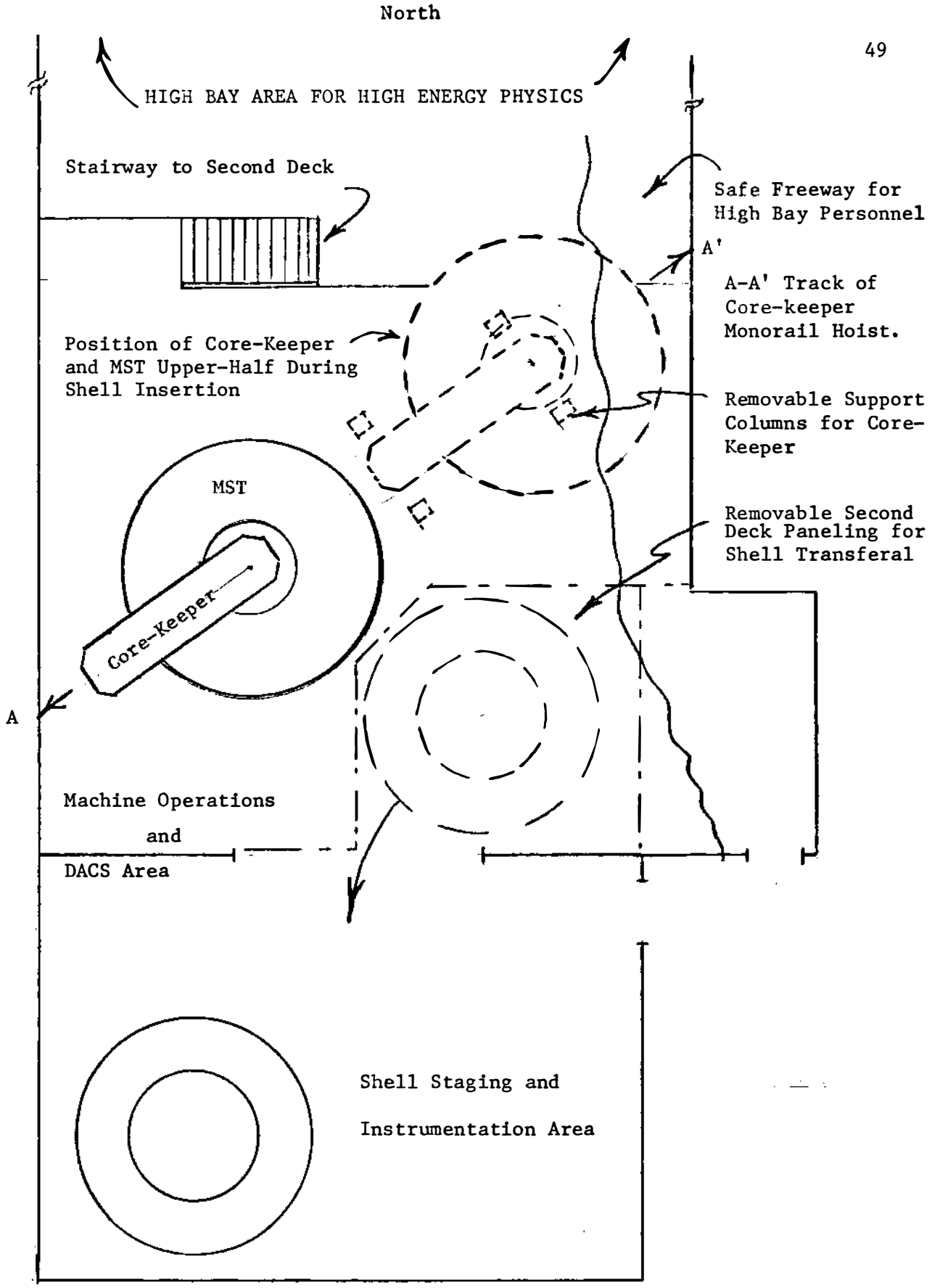

Fig. 3.2.1.1. Exploded View of MST in High Bay.

3.2.2 Layout of Capacitor Banks and Transmission Lines

The capacitor banks are already in place and used in versatile fashion for Tokapole II and the Levitated Octupole. The banks do not constrain the siting, but the transmission lines must be reconstructed and relocated. These considerations place no significant burden on the site layout.

3.2.3 Constraints for Diagnostics, Pumps, and Shared High-Bay Facility

Owing to the limited floor-plan space available in the High Bay, the requirements for displacing the core-keeper make it essential to plan the diagnostic port locations early in the design. Similarly the operator and computer areas are limited. Continuing the tradition on the Levitated Octupole, a second deck will be constructed as depicted in Fig. 3.2.1.1. The shared 7-1/2 ton overhead crane is adequate for all shell interchanges, but the new core-keeper hoist and tractor must be kept below the pulleys and tractor of the overhead crane. The hoist elevation vertically clears the height of persons on the second deck. Many parts of diagnostic apparatus and assorted power supplies will be installed on the second deck.

3.2.4 Layout of Operator Area, Data-Acquisition Computer, and Control Area

The entry to the High Bay area is shared with other research groups, and a high traffic region results. Requirements for personnel safety during operation confine the traffic to the east wall and the

iron core as far to the west as possible. The operator area, bank charging controllers, timing panel, and operations monitoring computer are thereby placed as in Fig. 3.2.1.1. The data acquisition computer is then finally placed as shown; a satisfactory layout is achieved despite many constraints.

3.3 Magnetic Field Errors

3.3.1. Field Error Criteria

The presence of nonaxisymmetric radial magnetic field within the plasma has two well-recognized effects harmful to magnetic confinement, namely, the breakup of magnetic surfaces into islands and the production of localized bumps in the outermost surface leading to local plasma-wall interaction. Below we briefly describe the criteria employed to determine the field error amplitude and spectrum acceptable in the machine design.

Beyond these two major concerns, field errors may produce other problems; for example, a gap may create an additional field error in the presence of a helically kinked plasma column or it may initiate an instability in an otherwise stable plasma. These effects are discussed in Appendix III.

3.3.1.1 Magnetic Islands

For a low-q toroidal device the radial width of an island is given by

$$\Delta r = 4 \left(\frac{B_r}{B_p} \frac{r}{ndq/dr}\right)^{1/2}$$

where B_r and n are the amplitude and toroidal mode number of the error field, B_p and q are the poloidal field and safety factor at the surface $r=r_o$ which is resonant with the perturbation. The expression is valid if the equilibrium surfaces are nearly circular and if the island width is much less than the minor radius.

The q=0 reversal surface is the surface that is most vulnerable to island formation since for a perturbation with poloidal mode number m=0, all n-values are resonant. Since $\Delta r \sim n^{-1/2}$, low n errors are the most dangerous; for example, if n=1 and $B_r/B_p \sim 0.00025$, then the island width is about one-tenth of the minor radius. For $m \neq 0$ only high n $\gtrsim$10) errors will produce islands. Our design goal is that the total radial distance covered by islands, which are produced by the sum of all predictable field errors, be less than one-tenth of the minor radius. For our design, this criterion, which is much less stringent than that listed below for local flux surface distortions, is well-satisfied and surpassed by about two orders of magnitude for the errors which have been calculated to date.

3.3.1.2 Magnetic Surface Distortions

Highly localized field errors, such as occurs at gaps, produce a broad wave-number spectrum and thereby tend to yield islands, due to specific resonances, which are small. Potentially more serious than surface breakup is the bump that occurs in the magnetic surface at the location of the gap. This is known to cause very harmful plasma-liner interaction.

We have adopted a guideline that all field-error-produced bumps shall be no greater than 1 cm, which is 3% of the minor radius. This is less than the 5% natural deviation from circularity which arises from toroidicity; i.e., concomitant with the toroidal shift of the plasma position, the plasma becomes slightly elliptical with an ellipticity of about 1.05. This in itself will cause some preferential heat deposition onto the liner (albeit not as localized as that due to a gap error).

3.3.2. Toroidal Field System

The toroidal magnetic field is produced by driving poloidal current through the 5-cm-thick aluminum vacuum tank. The advantages of this system over one that uses discrete toroidal field windings are (1) good diagnostic access, unencumbered by toroidal field windings, (2) greatly decreased field ripple, and (3) easier demountability of the vacuum tank, important for the studies involving shell exchanges.

As illustrated in Fig. 3.3.1, the poloidal current is fed to the tank through a long flange to diminish field rippple. The flange consists of a gapped cylindrical section connected to a horizontal disk section. Discrete transmission lines from a transformer connected to the capacitor energy storage supply connect to the bottom of the cylindrical section. The disk section of the flange connects to the vacuum tank gap at the midplane.

This system yields a negligible field error for two reasons. Firstly, the conducting vacuum tank provides a boundary condition of zero radial magnetic field (except at the gap) which greatly diminishes the error field in the chamber. Secondly, the current-profile-smoothing effect of the flange is sufficiently powerful that the chosen toroidal distribution of cables at the cylinder base is nearly irrelevant. The feed cables will connect to the cylinder base at four equally spaced locations with each connection covering 4^{o} of toroidal circumference. Below we describe the method and results of a calculation of the error magnetic field in the limit that the tank is a perfect conductor (the "inductive limit") and in the limit that the tank is highly resistive (the "resistive limit"). During the experimental time the toroidal field system is well-approximated by the inductive limit.

3.3.2.1 Inductive Limit

Method: We solve analytically for the magnetic field within the vacuum tank by separately treating each of the three regions and matching solutions at the boundaries. The current flow pattern in the

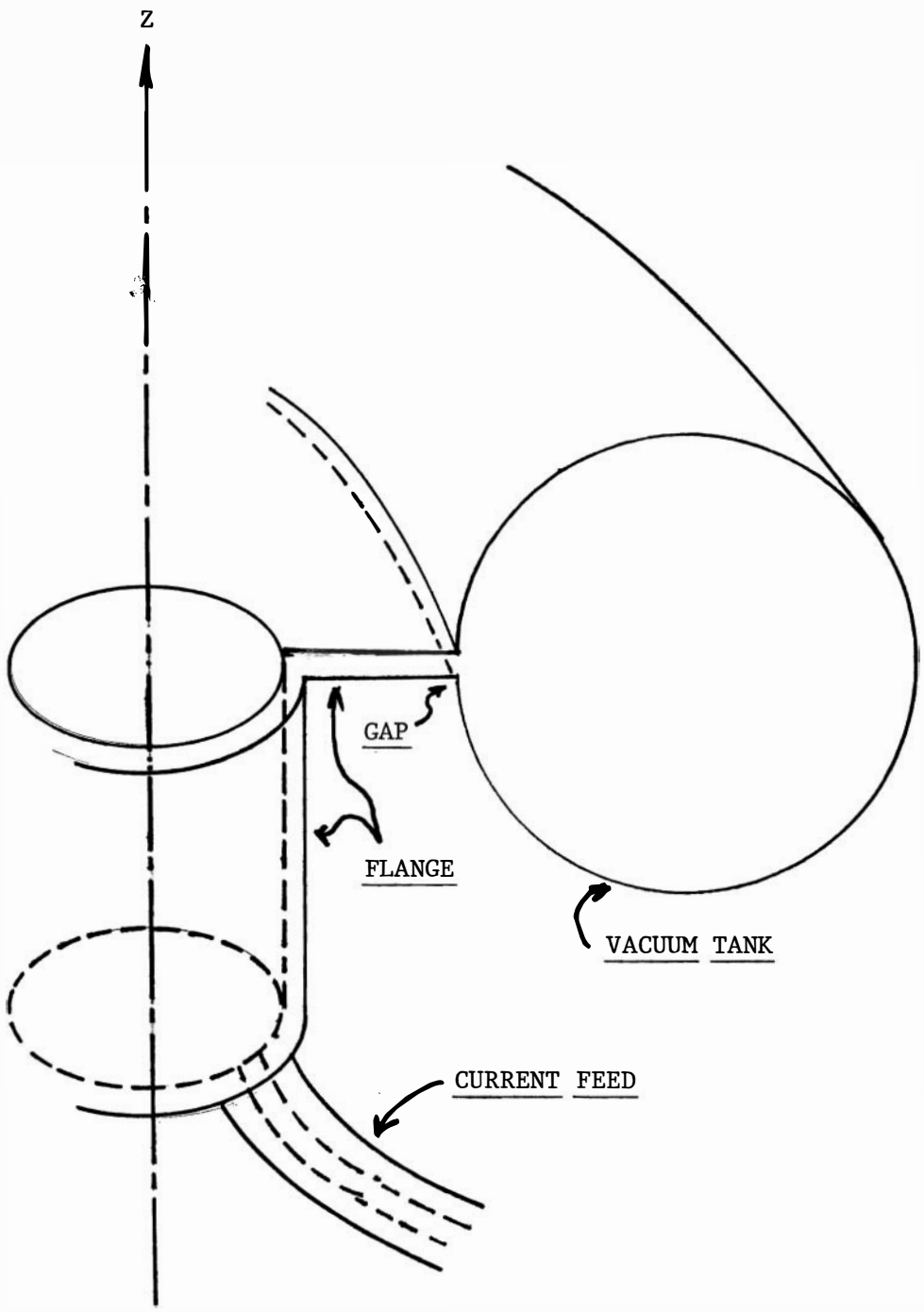

Fig. 3.3.1: Toroidal field system.

cylindrical and disk sections of the flange (regions 1 and 2) are calculated assuming the current flow is irrotational; such is the case if there are no induced currents. It is also the case in the present flange with a small gap width and identical toroidal distribution of cables at the base of the inner and outer cylinders. The induced image currents do not alter the flow pattern from that which exists if the induction were ignored, the purely driven case. The current per unit length, $\underline{j}$, flowing on the flange is then represented as $\underline{j} = \nabla\phi$, and the potential satisfies the two dimensional Laplace equation with solutions

$$\phi_1(\theta_1 z_1) = A_0 Z_1 + \sum_{n=1}^{\infty} (A_n e^{nz_1/r_c} + B_n e^{-nz_1/r_c}) \cos n\,\theta_1 \qquad (1)$$

on the cylinder and

$$\phi_1(r_2,\theta_2) = C_0 \ln r_2 + \sum_{n=1}^{\infty} (C_n r_2^{n} + D_n r_2^{-n}) \cos n\,\theta_2 \qquad (2)$$

on the disk. r_c is the cylinder radius, n is the toroidal mode number of the current distribution, (θ_1, z_1) are coordinates on the cylinder, and (r_2, θ_2) are coordinates on the disk.

The magnetic field in the vacuum tank (region 3) requires solution of a three-dimensional Laplacian for the magnetic scalar potential ϕ_3, where $\underline{B} = \nabla\phi_3$. If we ignore toroidicity an analytic expression for the potential is

$$\phi_3(r_3,\theta_3,z_3) = B_{z0}z_3 + \sum_{n=1}^{\infty} b_{r,n} \sin\frac{nz_3}{R}$$

(3)

$$\left\{\frac{d}{2\pi a}\frac{I'_0(\frac{nr_3}{R})}{I'_0(\frac{na}{R})} + \frac{2}{\pi}\sum_{m=1}^{\infty}\frac{\sin\frac{md}{2a}}{m}\frac{I_m(\frac{mr_3}{R})}{I'_m(\frac{ma}{R})}\cos m\theta_3\right\}$$

where (r_3,θ_3,z_3) are cylindrical coordinates within the tank, d is the gap width, a is the tank minor radius, R is the tank major radius, and the gap is located at $\theta_3 = 0$. Since d is small it was assumed as a boundary condition that the radial magnetic field is constant across the gap at r = a (and zero at the tank surface). The first term represents the desired symmetric toroidal field. The second term is a sum over toroidal and poloidal mode numbers n and m, with the first term in the curly bracket representing the m = 0 contributions.

The five coefficients A_n, B_n, C_n, D_n, and $b_{r,n}$ are straightforwardly obtained from the four matching conditions

$$J_{1z}(\theta_1,h) = J_{2r}(r_c p,\theta_2)$$

$$J_{1\theta}(\theta_1,h) = J_{2\theta}(r_c,\theta_2)$$

$$J_{2r}(R_i,\theta_2) = \frac{B_z}{\mu_0}(R_i,0,z_3) \qquad (4)$$

$$J_{2\theta}(R_i,\theta_2) = \frac{B_r}{\mu_0}(R_i,0,z_3)$$

and the specification of the cable distribution

$$J_{1z}(\theta_1,0) = \sum_{n=0}^{\infty} a_n \cos n\theta \qquad (5)$$

where a_n are the Fourier coefficients specifying the toroidal distribution of cables at the cylinder base. R_i is the tank inner major radius, and B_z, B_r are the fields within the tank.

Results: The n^{th} toroidal harmonic of the radial magnetic field at the gap in the vacuum tank is given (normalized to the axisymmetric toroidal field) by

$$\frac{b_{r,n}}{b_{z0}} = \frac{16}{7} \quad \frac{a_n}{a_0} \quad \left(\frac{r_c}{R_i}\right)^n \quad e^{-nh/r_c} \qquad (6)$$

amplitude at base	decrement due to disk	decrement due to cylinder

where R_i is the inner major radius of the torus. The full solution for the n^{th} toroidal harmonic of the field in the tank is obtained from Eq. (3) to be

$$B_{r,n} = b_{r,n} \sin n z_3/R$$

$$\left\{\frac{d}{2\pi a} \frac{I'_0(\frac{nr_3}{R})}{I'_0(\frac{na}{R})} + \frac{2}{\pi} \sum_{m=1}^{\infty} \sin \frac{md}{2a} \frac{I_m(\frac{nr_3}{R})}{I'_m(\frac{na}{R})} \frac{\cos m\theta_3}{m}\right\}$$

$$B_{\theta,n} = -b_{r,n} \sin z_3/R \frac{2}{\pi} \sum_{m=1}^{\infty} \sin \frac{md}{2a} \frac{I_m(\frac{nr_3}{R})}{I'_m(\frac{na}{R})} \sin m\theta_3 \qquad (7)$$

$$B_{z,n} = b_{r,n} \cos n \frac{z_3}{R} \left\{\frac{d}{a} \frac{I_0(\frac{nr_3}{R})}{I'_0(\frac{na}{R})} + \frac{2}{\pi} \Sigma \sin \frac{md}{2a} \frac{I_m(\frac{nr_3}{R})}{I'_m \frac{nr_3}{R})} \cos m\theta_3\theta\right\}$$

where the fields are represented as a sum over poloidal harmonics represented by poloidal mode number m.

The distortion of the magnetic surface at the gap is evaluated from the radial magnetic field at the plasma edge, obtained from Eq. (6). For the four-lead connection employed in the design, only n-values that are integer multiples of four contribute. We note from Eq. (6) that the n=4 component of the radial field at the surface of

the vacuum tank at the gap is 3% of the toroidal field (using r = 75 cm, h = 75 cm and R_i = 98cm). The flange reduces the n=4 component from its value at the cylinder base of nearly 200% (a_4/a_0 = 2) by a factor of about 70. Higher n components are negligible; e.g., the n=8 component is smaller than the n=4 by a factor of 160. The radial field amplitude decreases very rapidly with decreasing minor radius, as shown in Fig. 3.3.2 which plots $B_{r,4}$ versus r_3 using Eq. (7a). At the plasma surface at r_3 = 32 cm at the poloidal location of the gap, B_r/B_T is 0.2% (or B_r/B_p = 0.02%) which produces a bump in the edge magnetic surface of about 0.002 mm.

The poloidal spectrum of the error field, necessary to evaluate island widths, is obtained from the individual terms in the series of Eq. (7). However for n=4, the only term resonant in the plasma is the m=0 component given by

$$B_r\Big|_{\substack{m=0\\n=4}} = b_{r,4}\,\frac{d}{2\pi a}\,\frac{I'_0(\frac{4r_3}{R})}{I'_0(\frac{4a}{R})}\,\sin\frac{4z_3}{R} \qquad (8)$$

At the reversal surface $\dfrac{B_r\Big|_{\substack{m=0\\n=4}}}{B_p}$ is 0.005%, yielding an island width of about 1 cm.

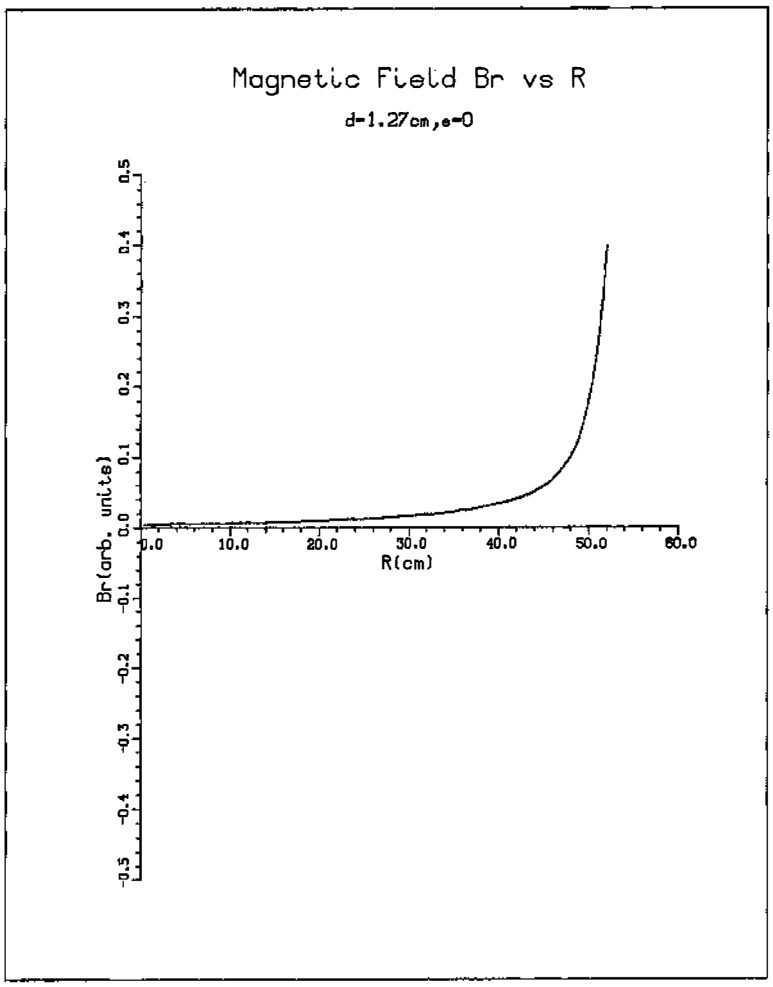

Fig. 3.3.2: Error radial magnetic field B_r vs radius (at the poloidal azimuth of the gap) generated by toroidal magnetic field system.

3.3.2.2 Resistive Limit

As time progresses during a discharge, the field error increases as radial magnetic field penetrates the vacuum tank. We have evaluated the field error in the worst case of the long-time limit and find that, with the flange system, the error is more than an order of magnitude lower than the design guideline.

In the resistive limit, all induced currents have decayed, the currents are purely driven and exactly described by solving the 2-D Laplace equation for the current flow, $\underline{j} = \nabla\phi$, on the conducting surfaces. Thus, the flange solutions are still given by Eqs. (1) and (2); the tank solution then simply requires solving for the 2-D current flow pattern on the toroidal surface (from which the fields are then calculated) and matching to the flange, as before.

Unfortunately, the 2-D Laplace equation is not separable when written in toroidal coordinates. However, analytic treatment of the toroidal vacuum tank current is still possible if we represent the tank as a sequence of disks and cylinders, as shown in Fig. 3.3.3. In the limit that the number of annular disks and cylinders is taken to be infinite an exact solution results.

The solution for the potential of the p^{th} segment, let us say a cylindrical segment, is given by

$$\phi_p(\theta_p, z_p) = A_p z_p + \sum_{n=1}^{\infty} (B_p e^{nz_p/r_{cp}} + C_p e^{-nz_p/r_{cp}}) \cos n\theta$$

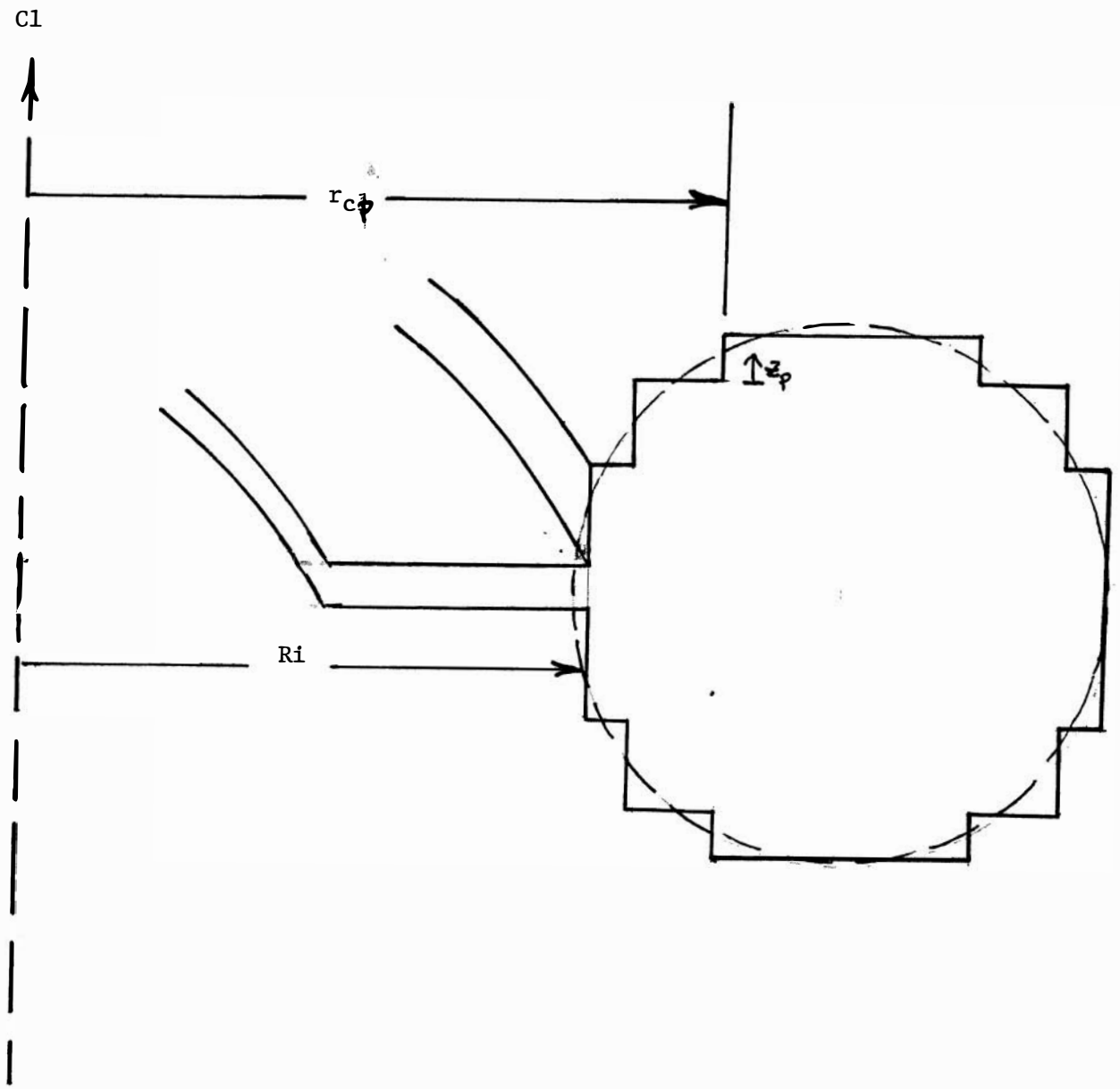

Fig. 3.3.3: Schematic illustration of representation of circular torus for resistive limit toroidal field calculations.

where (θ_p, z_p) are coordinates along the cylinder denoted by p and r_{cp} is the radius of the cylinder. For the p+1 segment, a disk,

$$\phi_{p+1}(r_{p+1},\theta_{p+1}) = A_{p+1}\ell nr + \sum_{n=1}^{\infty} (B_{p+1}r_{p+1}^{n} + C_{p+1}r_{p+1}^{-n})\cos n\theta \quad .$$

The ratio of the height h_p to radius r_{cp} of each segment is determined by the requirement that the segments lie along a circle. Matching of the solutions at each disk/cylinder boundary is straightforward; therefore we will advance to the results.

The radial magnetic field at the location of the gap for the n^{th} toroidal mode is

$$\frac{b_{r,n}}{b_{z0}} = \frac{a_n}{a_0}\left(\frac{a}{R_i}\right)^n e^{-nh/a} \qquad (9)$$

where the approximation $a^n << R_i^n$ was employed. This expression is identical to Eq. (6), the inductive case, except for a numerical factor. For the dominant n = 4 mode, $\frac{b_{r,4}}{B_{z0}}$ is 1.3%. This creates a magnetic surface distortion of about 0.01 mm. However the field does not diminish as rapidly with decreasing radius as for the inductive case.

To evaluate the m = 0 island width we poloidally average the n = 4 current. The nonaxisymmetric component of the poloidal current at an arbitrary location on the tank, $\tilde{j}_p$, is given by

$$\frac{\tilde{j}_{p,n}}{j_0} = \frac{a_n}{a_0}\, 2\, \left(\frac{a}{R}\right)^n\, e^{-nh/a}\, e^{-n\Sigma_j h_j/r_{cj}} \qquad (10)$$

where j_0 is the axisymmetric poloidal current, R is the major radius of the point at which the current is evaluated, and the summation is over all cylindrical segments at major radii smaller than the given location. Again, we invoked $a^n << R^n$. This expression is similar to Eqs. (6) and (9) for the error field at the gap, except that the error is diminished. That is, the vacuum tank itself serves as a flange in that as current proceeds poloidally around the tank, it spreads and becomes more axisymmetric. The disk-like effect of the tank is evident in the $(a/R)^n$ term, and the effect of all the small cylindrical segments is seen in the last exponential term.

The ripple-smoothing effect of the tank itself is observed by noting that at the outside of the tank at the midplane the error current has decreased to 0.021% (from 1.3% on the inside). At this location the summation in the exponential term can be calculated analytically in the exact limit of an infinite number of cylindrical segments. The m = 0 component of the error current (or error field) is about 0.35% of the axisymmetric component. The m = 0, n = 4 radial field diminishes slowly with radius as

$$b_r\Big|_{\substack{m=0\\n=4}} \sim I_0\, \left(\frac{4r}{R}\right) \quad . \qquad (11)$$

At the reversal surface (r= 25 cm) the radial field is 0.25% of the toroidal field which yields an island width of about 4.5 cm.

Thus, as time progresses during a discharge, the surface distortion and islands increase, but always remain negligible.

3.3.3. Poloidal Field System

The plasma current and poloidal magnetic field are driven by an iron core transformer with primary windings wound around the core. The conducting vacuum tank carries an image current of the toroidal plasma current. The axisymmetry of the tank currents (which play the role in plasma shaping of the usual axisymmetric primary winding current) is achieved by an additional system of windings (called continuity windings) which connect from one side of the poloidal gap in the tank to the other side, as shown in Fig. 3.3.4. The continuity windings surround, but do not link, the core. Their purpose is to allow the toroidal tank current to continue across the gap without distortion. The continuity currents are tightly coupled to the primary windings whose poloidal distribution is such that the driven continuity winding current matches the desired tank current distribution (which images the plasma).

This poloidal field system is chosen because it is energy-efficient and allows diagnostic access unencumbered by primary windings surrounding the torus. The field error amplitude is determined by the degree of perfection of the poloidal distribution of the primary/continuity winding system. The continuity winding surrounds the square core and is connected to the circular vacuum tank

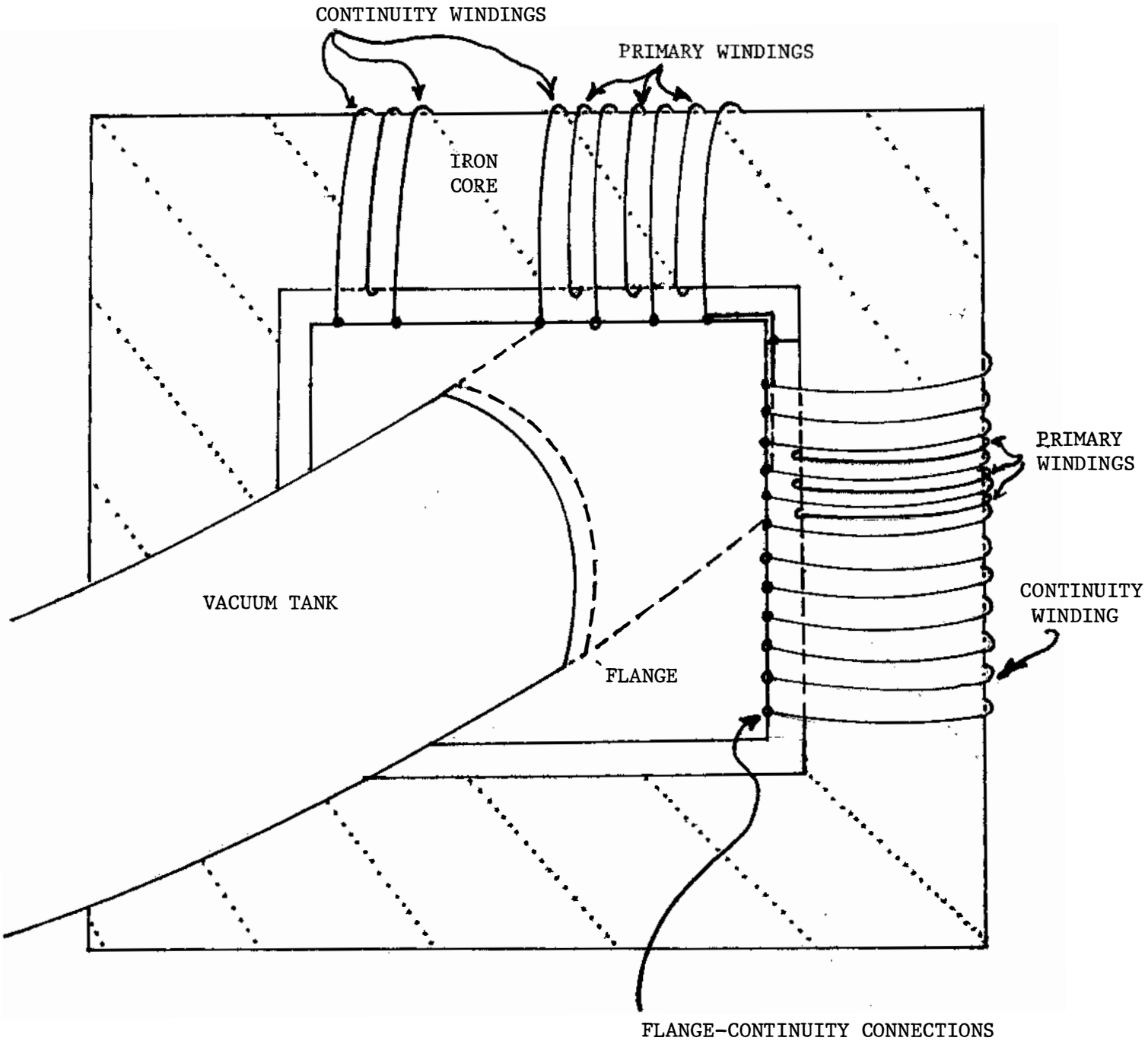

Fig. 3.3.4: Schematic illustration of poloidal magnetic field system.

via a flange (see Fig. 3.3.4). The flange reduces the effect at the tank gap of field errors generated by continuity-winding imperfections.

We first evaluate the desired primary winding distribution which results in no field error, that is, no radial magnetic flux penetrating the gap. The desired toroidal tank current is obtained from the equilibrium code described in Sec. 3.4.6. A typical poloidal distribution of the tank current density is shown in Fig. 3.3.5, where the effect of the outward shift of the plasma is seen to enhance the current at the outside of the torus.

The desired primary/continuity winding distribution is that which satisfies two requirements at the gap. Firstly, the poloidal distribution of the radial current in the flange, at the tank surface, must match that of Fig. 3.3.5. Secondly, the poloidal current at the flange tank interface must be zero. These conditions serve as two boundary conditions in the solution for the current density flow pattern $\underline{j}(r,\theta)$ on the flange, i.e.,

$$j_\theta(a,\theta) = 0$$

$$j_r(a,\theta) = \sum_m a_m \cos m\theta$$

where the a_m specify the tank distribution and (r_i,θ) are coordinates on the flange. Solution of the 2-D Laplace equation for ϕ, where $\underline{j} = \nabla\phi$, straightforwardly specifies the current everywhere in the plane of the flange. The desired primary/continuity winding current distribution is obtained by then evaluating the current density on the

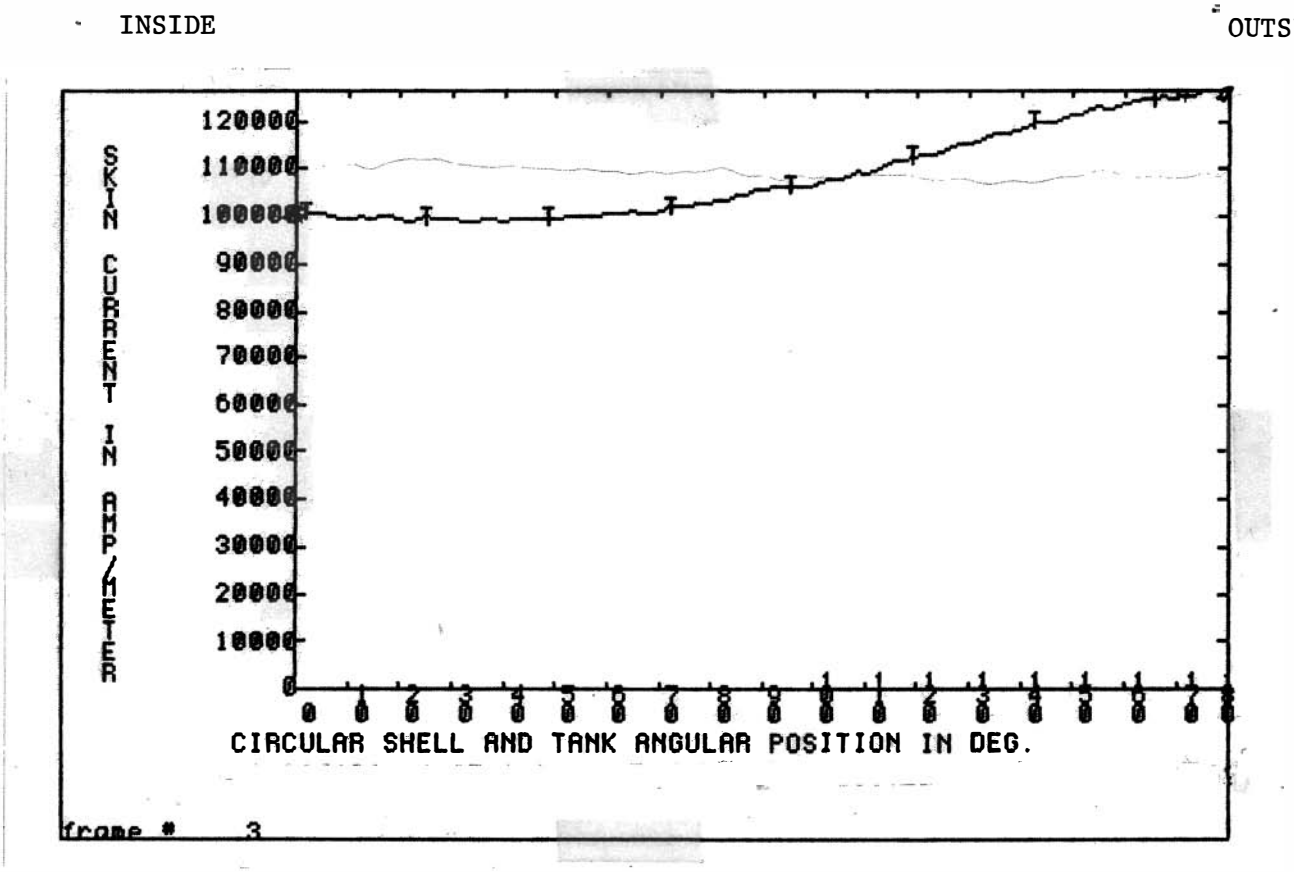

Fig. 3.3.5: Vacuum tank toroidal current density vs poloidal angle (over 180°).

appropriate square contour. The component normal to the square edge of the flange is the current magnitude that must be carried by the continuity winding at that point.

The resulting primary/continuity current distribution is shown in Fig. 3.3.6 for four cases -- the 32 cm, perfectly conducting ("thick") shell case, the 32 cm plasma thin shell case, the 52 cm plasma case and a hypothetical case (dashed curve) of a straight plasma in which toroidicity is ignored. Each figure shows the distribution in one leg of the core (top half-plane only). Comparison with the straight plasma case indicates that the dominant poloidal nonuniformity in the distribution arises simply to accommodate the $1/r^2$ falloff of $\underline{j}$ and nonuniformity of the distance between the circular tank and square winding aperture. Case-to-case differences arise from toroidal effects of differing current profiles. Clearly, adjustability of the winding distribution is necessary to accommodate the various cases.

To evaluate the field error generated by imperfect primary/continuity windings we solve for the flange current as before, but with the first boundary condition replaced by a chosen distribution of normal currents at the square boundary which represents an improperly distributed continuity winding current. The resultant flange poloidal current at the tank surface at the gap is then evaluated, which yields directly the radial error field. Numerical solution of this problem, as well as calculation of the expected deviation of the windings from the ideal case, is still in progress.

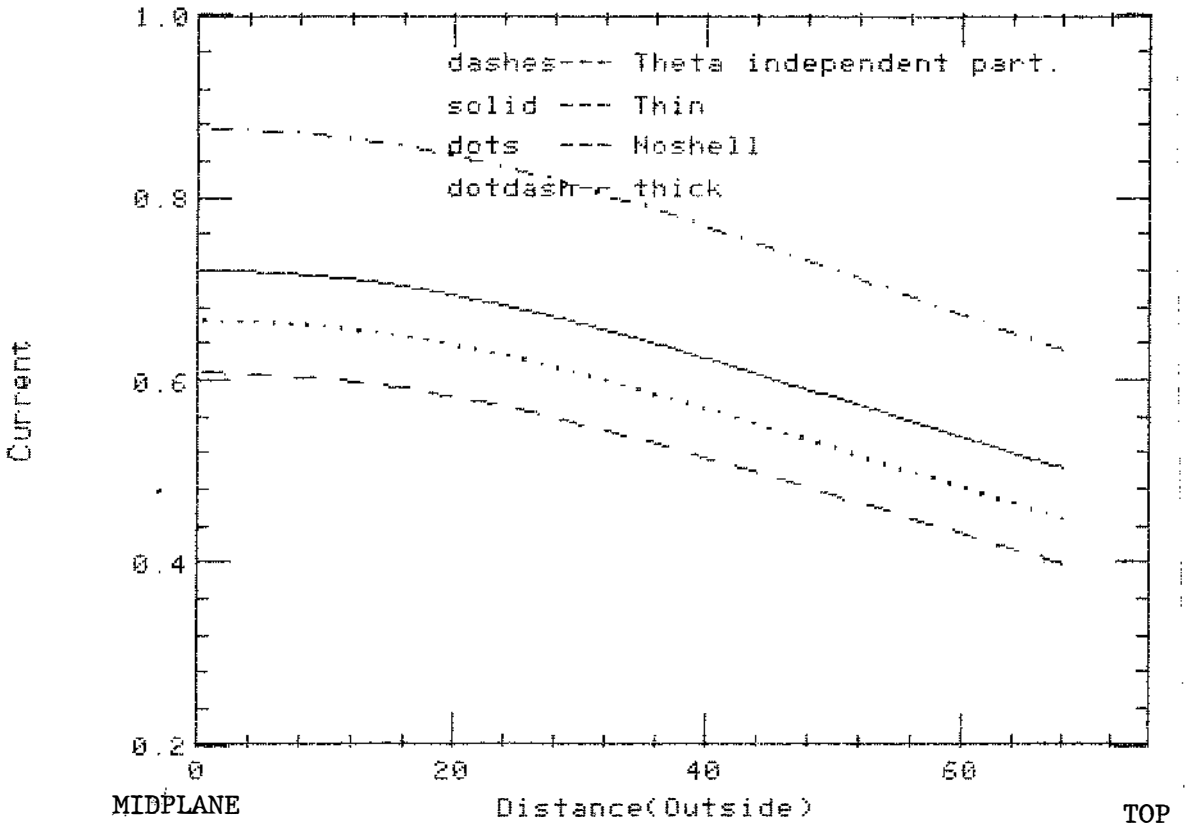

Fig. 3.3.6a: Desired outside primary winding current density vs distance ~~along~~ the core for four different plasma cases.

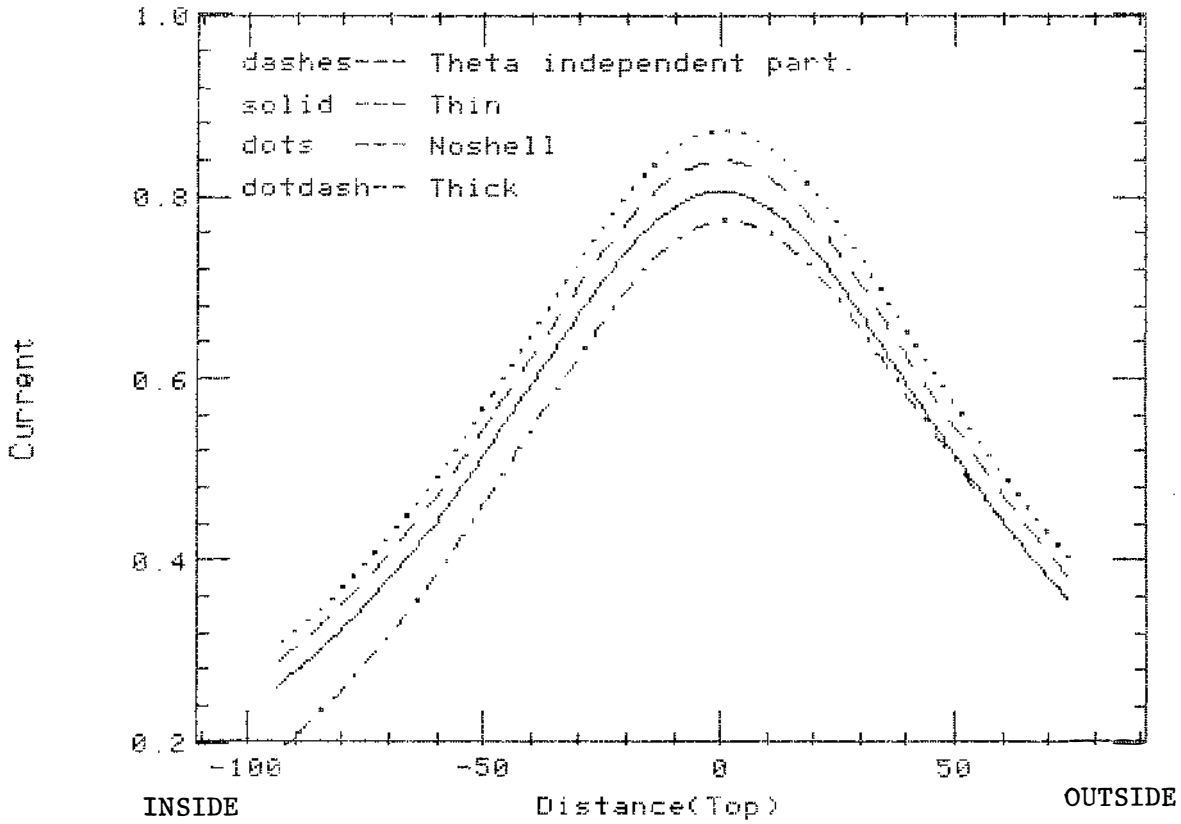

Fig. 3.3.6b: Desired top primary winding current density.

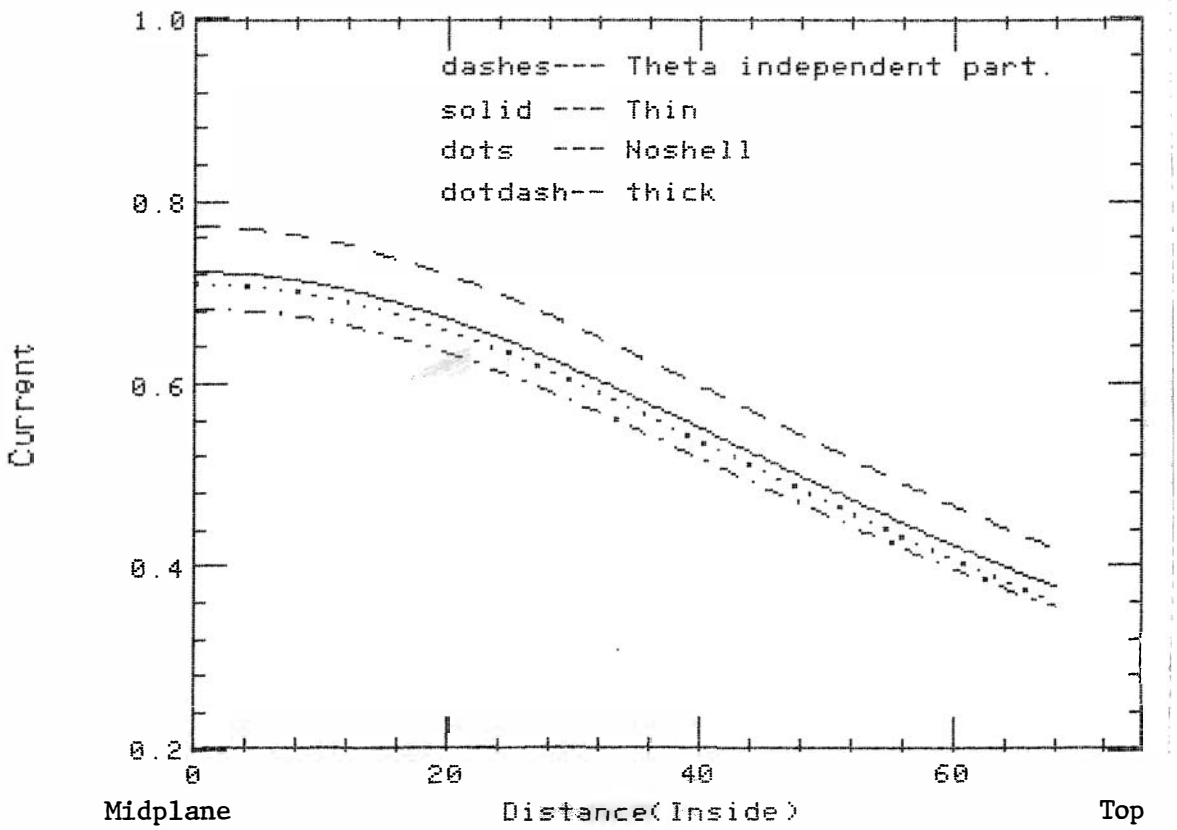

Fig. 3.3.6c: Desired inside primary winding current density.

However, initial results, as follows, indicate that the field error is extremely small.

Preliminary estimates indicate, for example, that if the winding distribution were hypothetically chosen to ignore entirely toroidal effects (i.e. the dashed curve of Fig. 3.3.6), the m = 1 radial field entering the tank gap would be about 20% of the poloidal magnetic field, the m = 2 about 15%, and succeeding poloidal modes much smaller. Although seemingly large, these errors create negligible magnetic islands. Due to the vanishing of the radial field on the wall away from the gap, the relevant Fourier modes are small. For example, the m = 1, n = 10 mode would be about 0.02% of the poloidal field, yielding an island width of about 1 cm.

To evaluate the local bump in a magnetic surface at the gap, we have evaluated the n^{th} poloidal harmonic of the field inside the tank to be

$$B_{r,m} = b_r \sin m\theta \left\{\frac{d}{2\pi r}\left(\frac{r}{a}\right)^{m-1} + \frac{2}{\pi}\sum_{n=1}^{\infty} \sin\frac{nd}{2R}\,\frac{I'_m\left(\frac{n_r}{R}\right)}{I_m\left(\frac{n_a}{R}\right)}\,\frac{\cos\frac{n_z}{R}}{n}\right\}$$

where b_r is the radial field at the gap (at r = a), d is the gap width, and z is the toroidal direction. The significant point is that the radial field decreases extremely rapidly with decreasing radius. Figure 3.3.7 shows the minor radial dependence of the m = 1 component of the radial field at the toroidal azimuth of the gap. At a minor

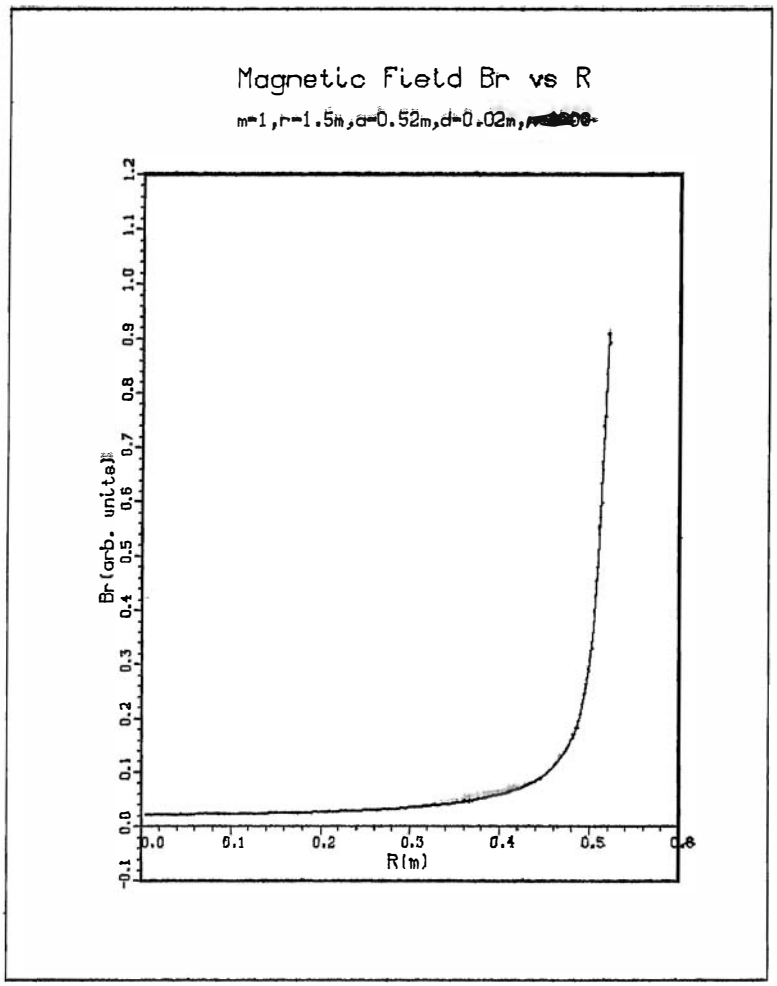

Fig. 3.3.7: m = 1 error radial magnetic field vs minor radius (at the toroidal azimuth of the gap) generated by the poloidal field system.

radius of 45 cm, the error field has fallen by an order of magnitude from its wall value. At the surface of a 32 cm plasma the error field is about 4% of its wall value. Hence, for the above-mentioned 20% wall error, the error at the plasma is only about 1%, which creates a bump in the magnetic surface of about 1 cm, which is well within our guidelines. Higher m values behave similarly, as depicted for m = 2 in Fig. 3.3.8.

3.3.4 Errors Due to Portholes

Any aperture in the shell or vacuum tank interrupts the current flow, thereby creating a local field error. An advantage of having the vacuum container separate from the first wall is that the large pump ports need only be located in the large vacuum tank which is relatively far from the 32 cm plasma. All holes in the shell and liner will be 1.25" diameter or less. This includes holes for pumping, diagnostics, gas feed, etc.

Nevertheless, these small holes create errors that must be evaluated. For a single hole in a thin, conducting wall (wall thickness much less than hole radius) the current density flow pattern in the wall is easily solved and is given by

$$J_r = (1-a^2/r^2)J_0 \cos\theta$$

$$J_\theta = -(1 + a^2/r^2)J_0 \sin\theta$$

where (r,θ) are polar coordinates centered on the circular hole, a is

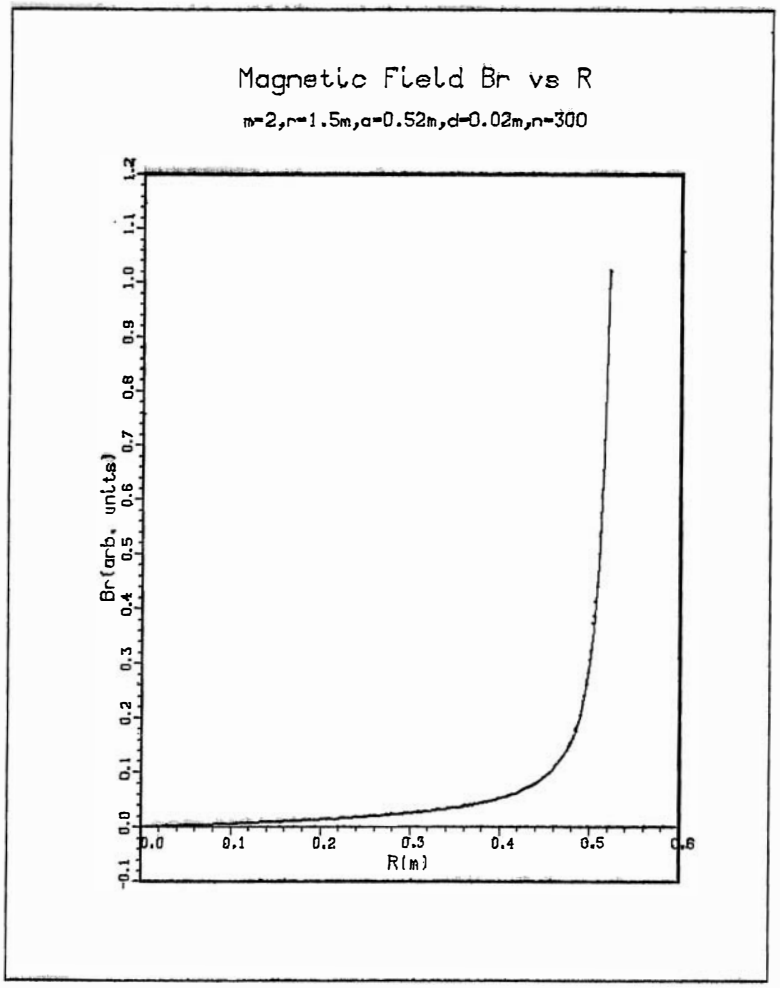

Fig. 3.3.8: m = 2 error field generated by poloidal field system.

the hole radius, and J_0 is the current density far from the hole. The current flow pattern described by these equations is sketched in Fig. 3.3.9. Given these currents, we have solved for the resultant error field away from the hole. Figure 3.3.10 illustrates the spatial dependence of the radial error field. The next step will be to superpose the error fields due to all the holes in the shell, evaluate magnetic surface distortions and Fourier analyze to calculate island structure.

A refinement of the above calculation, which will be enacted, will be to include the finite thickness of the conducting wall. Similar to a flange, this has the effect of somewhat reducing the perturbation to the current since the current can now circumvent the hole by flowing on the lip of the hole rather than the longer path on the plane (see Fig. 3.3.11). An inexact estimate of this effect is easily obtained by assuming the current on the hole is driven, with no induced effects. The 2-D problem is then separately soluble on the plane and on the cylindrical surface. Matching then yields the solutions on the plane,

$$j_r = (1 - a^2/r^2\ e^{-2w/a}) j_0 \cos\theta$$

$$j_\theta = -(1 + a^2/r^2\ e^{-2w/a}) j_0 \sin\theta$$

where w is the thickness of the wall. Thus, the second term in each equation, which represents the deviation from the straight streamlines, is diminished by an exponential factor which depends upon the thickness/radius ratio. If $w \simeq a$, the current streamlines will be nearly straight everywhere for $r > a$.

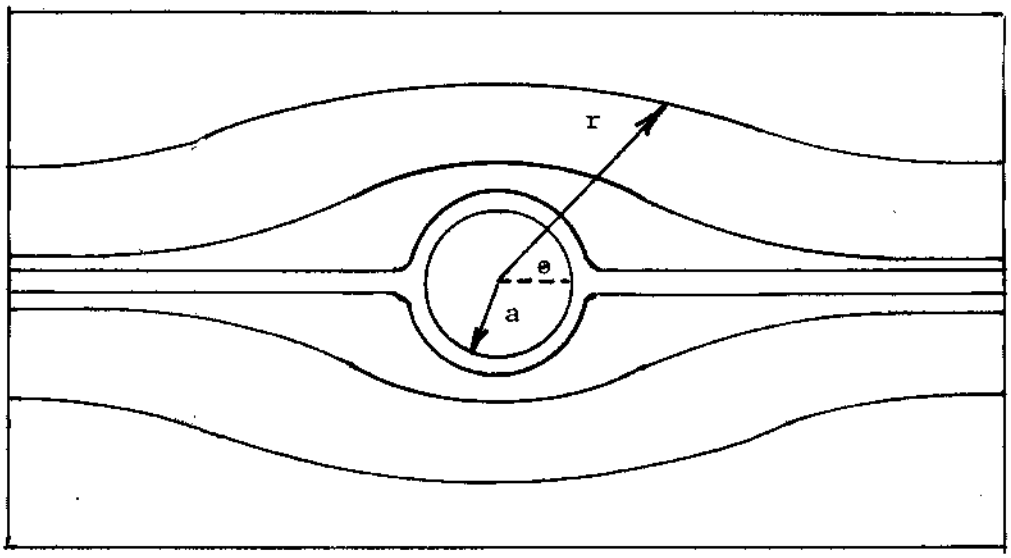

Fig. 3.3.9: Sketch of current flow pattern around a hole in a zero-thickness wall.

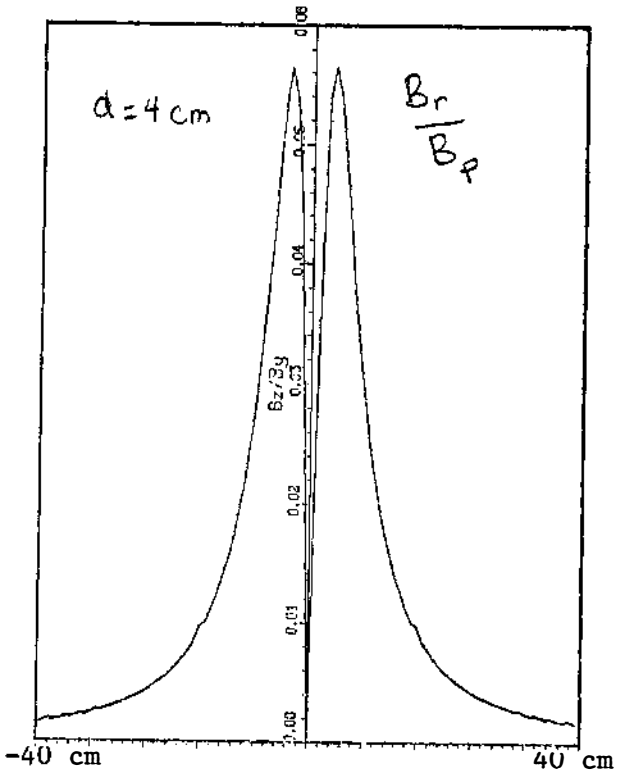

Fig. 3.3.10a: Radial magnetic field (normalized to B_p) due to 1-1/4" diameter porthole at a distance, d, of 4 cm from the wall plane. Horizontal axis is distance parallel to plane, orthogonal to unperturbed current flow, passing through the hole axis. The right-hand side of the curve has been inverted.

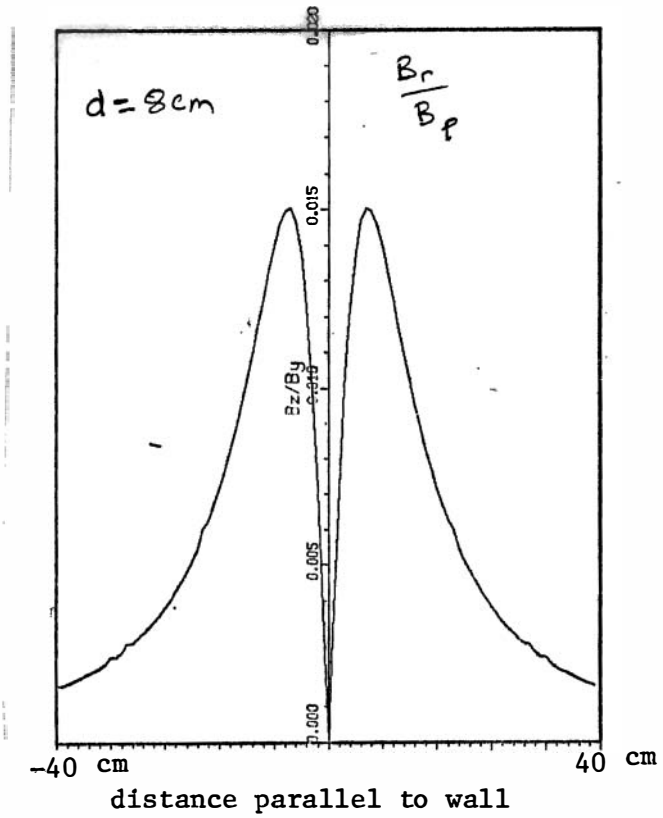

Fig. 3.3.10b: Porthole field error at 8 cm from wall.

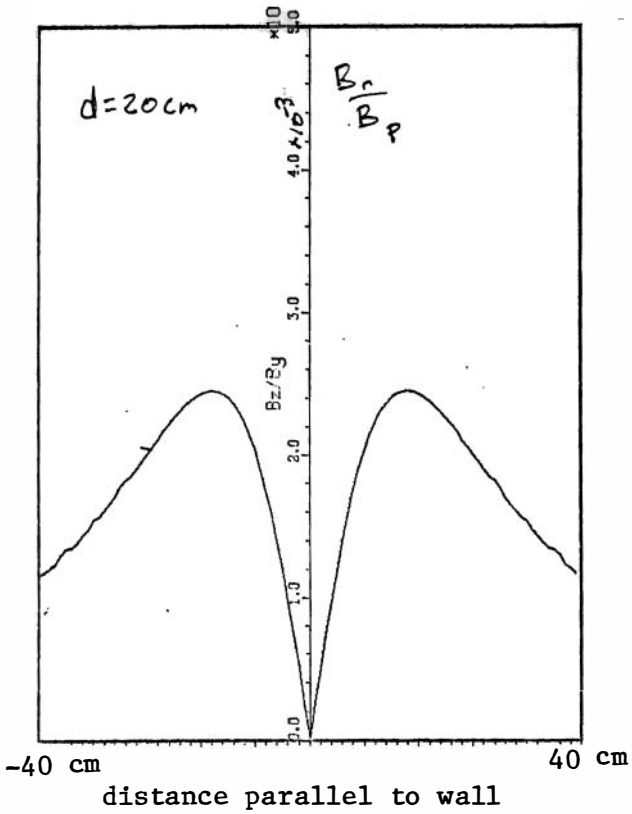

Fig. 3.3.10c: Porthole field error at 20 cm from wall.

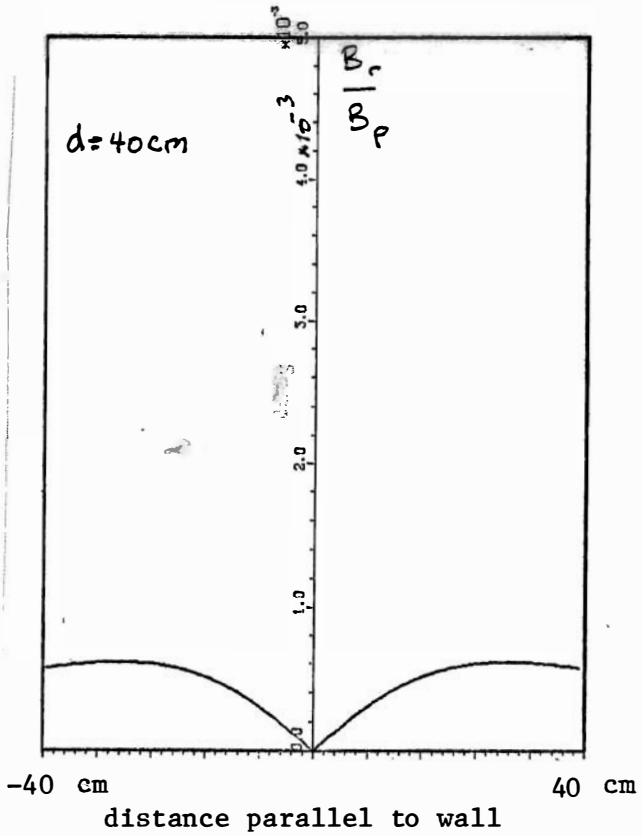

Fig. 3.3.10d: Porthole field error at 40 cm from wall.

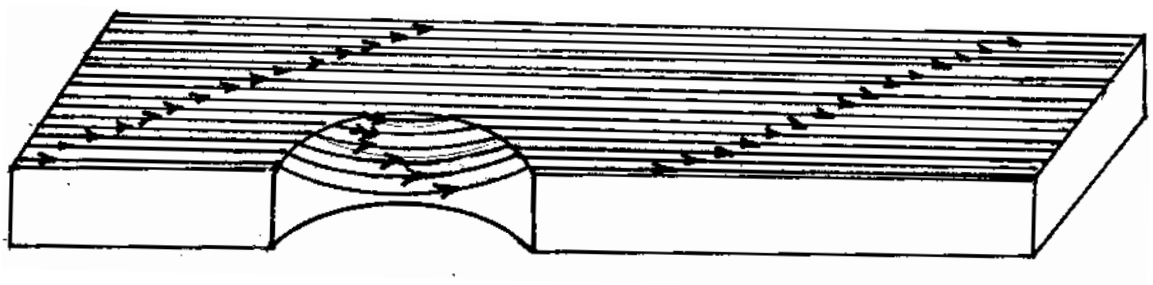

Fig. 3.3.11: Illustration of current flow pattern around a hole in a finite thickness wall.

An appropriate three-dimensional calculation in the inductive limit will follow the thin-wall calculation.

3.3.5 Field Error Correction Scheme

After all due attention has been paid to reducing field errors, we will have the capability of feedback control of local errors as described in Sec. 5.4.4 of our original proposal. Basically the provision entails including 378 holes of 1/4" diameter around the poloidal and toroidal gaps in the vacuum vessel (128 on inner toroidal flange, 166 on outer toroidal flange, and 84 on the poloidal flange) so as to allow sense and feedback coils which drive to zero the component of magnetic field normal to the gap. High-power operational amplifiers capable of providing 1000 to 2000 ampere-turns at 20 volts with a risetime of 50 μsec have been prototyped and tested on the Octupole. These will be installed only if residual field errors at the gaps are determined to be a problem and then only in such quantity as is required to eliminate any degredation of performance due to field errors at the vacuum vessel gaps.

3.3.6 Shell Gap Field Errors

In order to ameliorate errors generated by the poloidal and toroidal gaps in the shell, we are installing two shells with the gaps of the two shells displaced. Thus the gaps in the inner shell are surrounded by the conducting metal of the second shell which, somewhat similar to a flange, allows the necessary current distortion at the gap

to occur on the outer shell, leaving the inner shell currents relatively axisymmetric. This technique has been discussed in some detail in the original proposal; our approach has not changed.

3.4 Magnetics and Electrical Circuits

3.4.1 Electrical Circuit Model

The primary tool for designing the electrical circuits for driving the plasma current and magnetic fields has been a numerical circuit model similar to that used by Culham and Los Alamos to predict the waveforms for HBTX-1A, ZT-40, and other RFP devices. The poloidal and toroidal field circuits are shown in Fig. 3.4.1. Each field is driven through an iron-core transformer. The components on the primary of each transformer have already been installed except for inductor L_{P2} which is used to flatten the waveform and will be added after the plasma resistance has been determined experimentally. In the poloidal field secondary, the inductance L_{PS} represents flux outside the liner and leakage flux between the primary and continuity windings. The calculation is somewhat conservative in that the flux excluded by the shell (27% of the total) is ignored. The eddy currents in the shell decay with a time constant of 6 msec. R_{PL} is the resistance of the liner in the toroidal direction. The plasma is represented by a resistance R_P and a current source I_ϕ in the toroidal direction. Similarly, the toroidal field secondary has an inductance L_{TS}, a liner with poloidal resistance R_{TL}, and a poloidal plasma current I_θ.

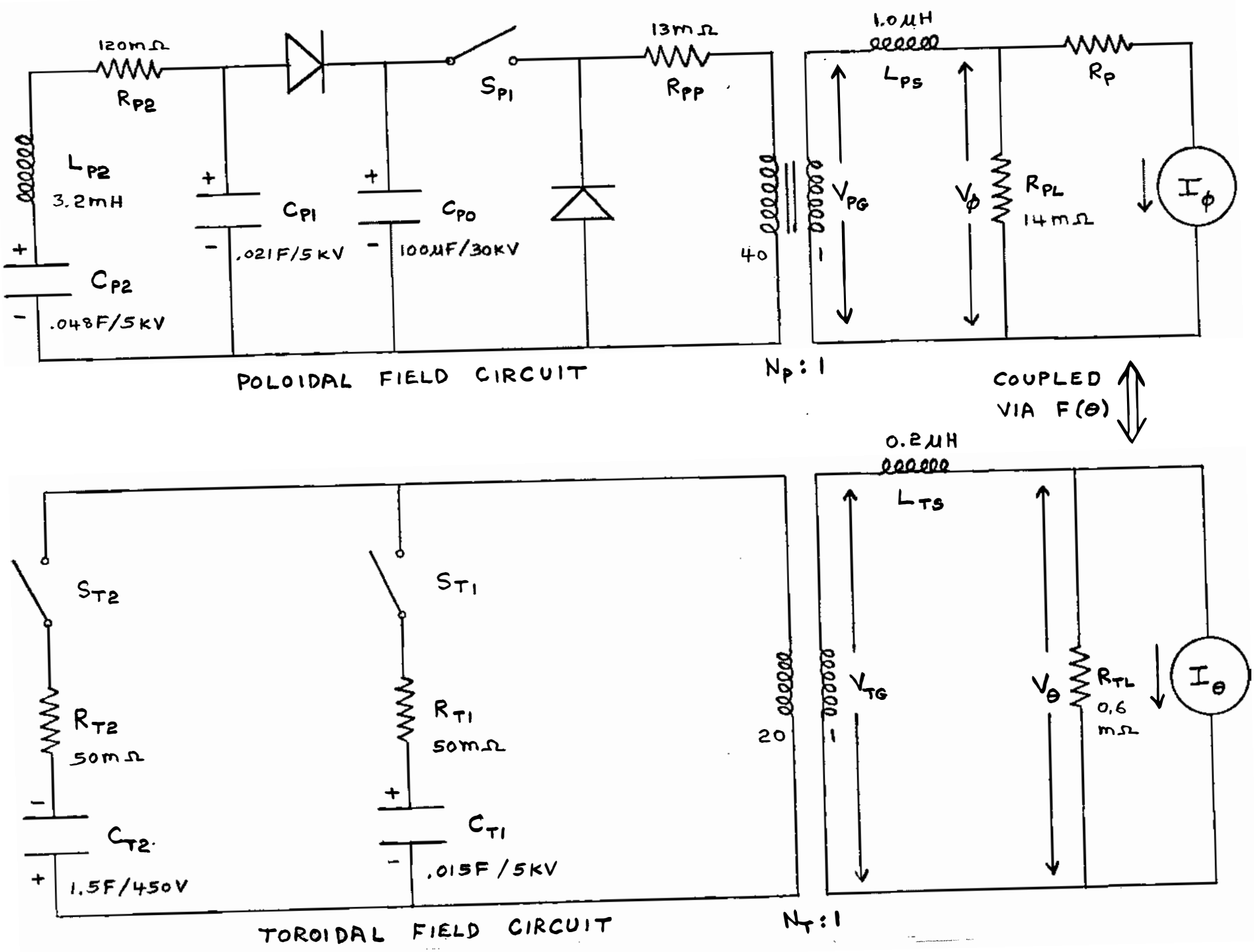

Fig. 3.4.1: MST Electrical Circuit Model.

The two circuits are coupled via the F(θ) curve for a modified Bessel function model, where

$$F = \frac{\mu_o I_\theta}{2\pi R_o \langle B_\phi \rangle}$$

$$\theta = \frac{\mu_o I_\phi}{2\pi a \langle B_\phi \rangle}$$

and $$\langle B_\phi \rangle = \frac{1}{\pi a^2} \int V_\theta \, dt \quad .$$

A polynomial expression for F(θ) recommended by Los Alamos has been used:

$$F = 1 - 0.438156\ \theta^2 - 0.078398\ \theta^3 - 0.190109\ \theta^4 + 0.0985\ \theta^5 \quad .$$

This expression is plotted in Fig. 3.4.2. Furthermore, a portion of the toroidal current I_ϕ is induced by the poloidal voltage V_θ according to

$$(L_P + L_{PS}) \frac{dI_\phi}{dt} = V_{PG} - BV_\theta - I_\phi R_P$$

where the internal effective plasma inductance L_P and the coupling constant B are given by other polynomial functions of θ,

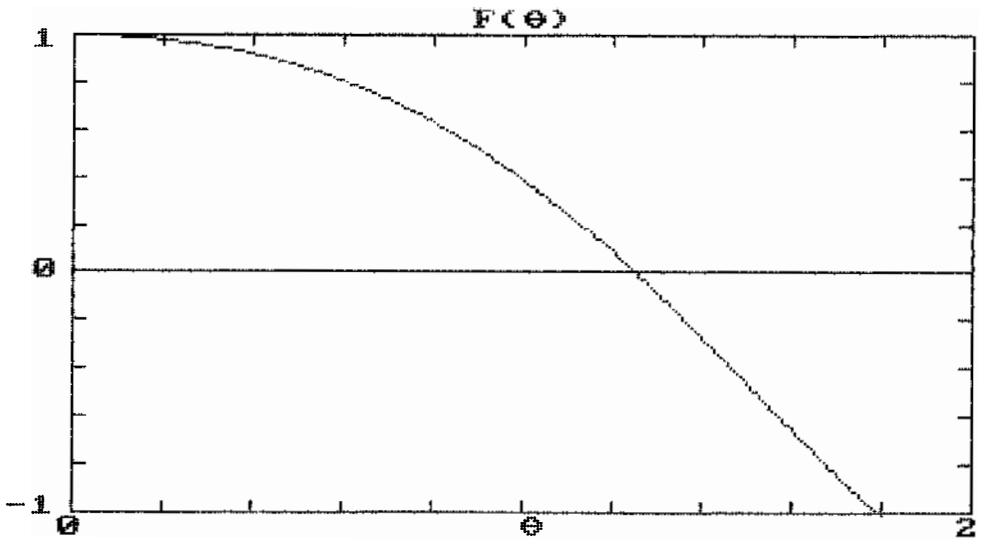

Fig. 3.4.2: Modified Bessel function model used for electrical circuit simulation.

$$L_P = \frac{\mu_o R_o}{4} (0.984715 + 3.45668\ \theta^2 - 10.9655\ \theta^3 + 15.1737\ \theta^4 - 5.2924\ \theta^5)$$

$$B = \frac{R_o}{a} (0.438156\ \theta + 0.078398\ \theta^2 - 0.674063\ \theta^3 +$$

$$3.19116\ \theta^4 - 5.05789\ \theta^5 + 1.89014\ \theta^6)$$

which are graphed in Fig. 3.4.3. Note that this inductance is not the inductance that one multiplies by the plasma current to get the internal poloidal flux, but rather is an effective inductance related to it by $L_P + \frac{\theta}{2} \frac{\partial L_P}{\partial \theta}$.

The magnetizing current in the poloidal iron core has been represented by

$$I_{PC} = 0.67\ e^{|7(\Phi/A - B_C)|}$$

where Φ is the flux in the core

$$\Phi = \int V_{PG}\ dt$$

B_C is the initial iron-core bias field (1.5 tesla), and A is the effective cross-sectional area of the core ($0.58 m^2$). These quantities have been calculated from the manufacturer's specification for the iron and compared with experimental measurements (see Sec. 3.4.4). The toroidal iron core has excess volt-seconds and hence negligible magnetizing current for the purposes of the present calculation.

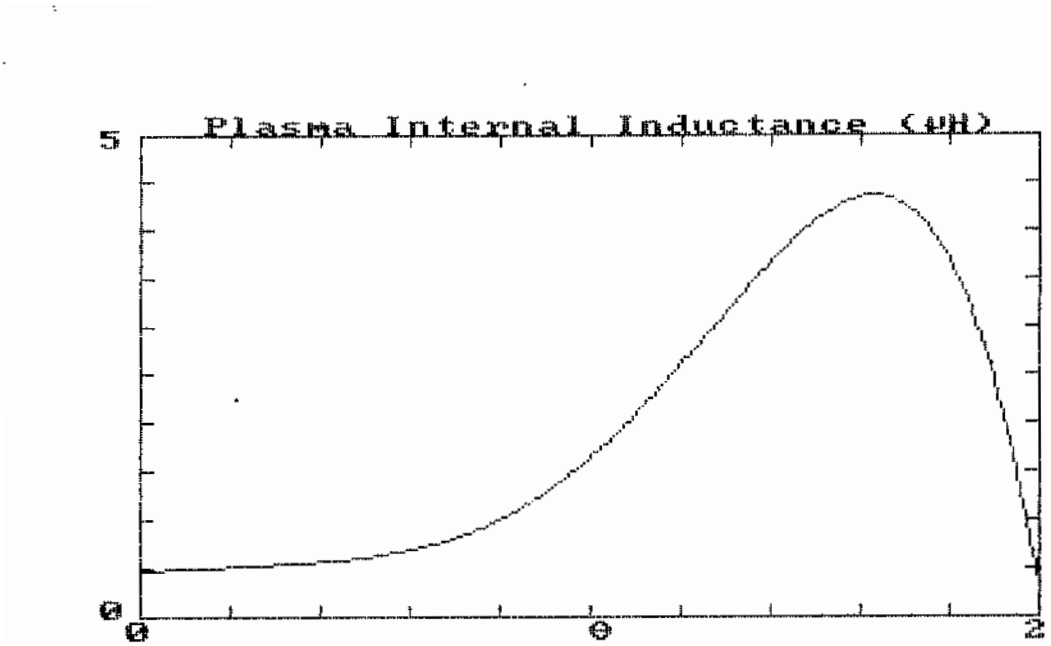

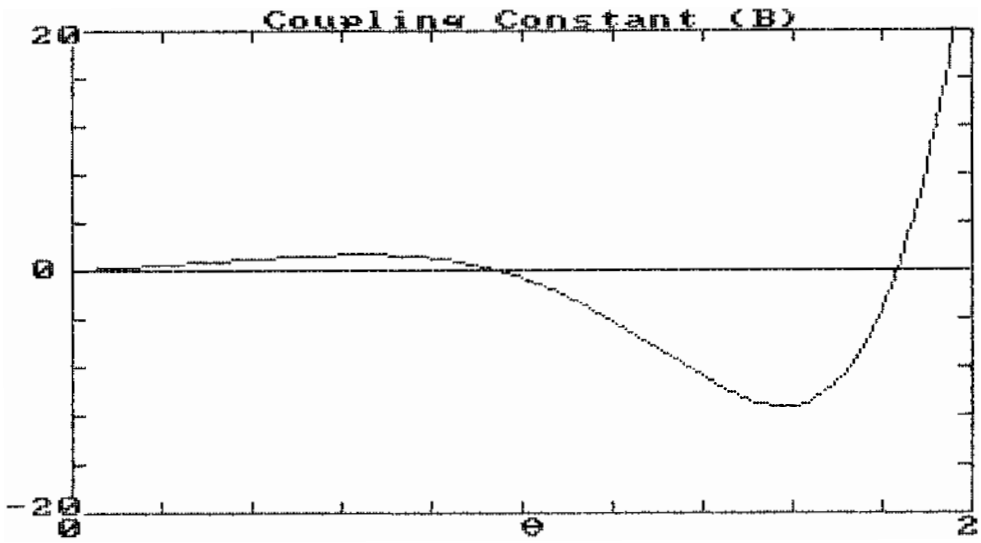

Fig. 3.4.3: Plasma internal inductance (a) and coupling constant (b) vs pinch parameter θ.

The switch S_{P1} in Fig. 3.4.1 is closed at t = 0 to begin the discharge, and the capacitors C_{P0}, C_{P1}, and C_{P2} are assumed to be charged to their full rated voltages. Switch S_{T1} is closed before the start of the calculation at a time such that the voltage across C_{T1} is zero at t = 0 and the average toroidal field is 800 gauss. Switch S_{T2} is closed when the toroidal field at the wall crosses zero (when I_θ reverses). C_{T2} is initially charged to -450 volts. The switches and the diodes are actually ignitrons with forward voltage drops of 13 volts. No ignitrons have to open under load.

The most critical (and unfortunately the least certain) electrical parameter is the plasma resistance. There is evidence that when Z_{eff} and geometric factors are properly taken into account, the resistivity during the flat top phase of the discharge is classical. Furthermore, the temperature appears to scale linearly with plasma current (~1 eV/kA) at least if the plasma density is controlled. We have therefore assumed for most of the circuit modeling a classical scaling with the coefficient adjusted to fit a 200 kA, 50 volt, ZT-40M discharge:

$$R_P = 770\ (R_o/a^2) I_\phi^{-3/2} \quad .$$

This case was chosen because of the large data base that exists for ZT-40M and because it is similar in current density to that expected in MST. It is somewhat conservative in that recent ZT-40M discharges after pulsed discharge cleaning have been as low as 40 volts at 200 kA.

The scaling above apparently underestimates the observed resistivity during startup when high startup voltages are used (see Sec. 3.4.4). To give a resistive volt-second consumption that scales properly from ZT-40M, the resistivity during startup (when $F > 0$) is enhanced by a factor of $V_{P0}/12500 + 0.6$ where V_{P0} is the startup bank voltage (5-30 kV).

In order to avoid an infinite resistance at $t = 0$ when $I_\phi = 0$, an upper bound of 20 mΩ is placed on the resistance. This initial resistance is consistent with what is seen on ZT-40 and should be easily achieved by low power ECRH (50 W of 2.45 GHz). It corresponds to a conductivity temperature of ~1 eV. No additional allowance is made for breakdown since it is assumed that ECRH will provide the preionization.

There was a small error in the circuit model whose net result is to require a 200 μF rather than a 100 μF fast startup bank for the B_p circuit to yield the waveforms shown in the presence of a continuous resistive liner. Thus extra capacitors would have to be purchased at an estimated cost of $5,000.

3.4.2 Baseline Design Waveforms

Subject to the approximations of the previous section, electrical waveforms have been calculated and displayed in Fig. 3.4.4 for the case in which all capacitor banks are charged to their full rated voltages. Although there is room to trade off parameters such as peak current and

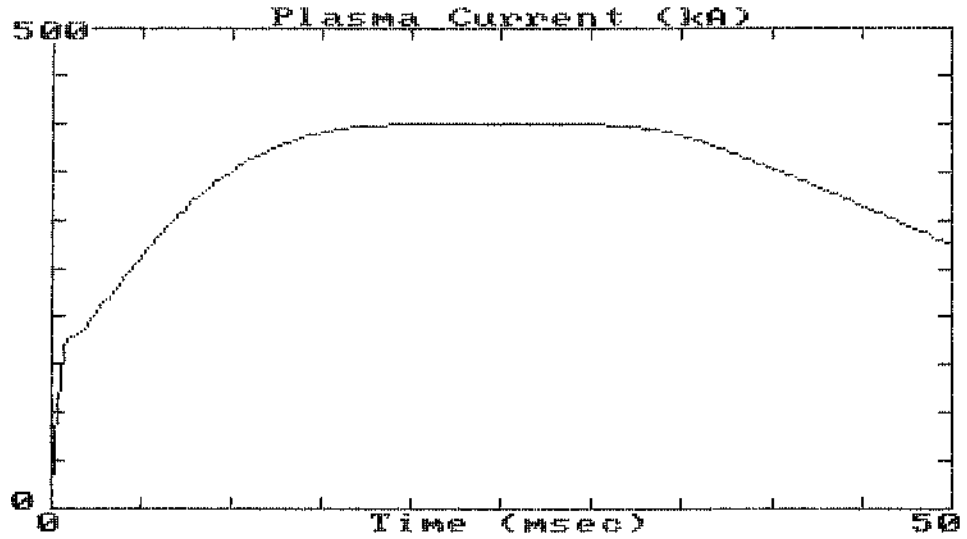

(a)

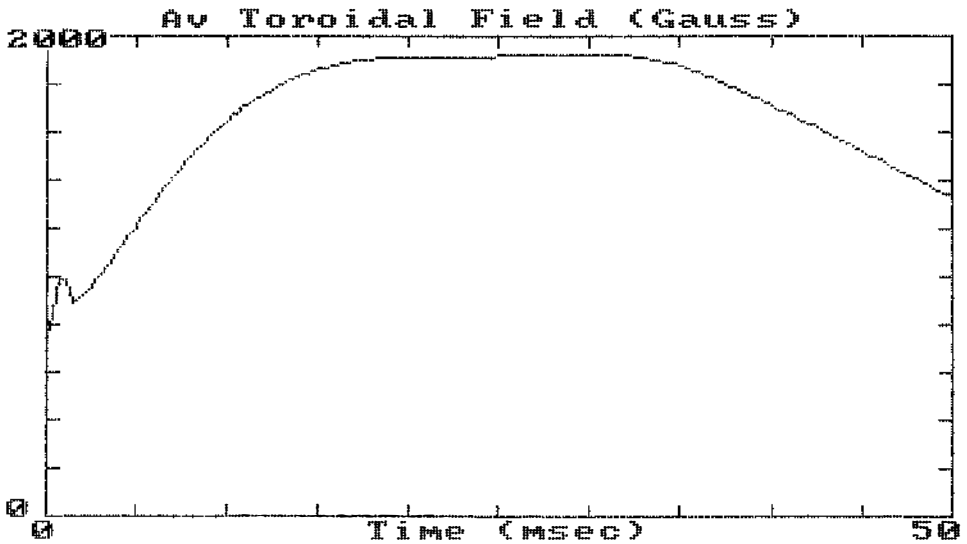

(b)

Fig. 3.4.4: Electrical waveforms for baseline design case.

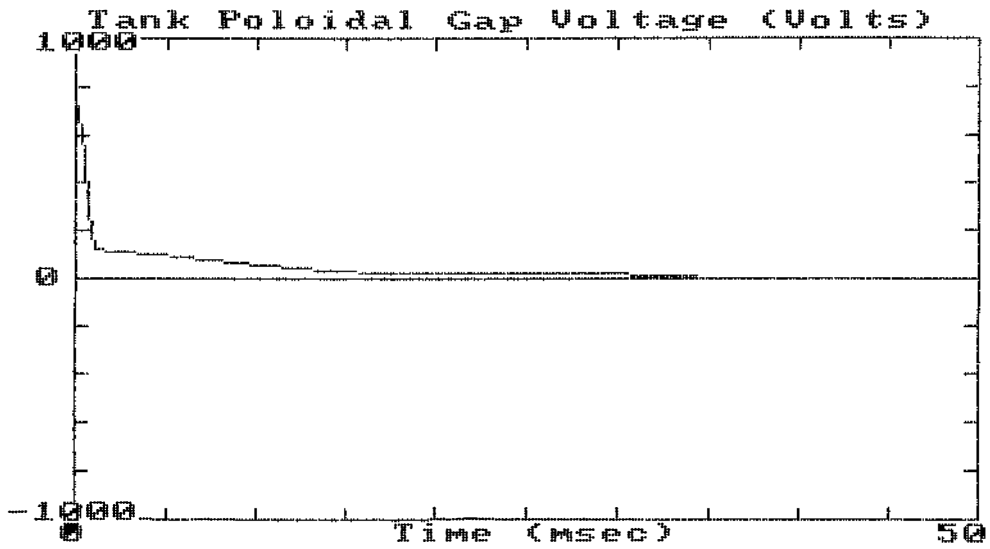
Tank Poloidal Gap Voltage (Volts)
1000
0
-1000
0
Time (msec)
50

(c)

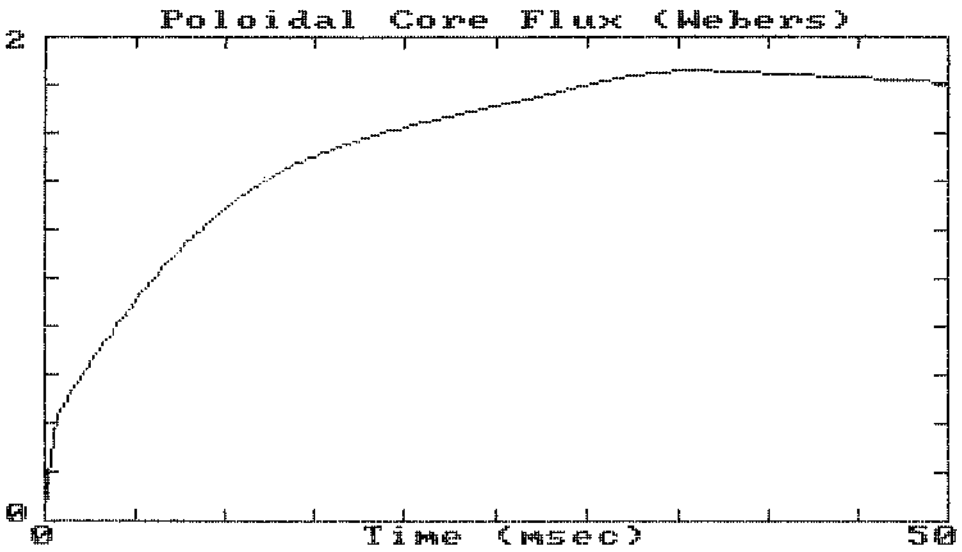
Poloidal Core Flux (Webers)
2
0
0
Time (msec)
50

(d)

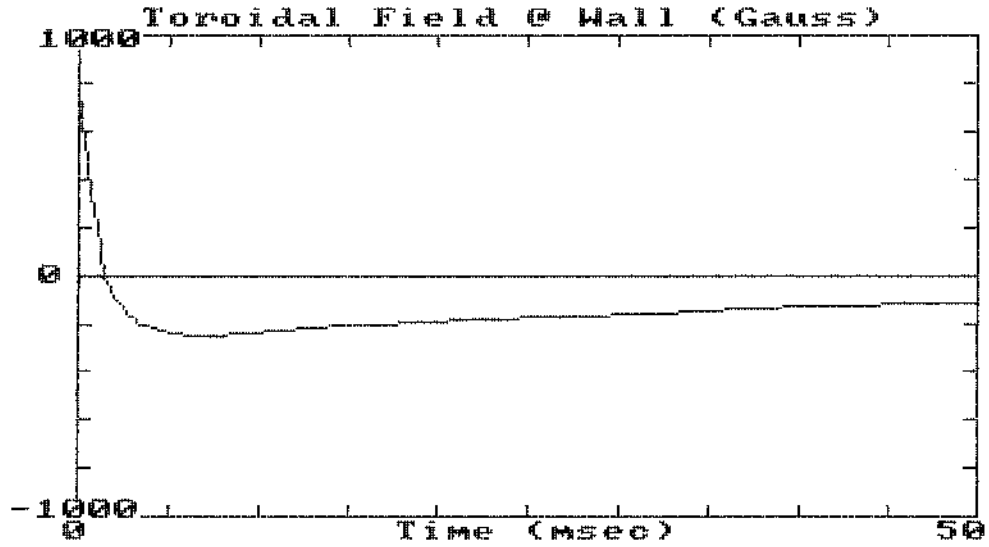
Toroidal Field @ Wall (Gauss)
1000
0
-1000
0
Time (msec)
50

(e)

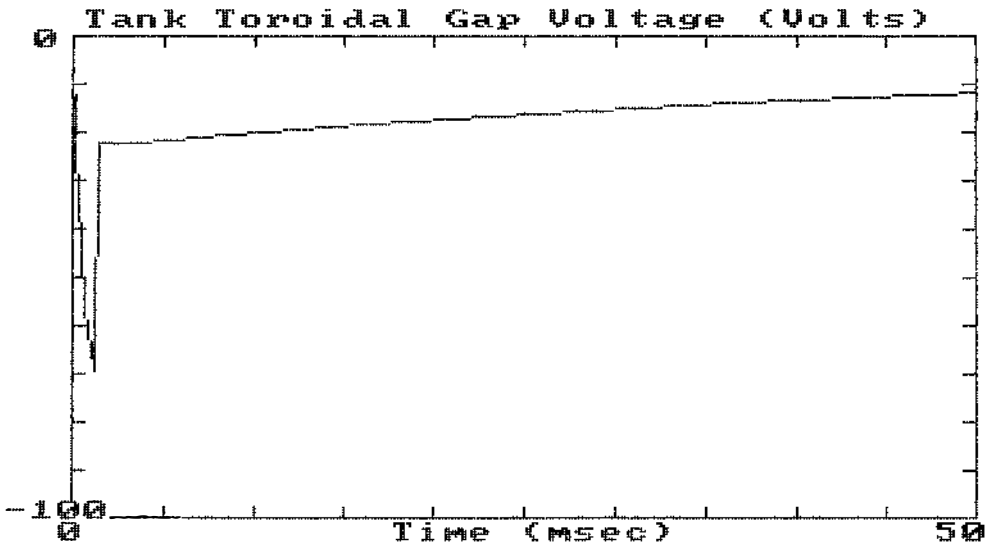
Tank Toroidal Gap Voltage (Volts)
0
-100
0
Time (msec)
50

(f)

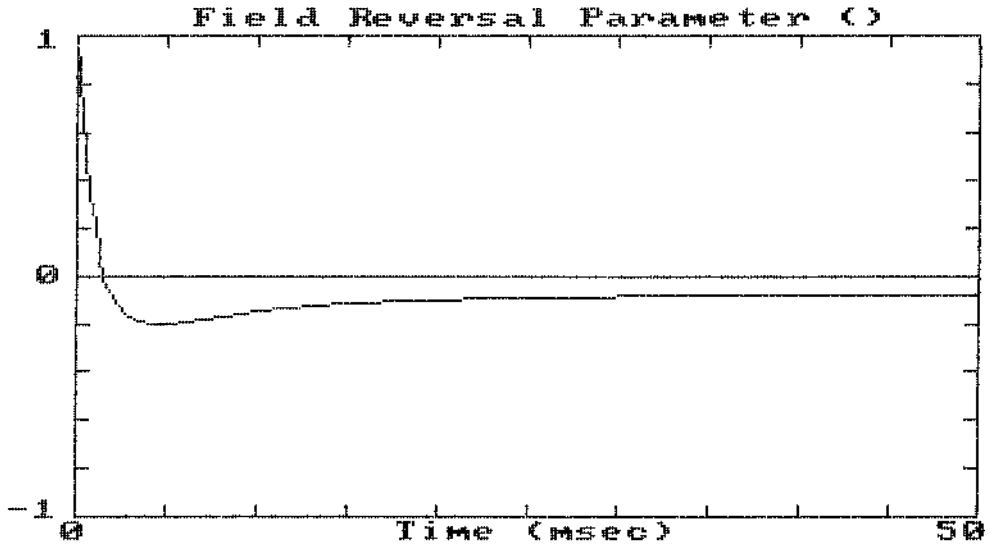
Field Reversal Parameter ()
1
0
-1
0
Time (msec)
50

(g)

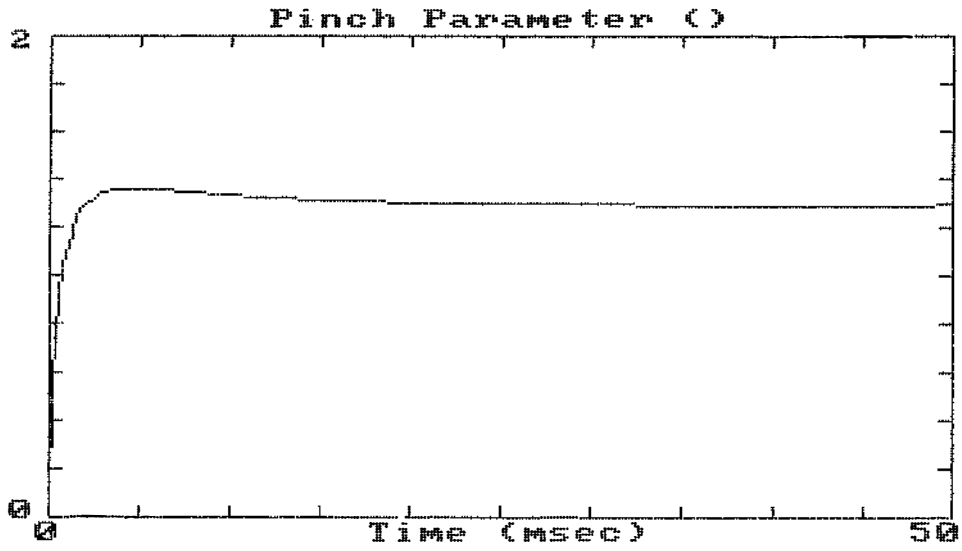
Pinch Parameter ()
2
0
0
Time (msec)
50

(h)

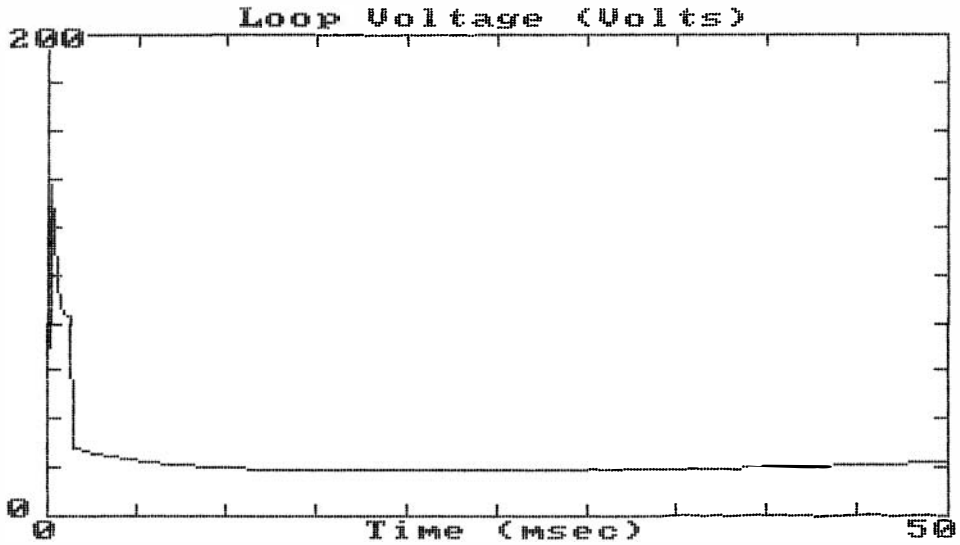
Loop Voltage (Volts)
200
0
0
Time (msec)
50

(i)

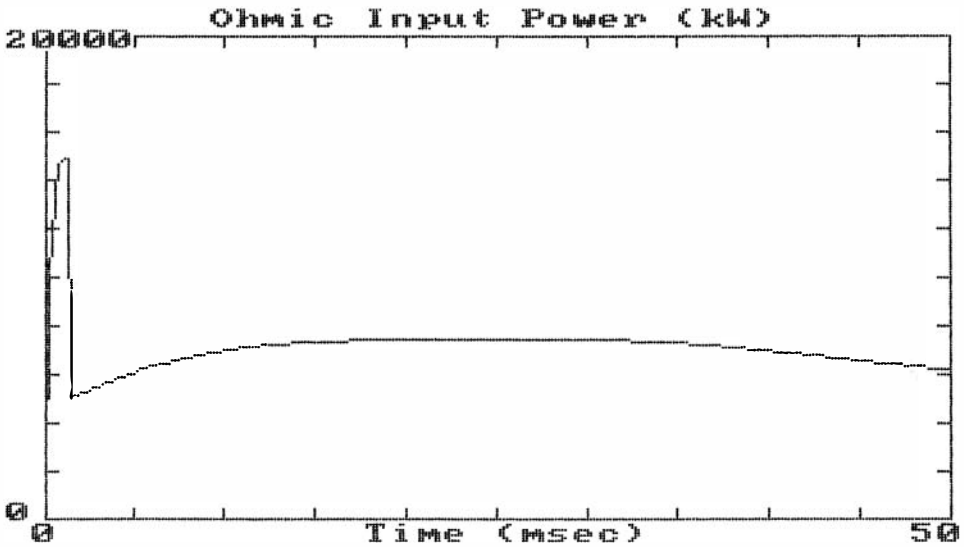
Ohmic Input Power (kW)
20000
0
0
Time (msec)
50

(j)

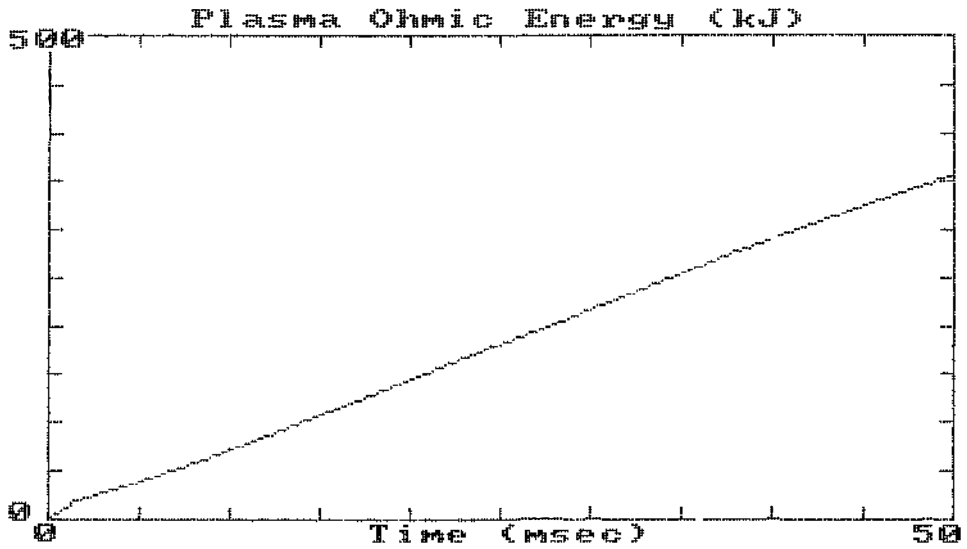
Plasma Ohmic Energy (kJ)
500
0
0
Time (msec)
50

(k)

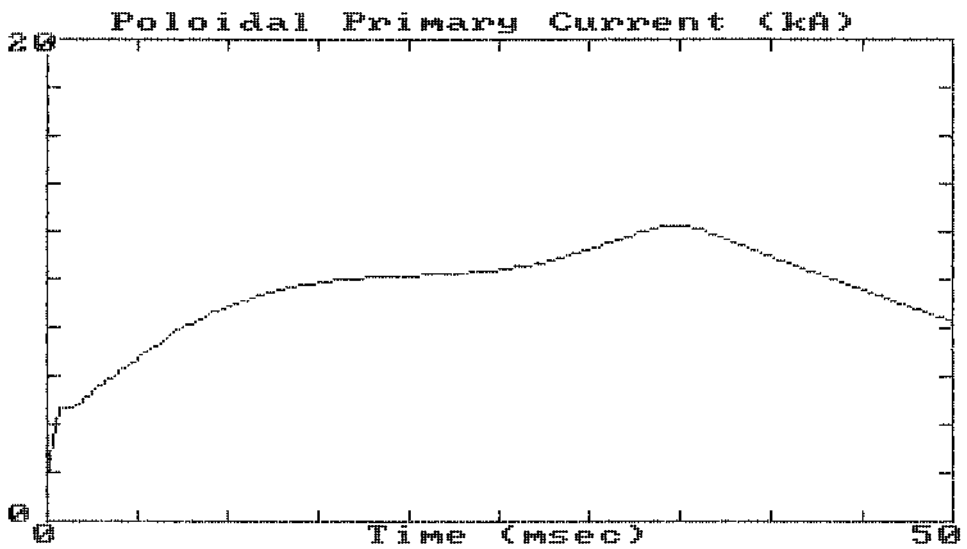
Poloidal Primary Current (kA)
20
0
0
Time (msec)
50

(l)

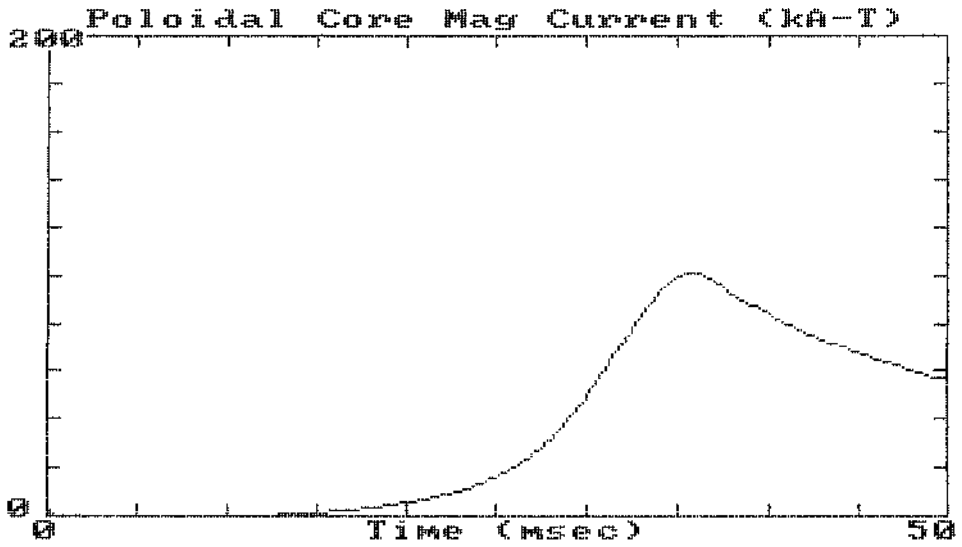
Poloidal Core Mag Current (kA-T)
200
0
0
Time (msec)
50

(m)

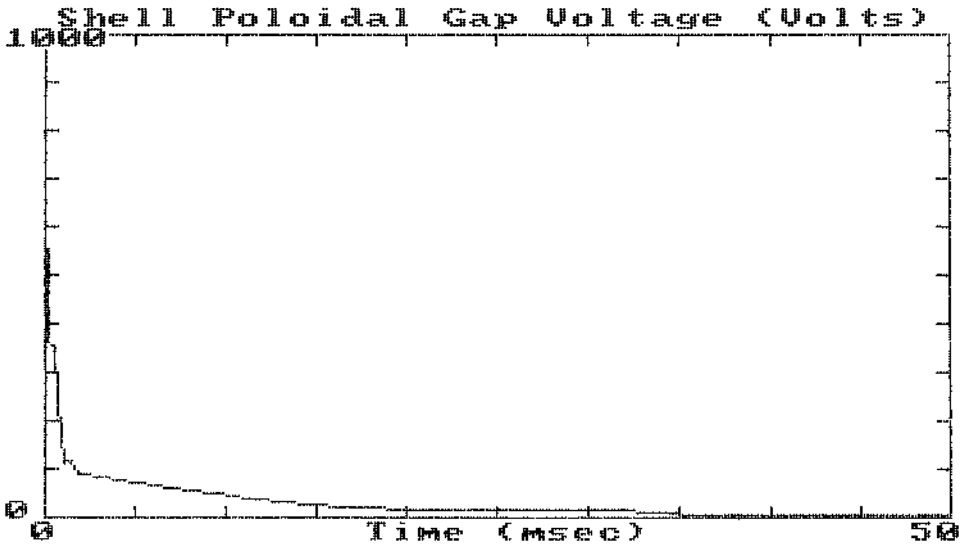
Shell Poloidal Gap Voltage (Volts)
1000
0
0
Time (msec)
50

(n)

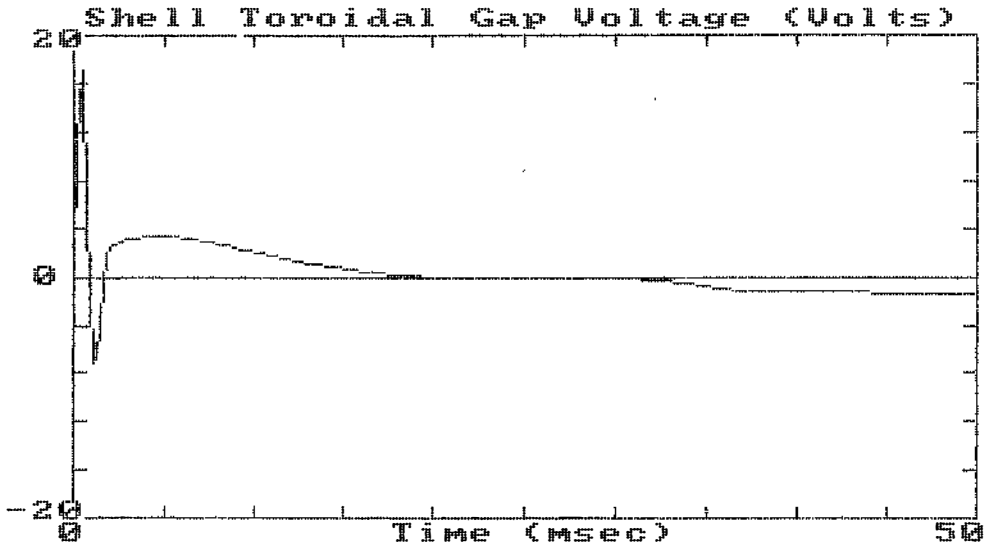
Shell Toroidal Gap Voltage (Volts)
20
0
-20
0
Time (msec)
50

(o)

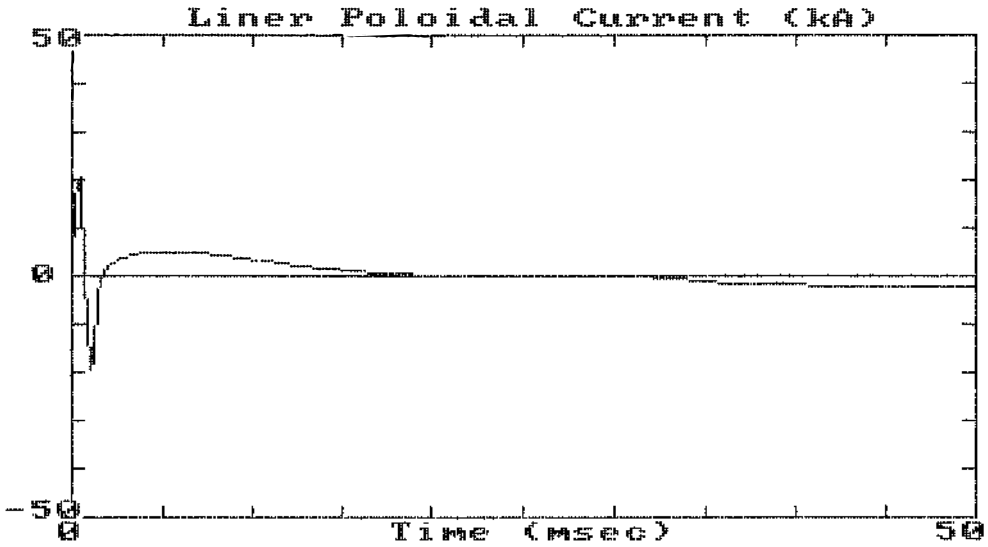
Liner Poloidal Current (kA)
50
0
-50
0
Time (msec)
50

(p)

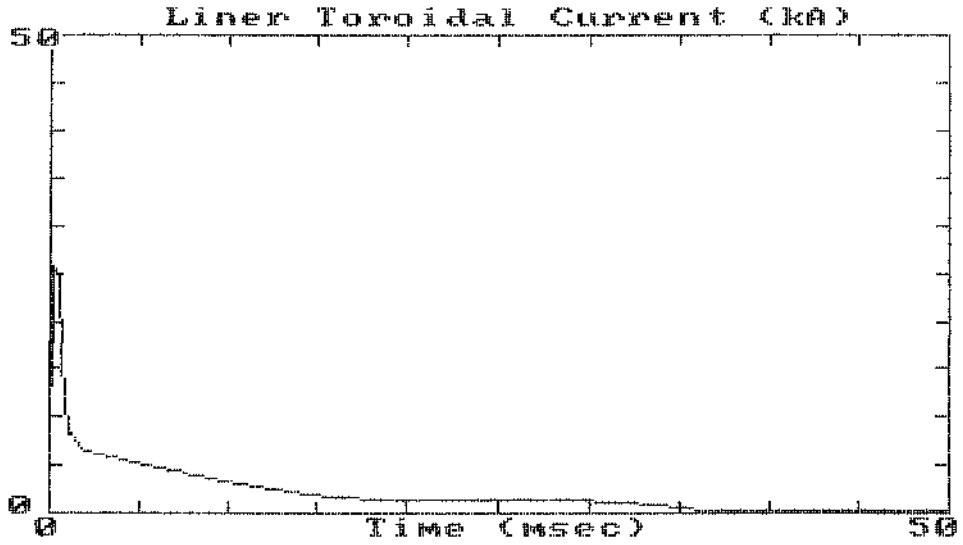
Liner Toroidal Current (kA)
50
0
0
Time (msec)
50

(q)

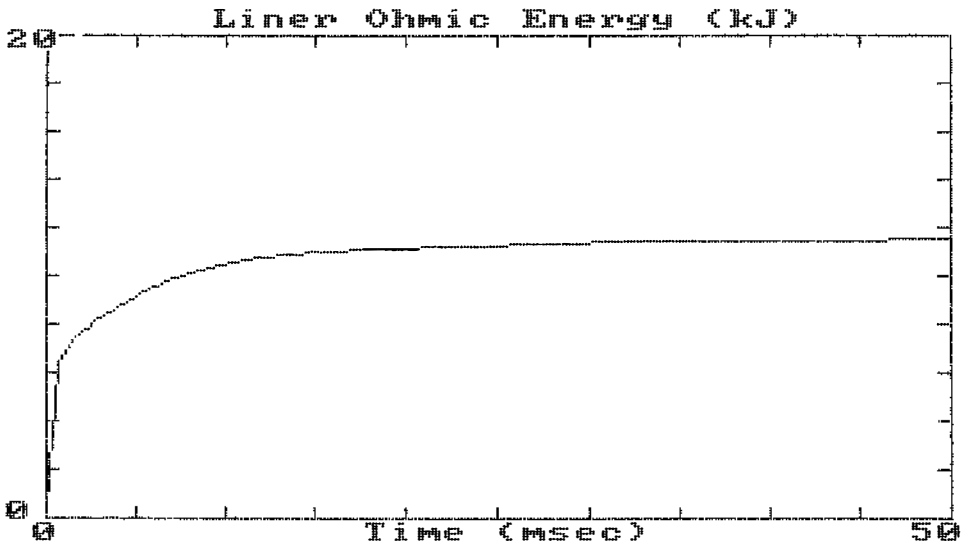
Liner Ohmic Energy (kJ)
20
0
0
Time (msec)
50

(r)

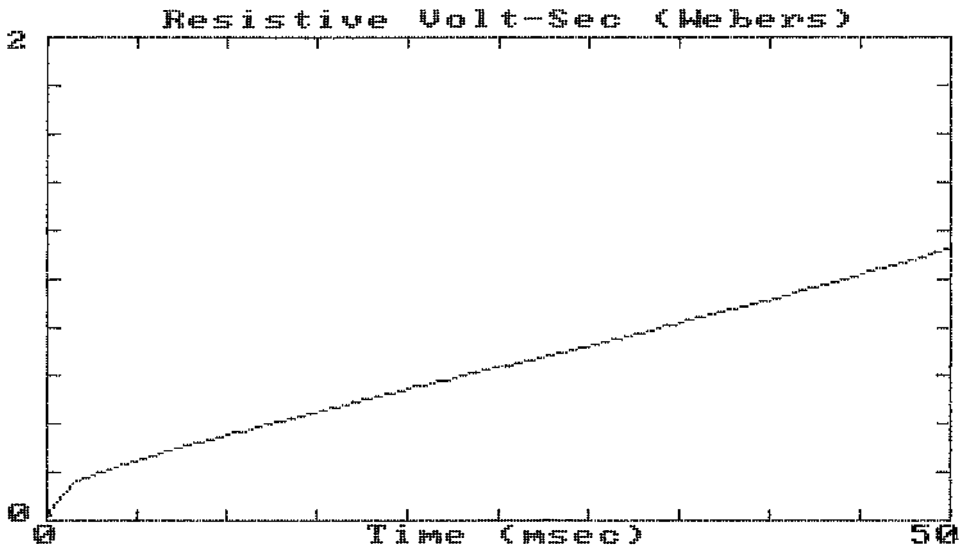

(s)

pulse length, the case shown has been used as a baseline design since it represents our best estimate of the maximum performance of the machine with an a = 32 cm radius liner and R_o = 1.56 meters. It also requires minimal modification of our existing capacitor banks. The baseline case has a 40:1 turns ratio on the poloidal field core so as to provide 750 volts/turn of startup voltage.

3.4.3 Alternate Waveforms

In an attempt to bracket the range of expected performance, we have examined a large number of alternate cases. For example, if the plasma resistance, both during startup and during the flat top were a factor of two higher than expected (corresponding approximately to no a^2/R_o enhancement over ZT-40), the resulting plasma current and core flux waveforms would be as shown in Fig. 3.4.5. This case requires a flux swing of 2.0 volt-sec and draws a peak core magnetizing current of 600 kA-turns.

We have also examined the case of discharging all capacitor banks at their full rated voltage into the machine with no plasma present to ensure that peak currents, mechanical stresses, thermal loads, etc. are tolerable. The general strategy has been to place enough impedance in the transformer primaries to prevent destruction of all components. Figure 3.4.6 shows the poloidal primary current, the currents in the liner, and the ohmic energy deposited in the liner. The toroidal field system is little affected by the plasma.

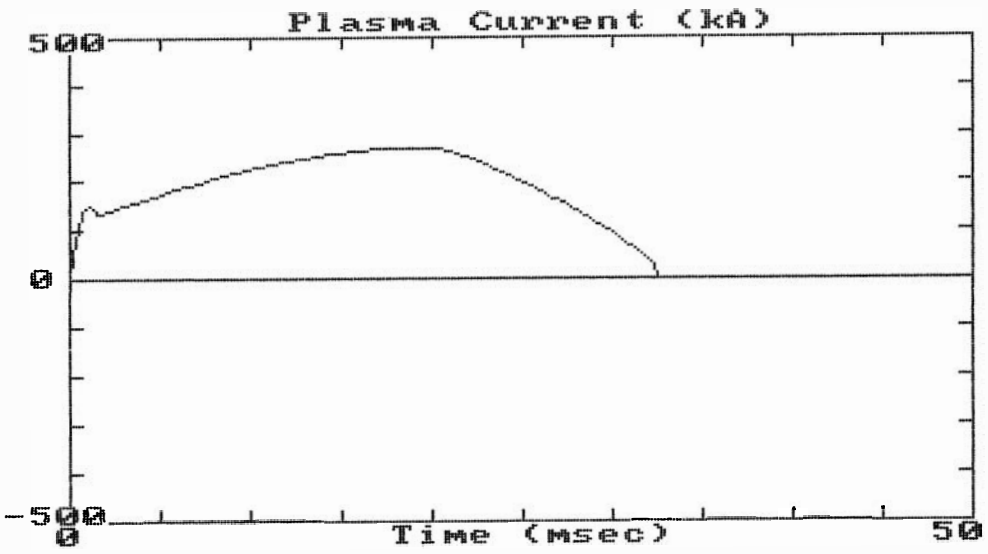

(a)

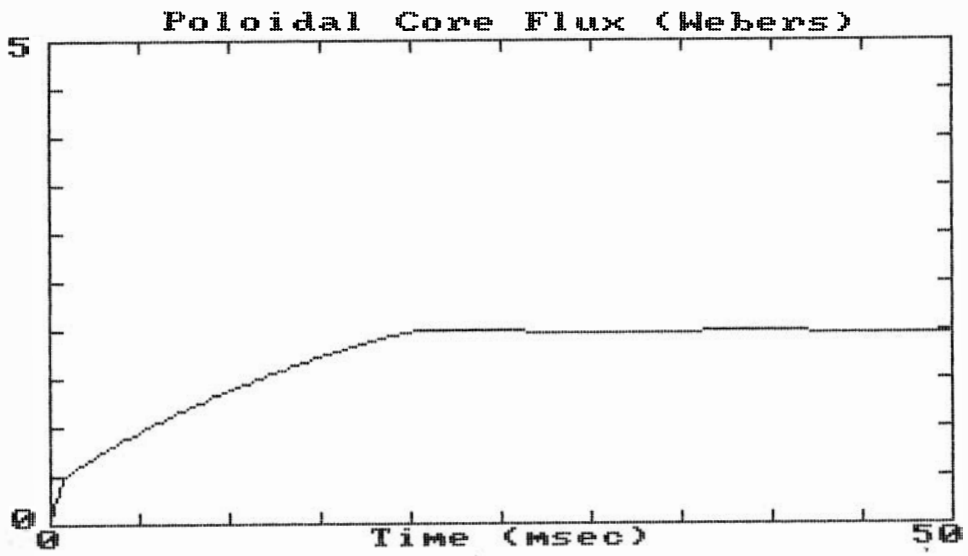

(b)

Fig. 3.4.5: Plasma current (a) and poloidal core flux (b) for a pessimistic case in which the plasma resistance in twice the expected value.

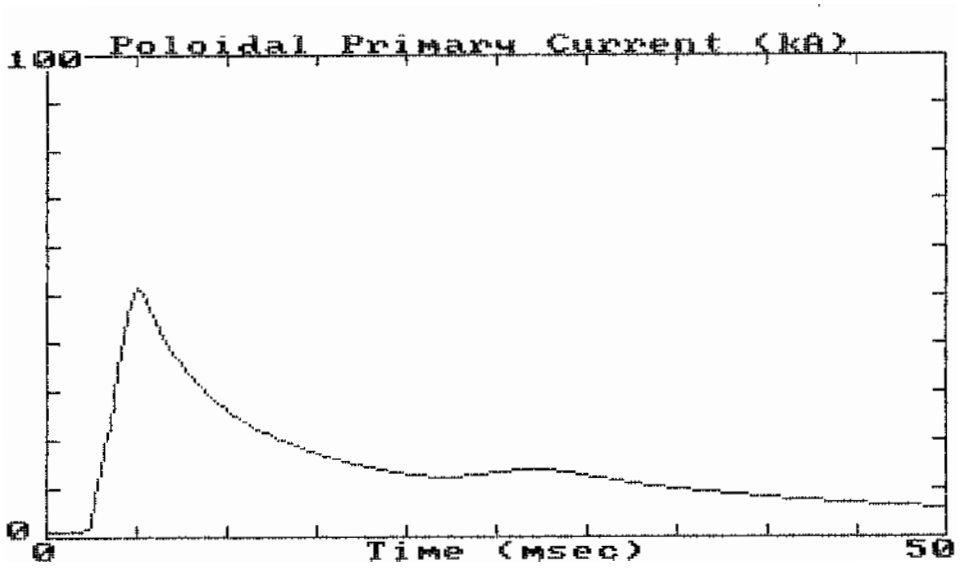

(a)

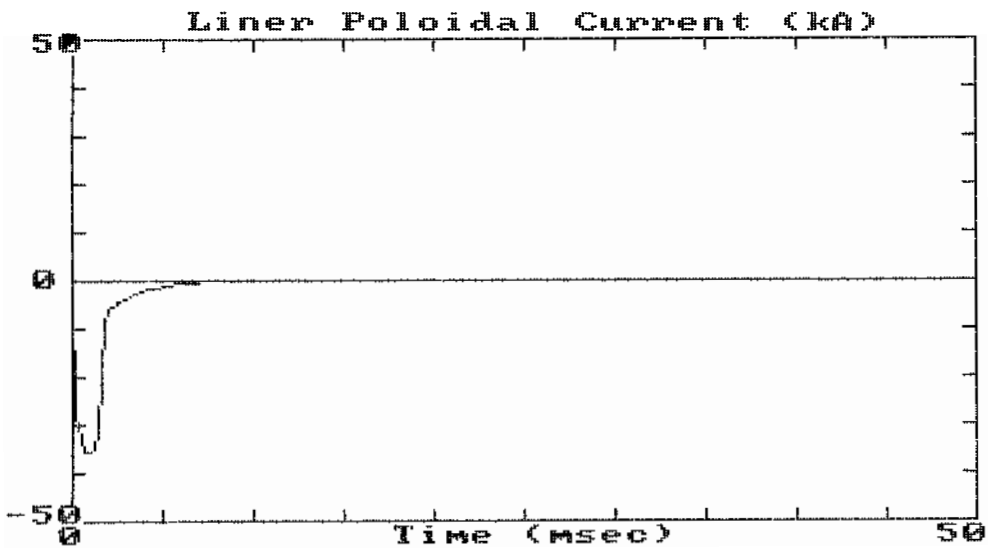

(b)

Fig. 3.4.6: Electrical waveforms for a case in which the capacitor banks are discharged into the machine at full voltage with no plasma present.

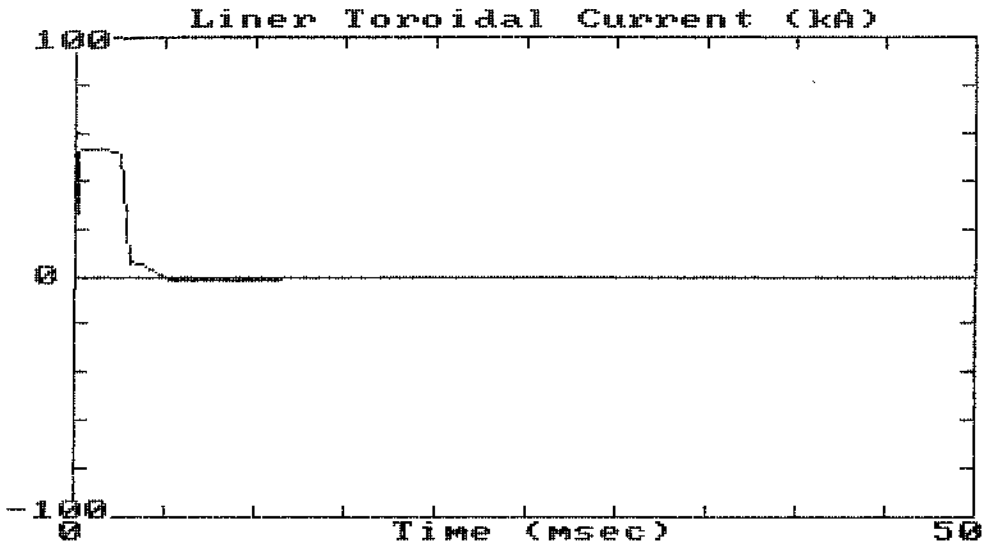
Liner Toroidal Current (kA)
100
0
-100
0
Time (msec)
50

(c)

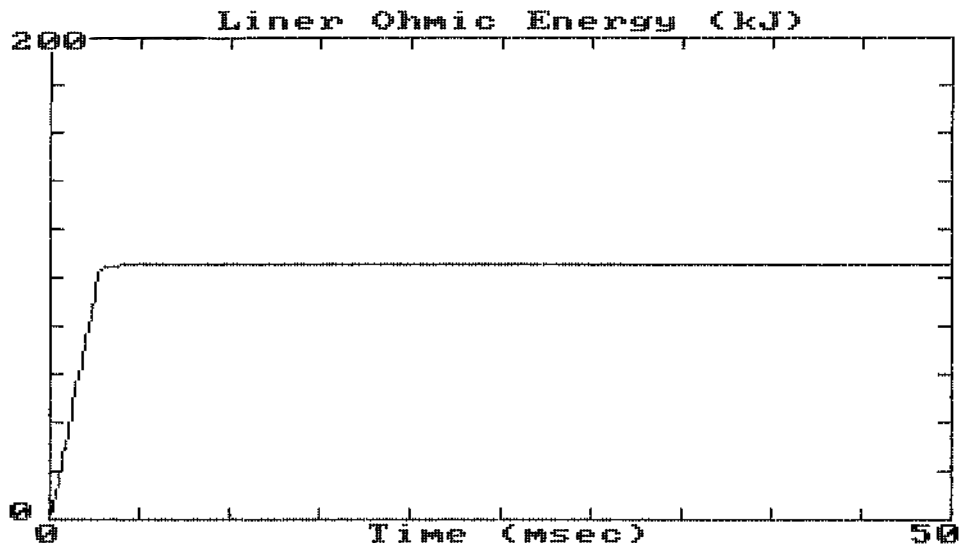
Liner Ohmic Energy (kJ)
200
0
0
Time (msec)
50

(d)

Finally, in Fig. 3.4.7 we show the case of a full a = 52 cm radius, R_o = 1.5 meter plasma (no shells). For this case, the inductance L_{P2} and resistance R_{P2} in Fig. 3.4.1 have been removed so that the plasma current rises to 800 kA and then decays with the L/R of the plasma after the current peak which is typically 60 msec. This case is energy-limited rather than flux-limited, and so one could achieve somewhat higher currents (~1 MA) if the poloidal capacitor bank were enlarged.

3.4.4 Volt-second Requirements and Limits

The volt-seconds required for a given plasma discharge can be divided into three parts: 1) inductive, 2) resistive during startup (when F > 0), and 3) resistive during ramp-up and flat-top.

The inductive part has been estimated by scaling from ZT-40 and from our own flux plot calculations assuming reasonable current profiles (see Sec. 3.4.6). The results are virtually the same and lead to an inductance of 1.7 μH inside the liner and 1.0 μH outside the liner (ignoring flux which has soaked into the shell and vacuum chamber wall). Thus for a 400 kA discharge, we require 1.08 webers for the inductive part.

The resistive startup volt-second requirement is scaled from ZT-40 according to

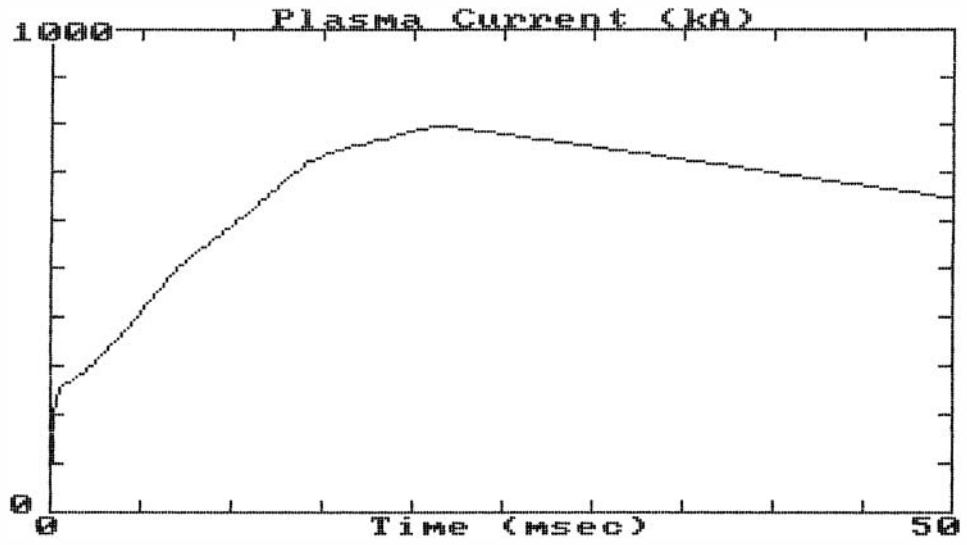

(a)

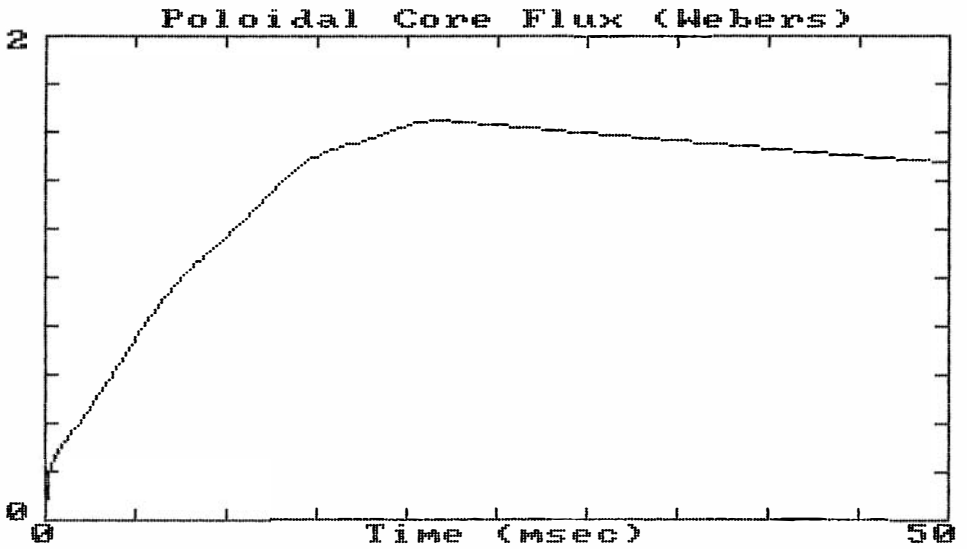

(b)

Fig. 3.4.7: **Plasma current (a) and poloidal core flux** (b) for a full **a = 52 cm radius.**

$$\Delta\Phi = 3 \times 10^{-5} \hat{I}_\phi R_o \tau_R / a^2$$

where $\hat{I}_\phi$ is the peak plasma current, τ_R is the current risetime, and all units are MKS. If we apply this formula up to the time of reversal (τ_R = 1.5 msec) where $\hat{I}_\phi$ = 185 kA, we predict ~0.13 volt-seconds. In the circuit simulation, the initial resistance was chosen to give about this volt-second consumption as described in Sec. 3.4.1.

The remaining 0.8 volt-seconds is thus available for the ramp-up and flat-top. If we can run with a loop voltage of 20 volts (a reasonable extrapolation from ZT-40 assuming resistance scales as R_o/a^2), we can achieve a nominal 40 msec pulse length.

The ultimate performance of the machine (especially peak plasma current and pulse length) is determined principally by the flux limit of the iron core in the poloidal field circuit. The physical dimensions of the core have been carefully measured and are given in Fig. 3.4.8. The manufacturer's specification for the magnetic properties of the iron are shown in Fig. 3.4.9. Over the range of interest ($B \gtrsim 1$ tesla), the magnetizing current is an approximate exponential function of the flux as indicated by the straight line in Fig. 3.4.9.

The electrical characteristics of the core were also measured experimentally. This was done by discharging a 0.048 farad capacitor bank that could be charged to 5 kV (600 kJ) into a 32-turn primary

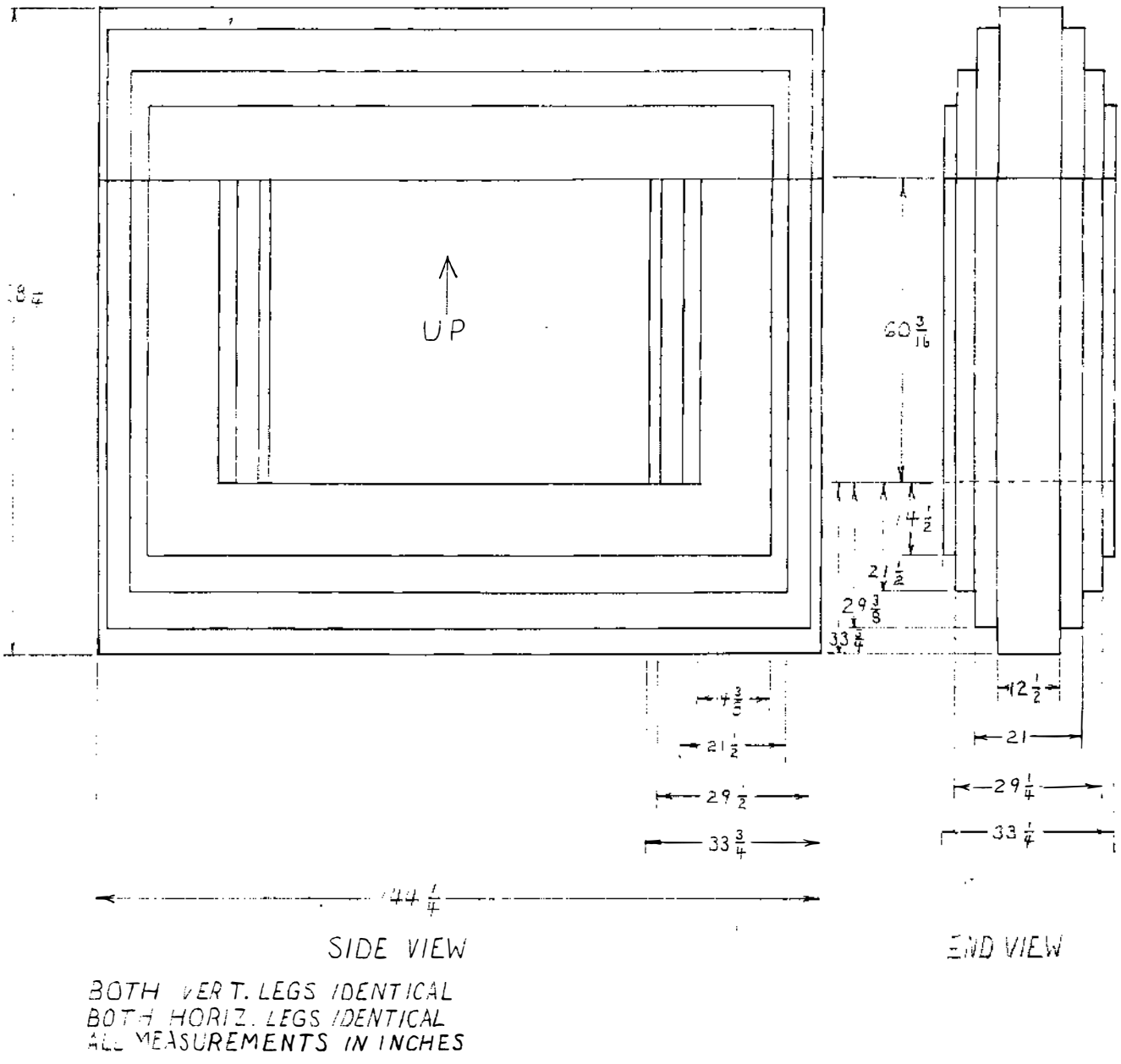

Fig. 3.4.8: Physical dimensions of the poloidal iron core.

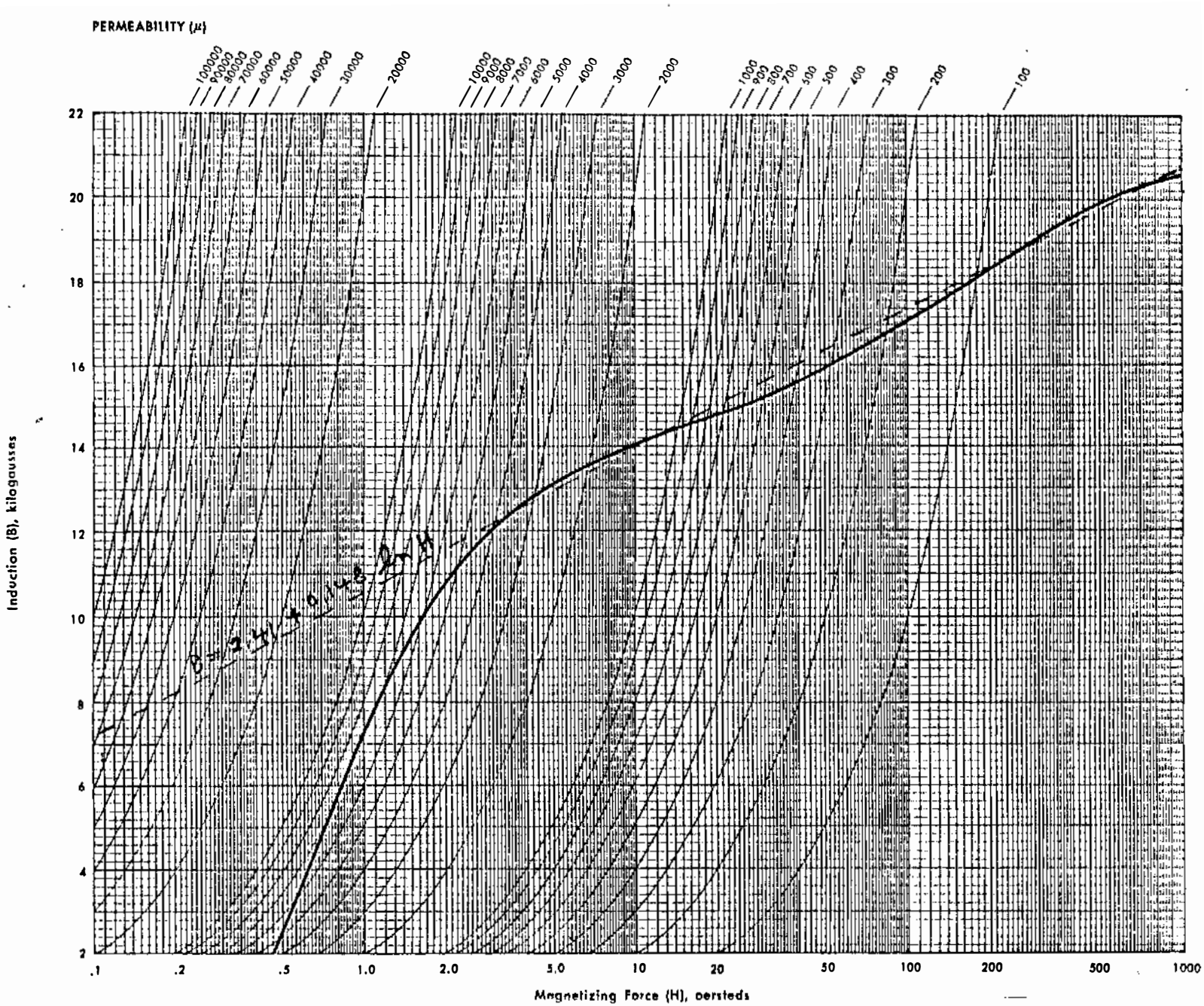

Fig. 3.4.9: DC Magnetization Curve for 26 and 24 gage M-19, AL Transformer C

winding on the core in the absence of plasma or other secondary currents. The primary current was measured by monitoring the voltage across a 50μΩ shunt, and the core flux was measured by passively integrating the voltage across a single-turn loop around the core. The current and flux measurements were calibrated to an accuracy estimated as ±2%. Typical traces of the flux and current are shown in Fig. 3.4.10. The core was degaussed between pulses by means of a 12 volt battery that could provide ~100 amps × 32 turns. The remanent magnetization of the core was monitored by a Hall probe near the gap where the top leg of the core meets the outside leg. The remanent field was ≤350 gauss for the cases shown and led to a small (2%) correction to the data. From data of this sort the magnetization curve in Fig. 3.4.11 was constructed. Also shown in the figure is the theoretical expectation based on the manufacturer's B-H specification and the exponential fit used in the circuit simulation. From the data, we conclude that with a 1.5 tesla bias field, the core can be swung 2.0 volt-seconds with a magnetizing current of about 400 kA-turns.

3.4.5 Core Biasing

The selection of 1.5 tesla core bias represents a compromise between the desire to get the maximum flux swing and the rapidly increasing power requirements for the biasing circuit. From Fig. 3.4.9, it can be seen that 1.5 tesla requires about 30 oersteds or 24 kA-turns for a core length of 10 meters. With a 40-turn primary, we thus require 600 amps. A power supply is on hand that will provide 600 amps at 40 volts (24 kW). Thus, we are allowed a circuit

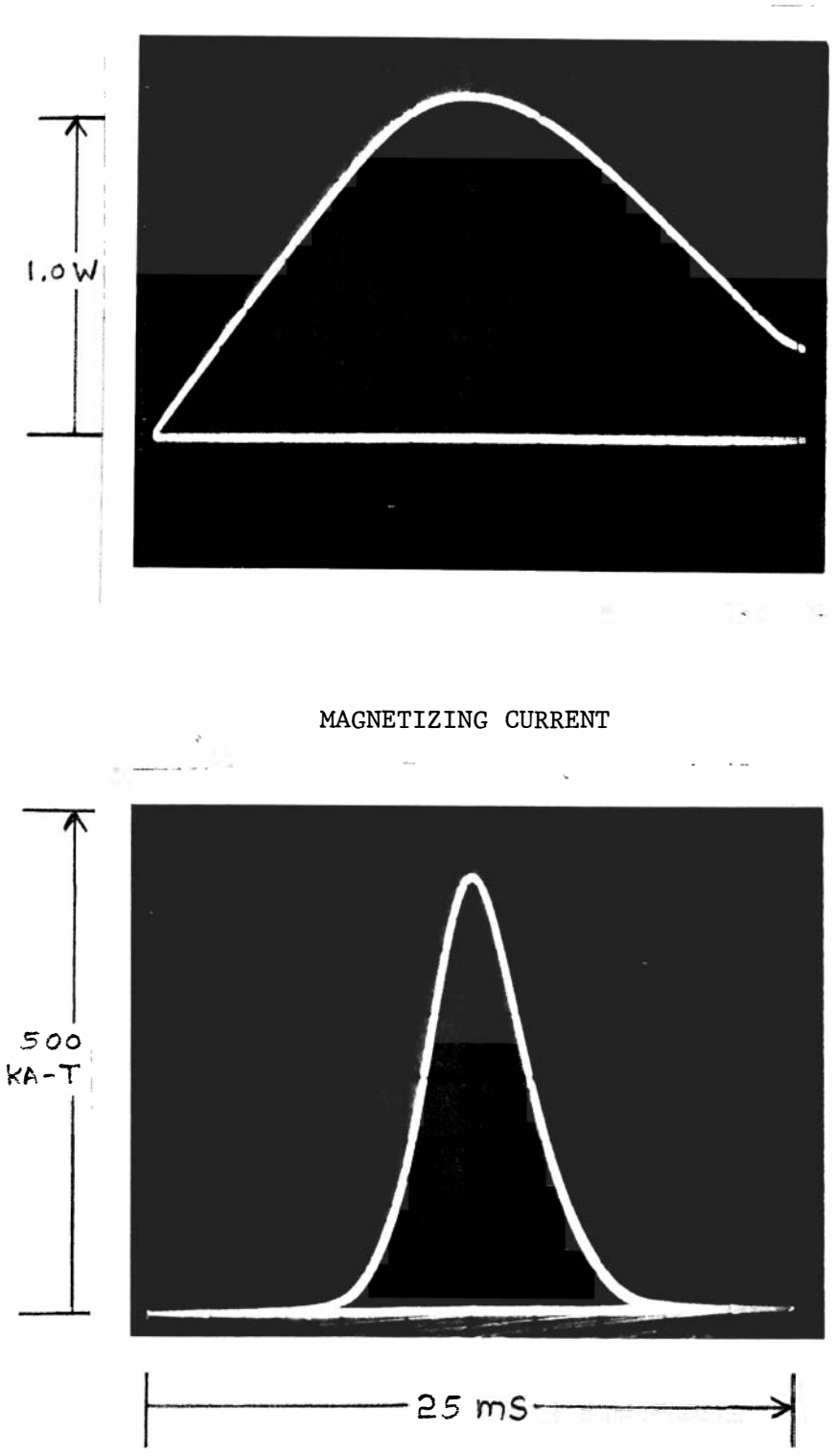

Fig. 3.4.10: Measurement of core flux and magnetizing current typical of that used to verify the electrical properties of the poloidal iron core.

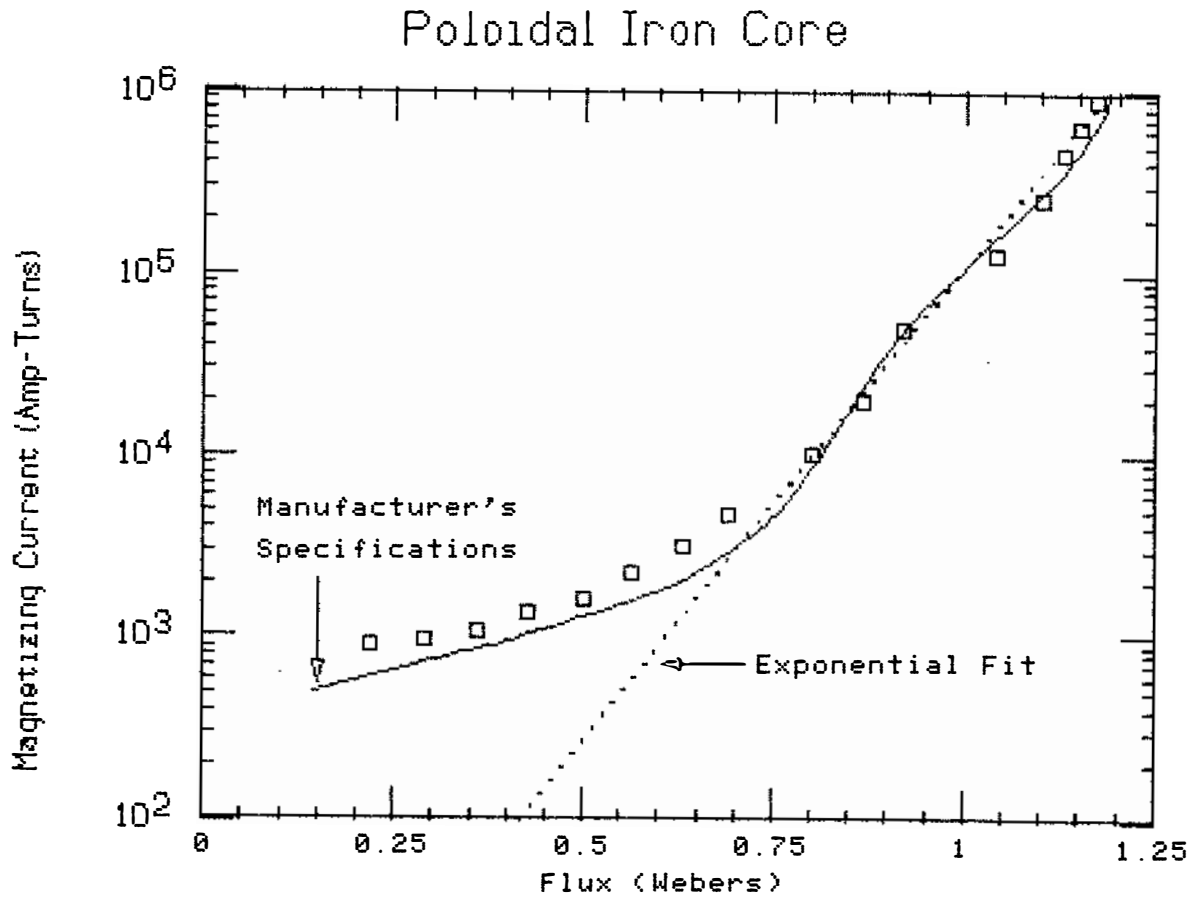

Fig. 3.4.11: Experimental measurements of the magnetizing current vs flux for the poloidal iron core compared with the manufacturer's specifications (solid line) and the exponential fit (dotted line) used in the circuit modeling.

resistance of ~67 mΩ. The most straightforward bias circuit would use an inductor of ~40 mH (so as to consume only 10% of the energy in the poloidal field bank) with 54 mΩ resistance (allowing 13 mΩ for the poloidal field primary). Such an inductor, if made 1 meter long × 2 meters in diameter using copper wire is estimated to cost ~$20K. Cooling of the inductor should not be a problem since the bias supply need only be on for 1-2 seconds out of every 3 minutes, and thus the average dissipation is ~100 watts.

One drawback of a dc bias scheme is that a dc field error is produced at the location of the plasma unless the bias windings are placed in the right location around the core (see Appendix III). This requirement precludes biasing through the same primary winding that is used for the pulsed current. Alternate schemes using pulsed biasing are under investigation, but they typically require an unacceptably large capacitor bank or a high current switch that opens under load.

3.4.6 Magnetic Flux Plots

3.4.6.1 Equations

To solve for the equilibrium state, we start with the magnetohydrostatic equilibrium equations:

$$\vec{\nabla} \cdot \vec{B} = 0$$

$$\vec{j} \times \vec{B} = \nabla P \quad .$$

Assuming axisymmetry, these equations can be reduced to the familiar Grad-Shafranov equation in toroidal geometry:

$$\frac{\partial^2\psi}{\partial r^2} - \frac{1}{r}\frac{\partial\psi}{\partial r} + \frac{\partial^2\psi}{\partial z^2} = -\mu_0 J_\phi r = -\mu_0 r^2 P'(\psi) - ff'(\psi) \qquad (1)$$

where $f = rB_\phi$, and the coordinate system in Fig. 3.4.12 is used.

$f(\psi)$ and $P(\psi)$ are not uniquely specified in ideal MHD theory. For a force-free, low-β state,

$$\vec{\nabla} \times \vec{B} = \lambda(r,z)\vec{B} \quad , \quad \vec{\nabla}P \to 0,$$

The the equations become:

$$\frac{\partial^2\psi}{\partial r^2} - \frac{1}{r}\frac{\partial\psi}{\partial r} + \frac{\partial^2\psi}{\partial z^2} = -\lambda(\psi)f(\psi) \qquad (2)$$

with $\lambda(\psi) = \frac{\partial f(\psi)}{\partial\psi}$.

$\lambda(\psi)$ is chosen to have the form:

$$\lambda(\psi) = C_1(\psi - \psi_{limit})^{C_2}$$

For $C_2 = 0$ we have the Taylor state, while $C_2 \neq 0$ represents more realistic profiles where $\lambda \to 0$ near the plasma edge where $\psi = \psi_{limit}$. (ψ_{limit} is defined by the vacuum tank or internal shell.)
$f(\psi)$ becomes:

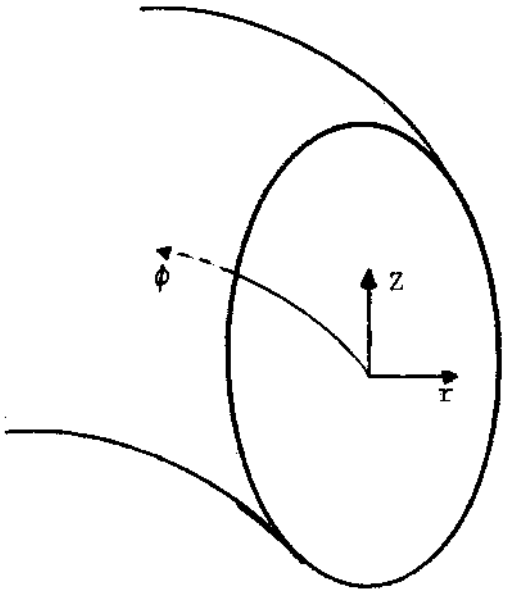

Fig. 3.4.12: Coordinate system used for magnetic flux plots.

$$f(\psi) = \frac{C_1(\psi-\psi_{limit})}{C_2+1} + C_3 \quad .$$

Given C_2, total plasma current, and B_ϕ at plasma edge as input, the constants C_1, C_2, and C_3 can all be determined directly or as function of Ψ. Then Eq. (2) is solved iteratively for a given device geometry. We solve for both force-free and finite pressure cases, but first illustrate the force-free case.

3.4.6.2 Examples

The examples in Figs. 3.4.13-3.4.16 show flux plots for some typical cases. The no-shell case has 1 MA of current while the thick shell and thin shell cases have 360 kA. Below the plots are profiles for B_ϕ, J_ϕ, P, and B_θ along the midplane, and λ along the midplane. Other diagnostics are displayed to the left. Simulations with non-zero pressure and various current profiles were also done as were field soak in effects by displacing the boundaries.

3.4.6.3 Inductance

Inductance as defined by

$$\frac{2 \times \text{poloidal field energy}}{(\text{toroidal current})^2}$$

is found to be $\approx$ 1.7 μH internally and 1 μH external to the plasma for the thin shell case at $\theta \approx 1.4$. Modeling of toroidal and poloidal

Constant λ, 360 kA with thin shell shifted 6 cm

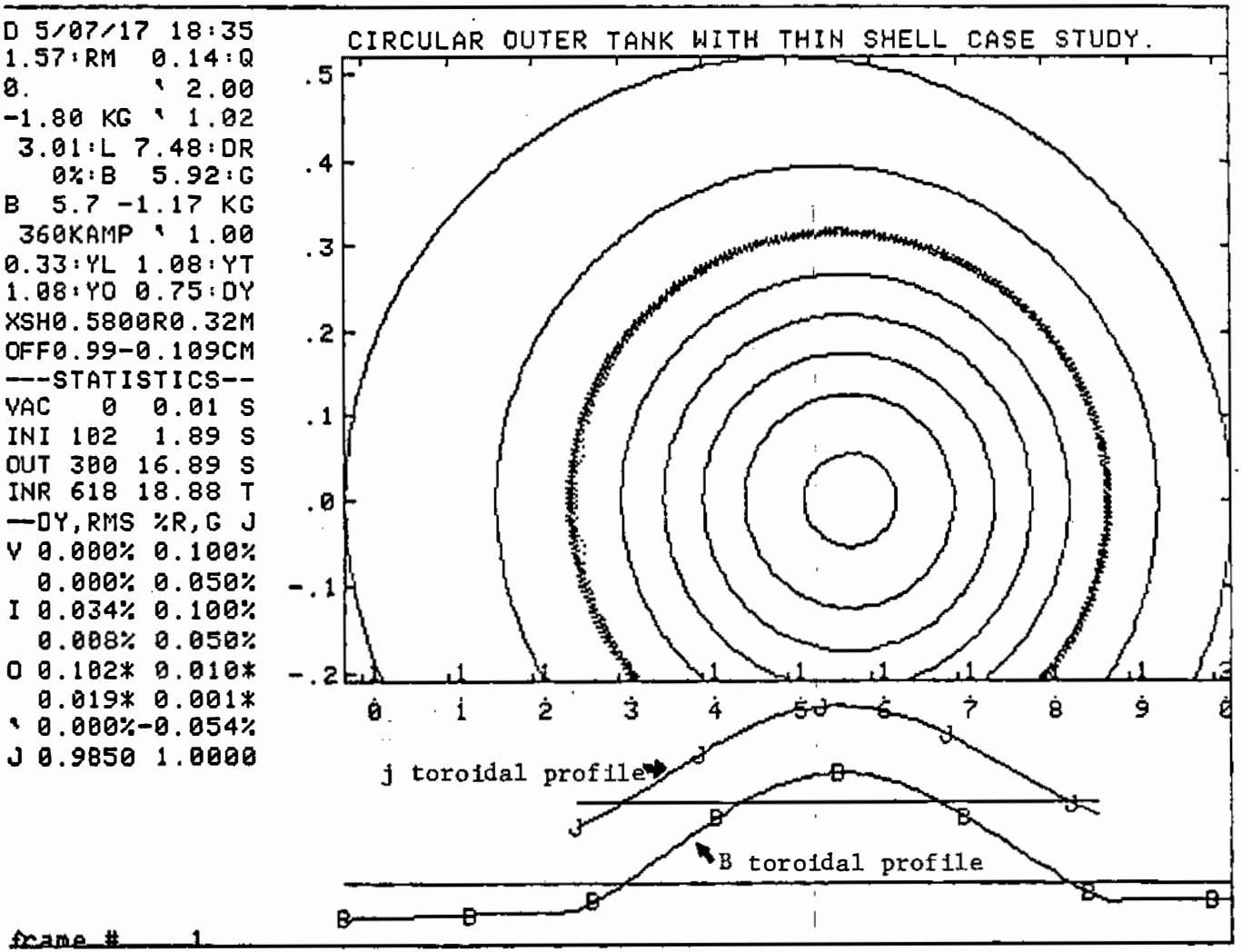

Fig. 3.4.13a

Mod. B plot for the constant λ case. λ, F, θ, and inductance data display also.

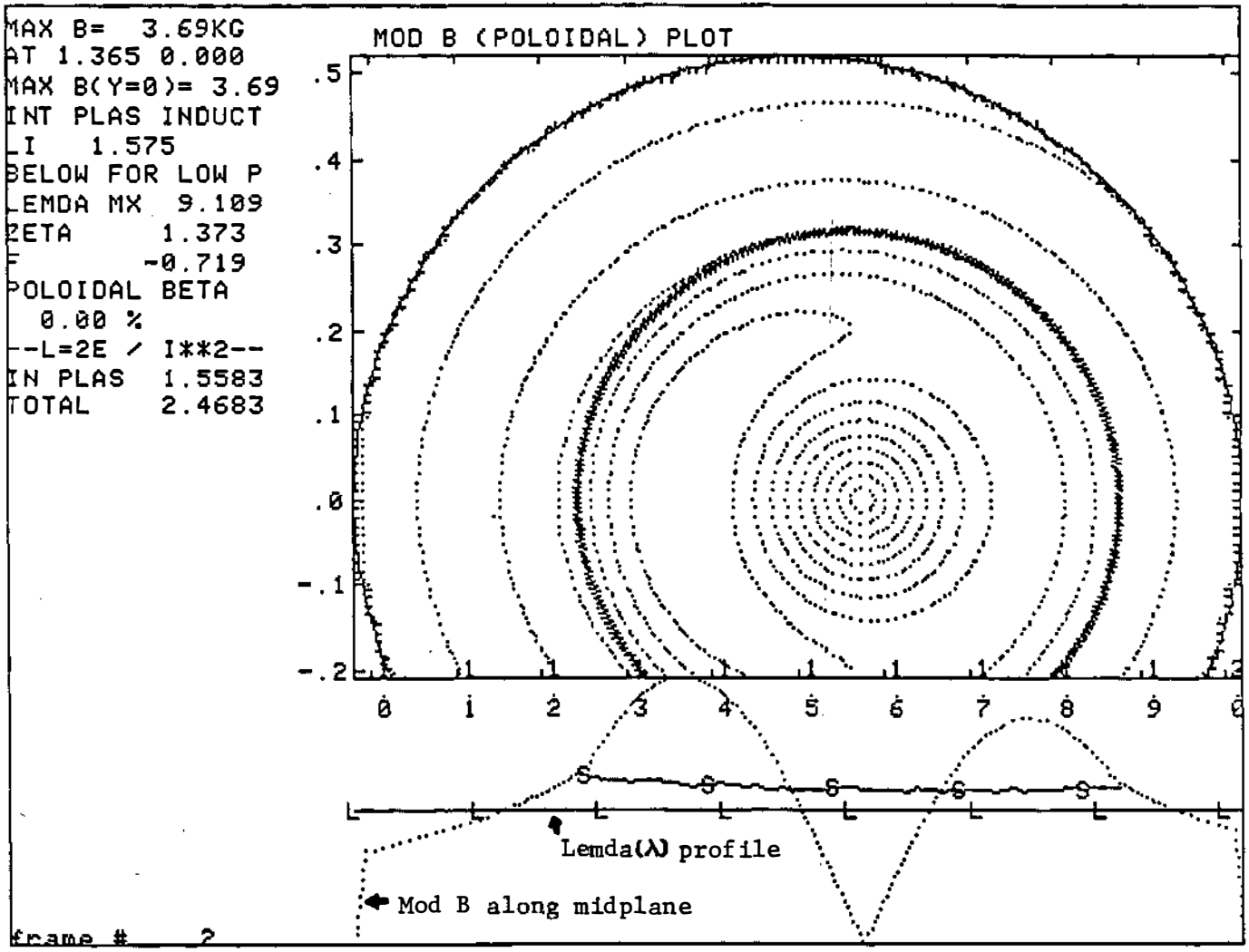

Fig. 3.4.13b

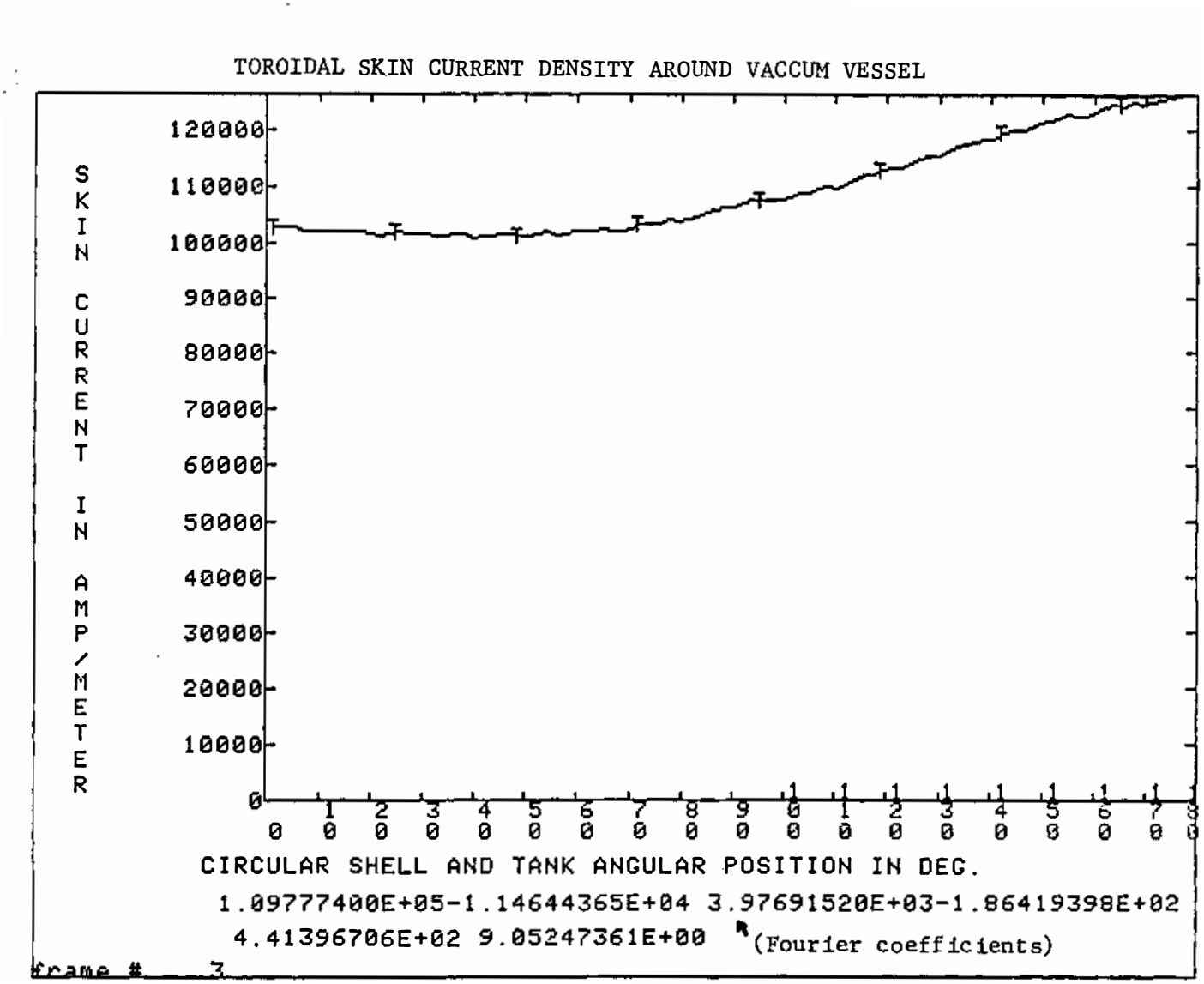
TOROIDAL SKIN CURRENT DENSITY AROUND VACCUM VESSEL
SKIN CURRENT IN AMP/METER
120000
110000
100000
90000
80000
70000
60000
50000
40000
30000
20000
10000
0
0 10 20 30 40 50 60 70 80 90 100 110 120 130 140 150 160 170 180
CIRCULAR SHELL AND TANK ANGULAR POSITION IN DEG.
1.09777400E+05-1.14644365E+04 3.97691520E+03-1.86419398E+02
4.41396706E+02 9.05247361E+00 (Fourier coefficients)
frame # 3

Fig. 3.4.13c:

1 MA case with no shell ($\lambda \alpha \psi^{0.1}$)

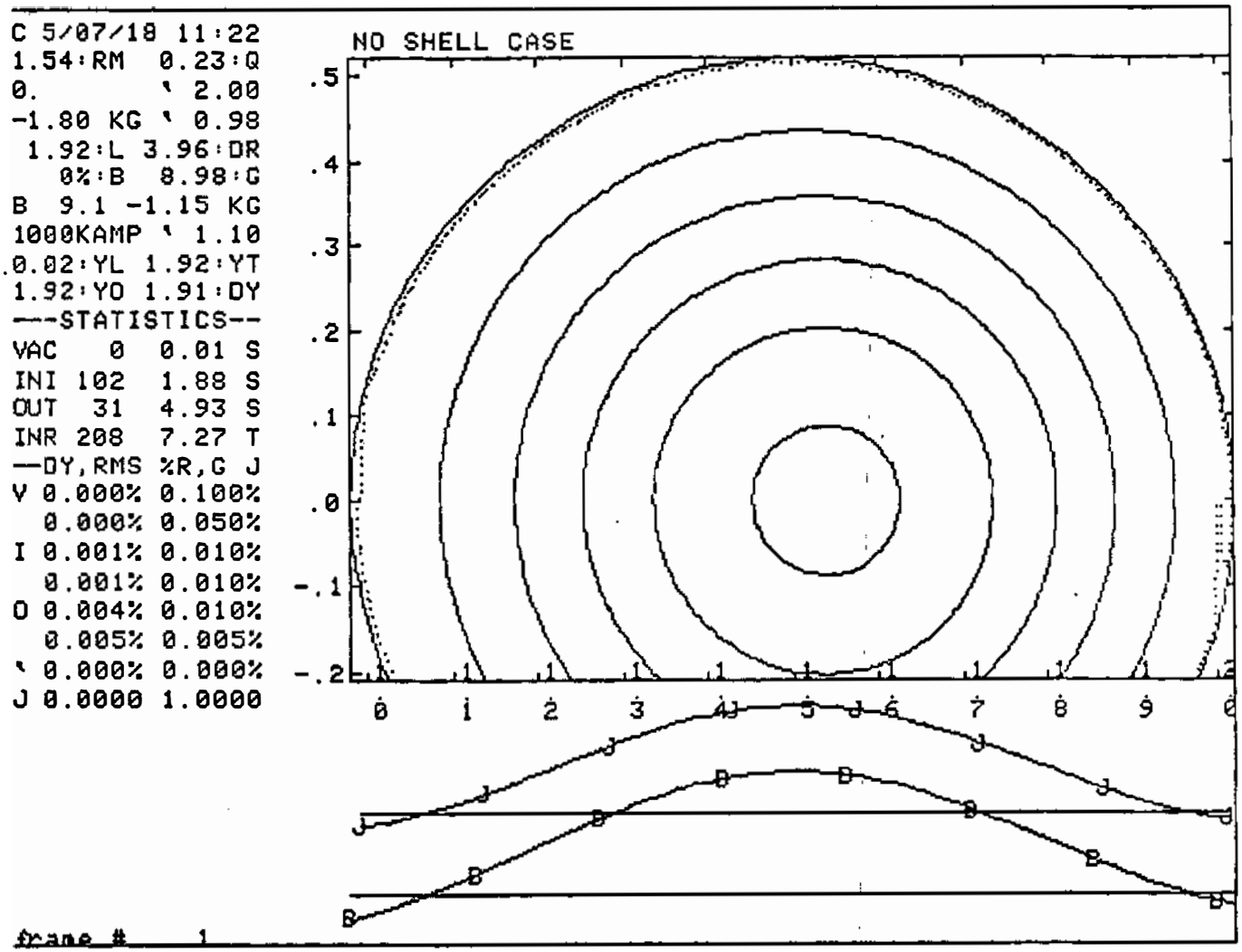

Fig. 3.4.14a

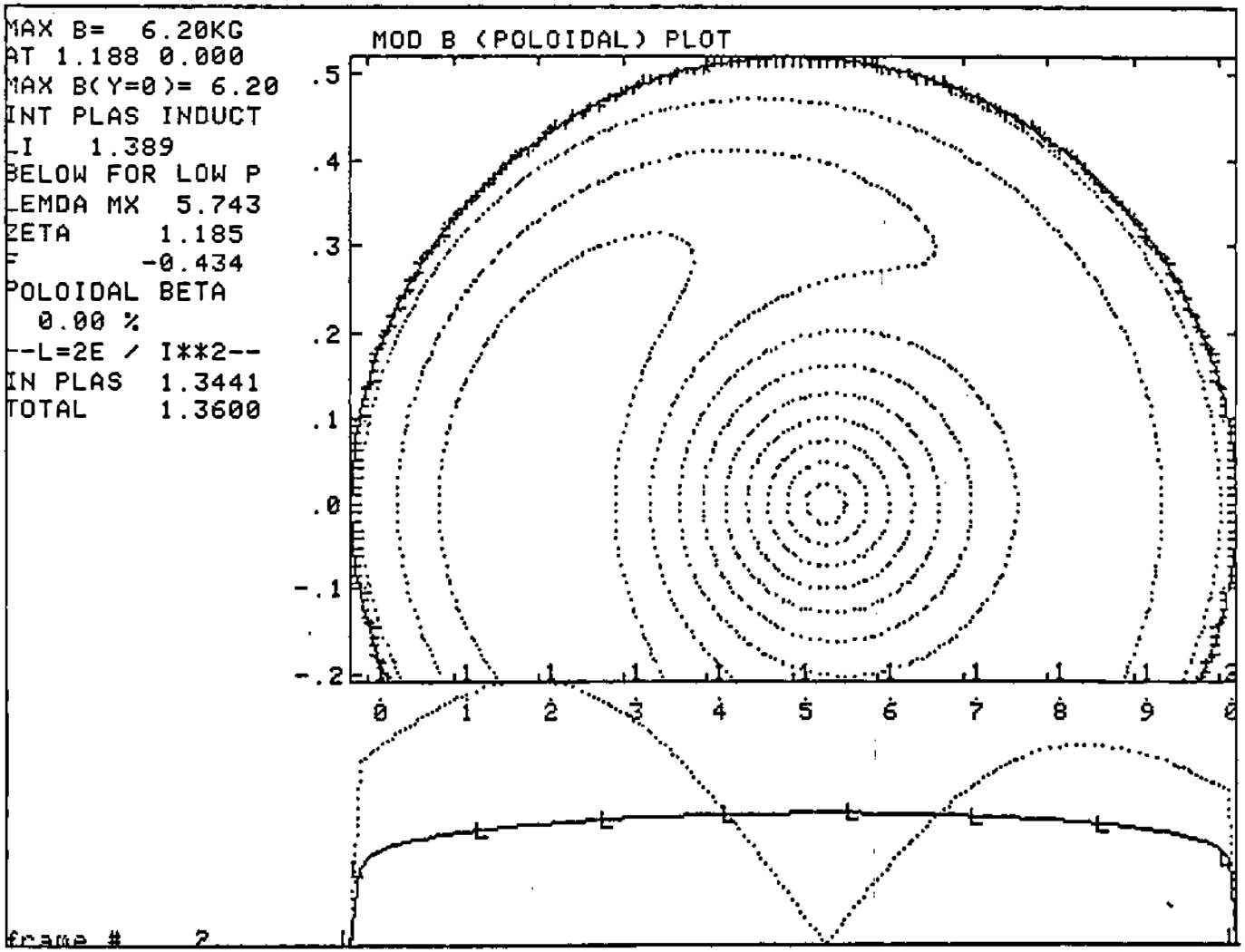
MAX B= 6.20KG
AT 1.188 0.000
MAX B(Y=0)= 6.20
INT PLAS INDUCT
LI 1.389
BELOW FOR LOW P
LEMDA MX 5.743
ZETA 1.185
F -0.434
POLOIDAL BETA
0.00 %
--L=2E / I**2--
IN PLAS 1.3441
TOTAL 1.3600
MOD B (POLOIDAL) PLOT
.5
.4
.3
.2
.1
.0
-.1
-.2
0 1 2 3 4 5 6 7 8 9 0
frame # 2

Fig. 3.4.14b

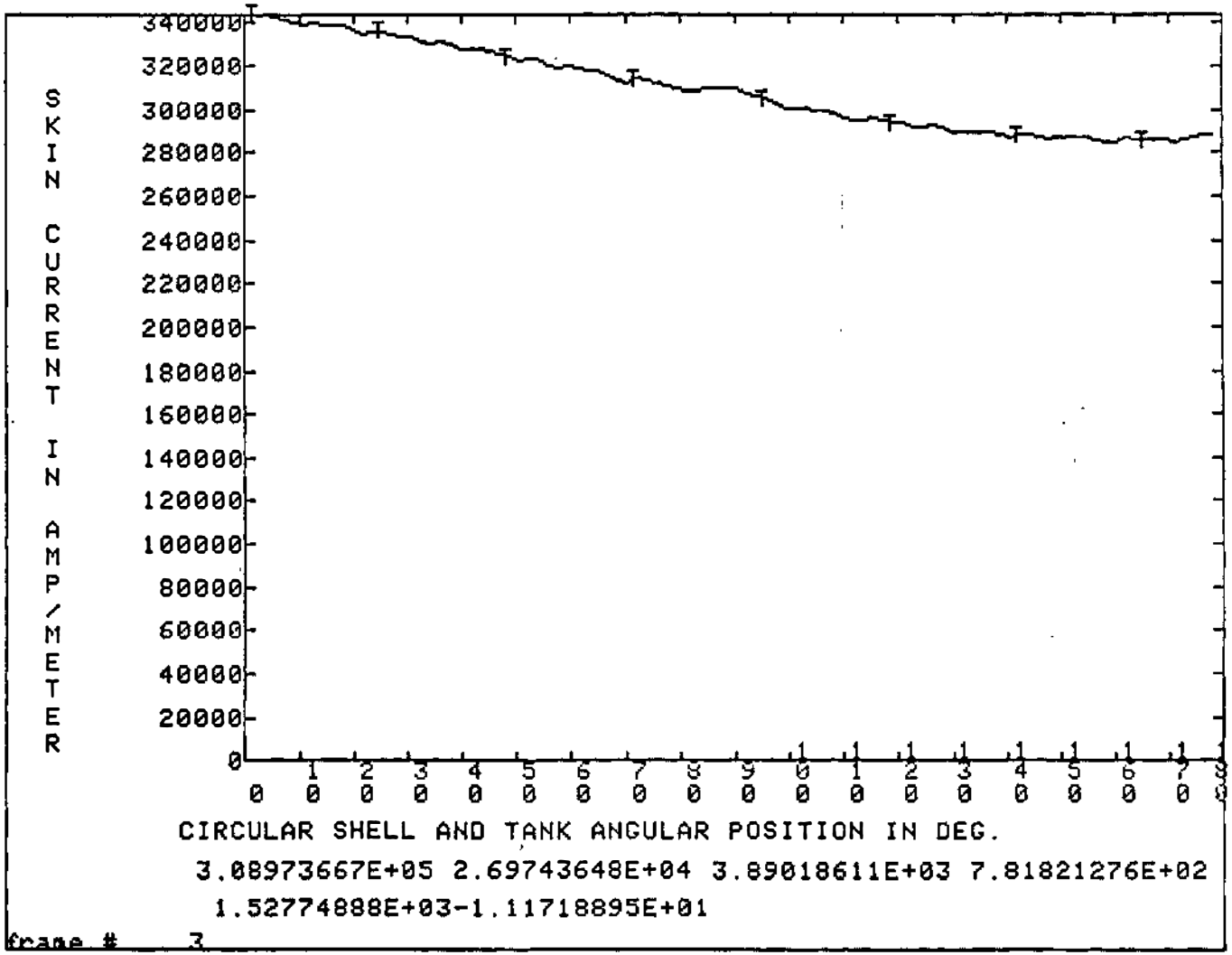
SKIN CURRENT IN AMP/METER
340000
320000
300000
280000
260000
240000
220000
200000
180000
160000
140000
120000
100000
80000
60000
40000
20000
0
0 10 20 30 40 50 60 70 80 90 100 110 120 130 140 150 160 170 180
CIRCULAR SHELL AND TANK ANGULAR POSITION IN DEG.
3.08973667E+05 2.69743648E+04 3.89018611E+03 7.81821276E+02
1.52774888E+03-1.11718895E+01
frame # 3

Fig. 3.4.14c

Constant λ 360 kA case

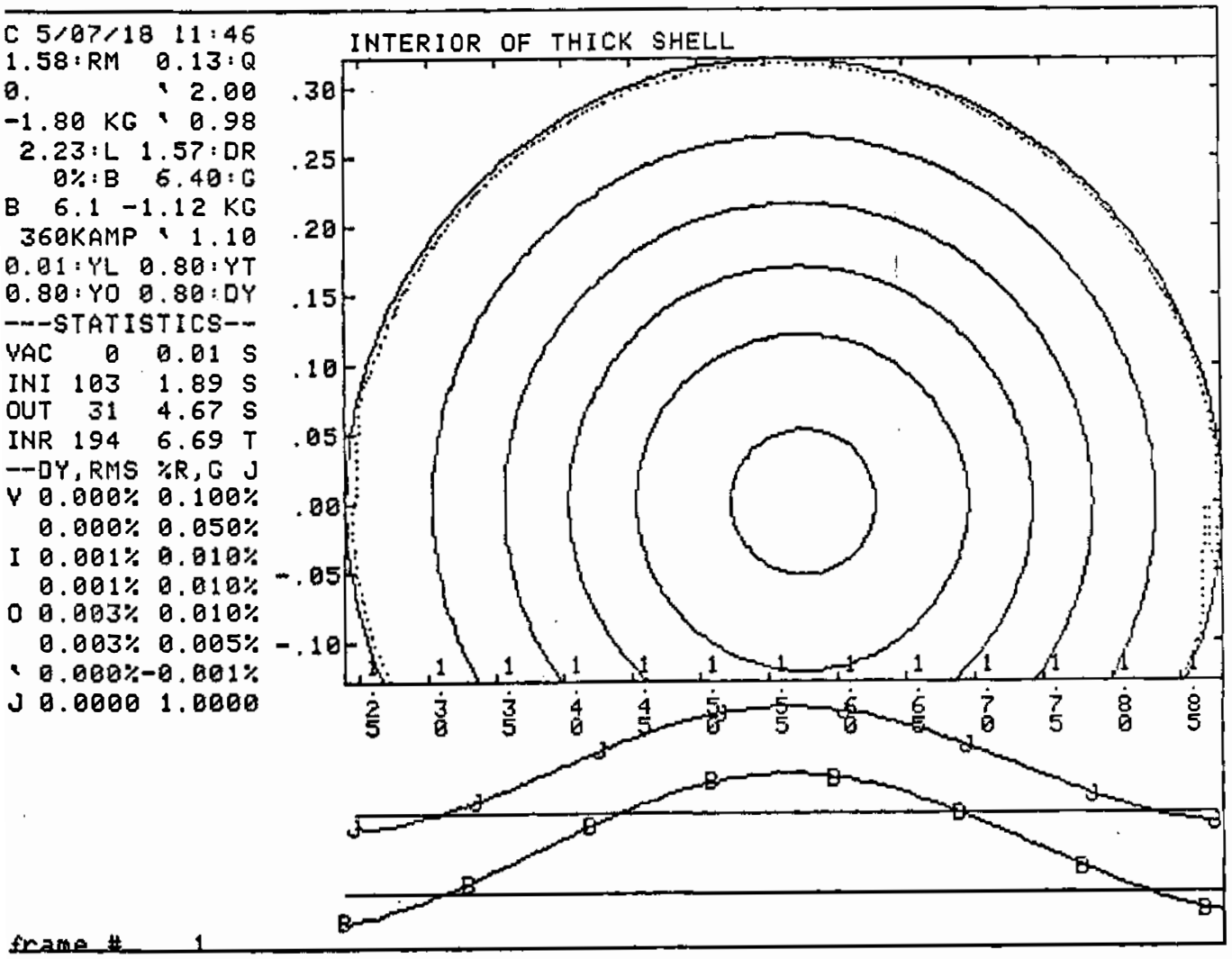

Fig. 3.4.15a

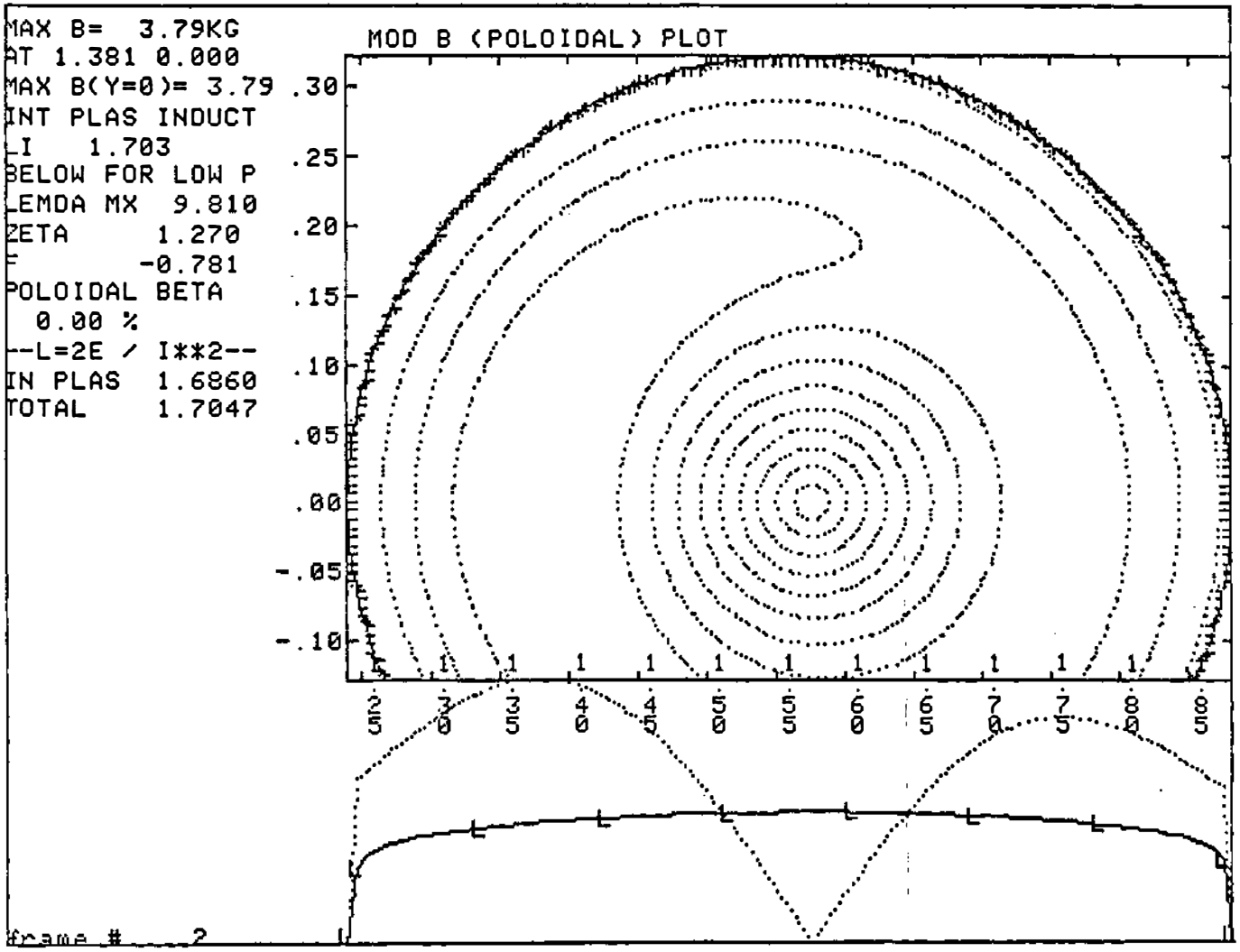
MAX B= 3.79KG
AT 1.381 0.000
MAX B(Y=0)= 3.79
INT PLAS INDUCT
_I 1.703
BELOW FOR LOW P
LEMDA MX 9.810
ZETA 1.270
F -0.781
POLOIDAL BETA
0.00 %
--L=2E / I**2--
IN PLAS 1.6860
TOTAL 1.7047
MOD B (POLOIDAL) PLOT
.30
.25
.20
.15
.10
.05
.00
-.05
-.10
frame # 2

Fig. 3.4.15b

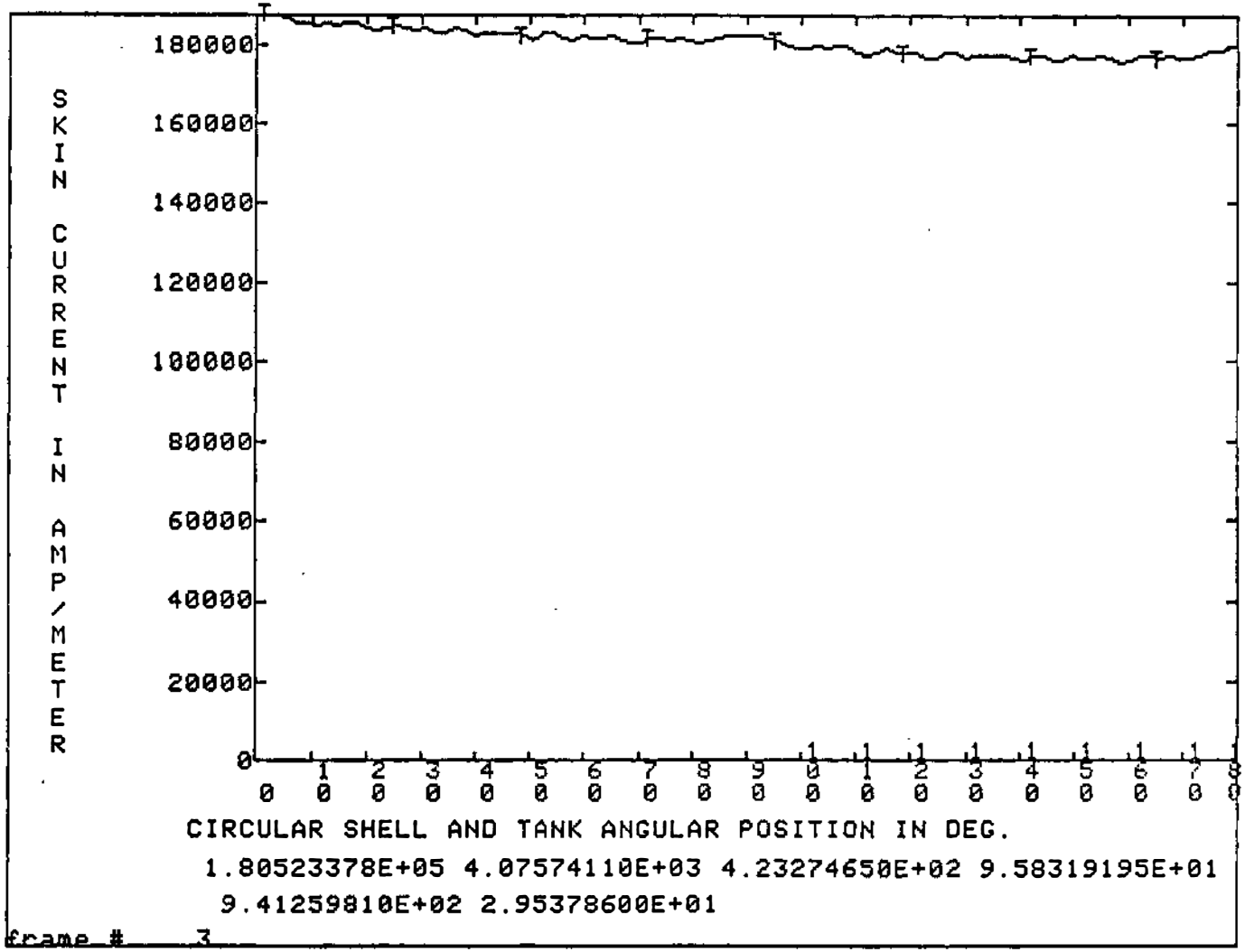
SKIN CURRENT IN AMP/METER
180000
160000
140000
120000
100000
80000
60000
40000
20000
0
0 10 20 30 40 50 60 70 80 90 100 110 120 130 140 150 160 170 180
CIRCULAR SHELL AND TANK ANGULAR POSITION IN DEG.
1.80523378E+05 4.07574110E+03 4.23274650E+02 9.58319195E+01
9.41259810E+02 2.95378600E+01
frame # 3

Fig. 3.4.15c

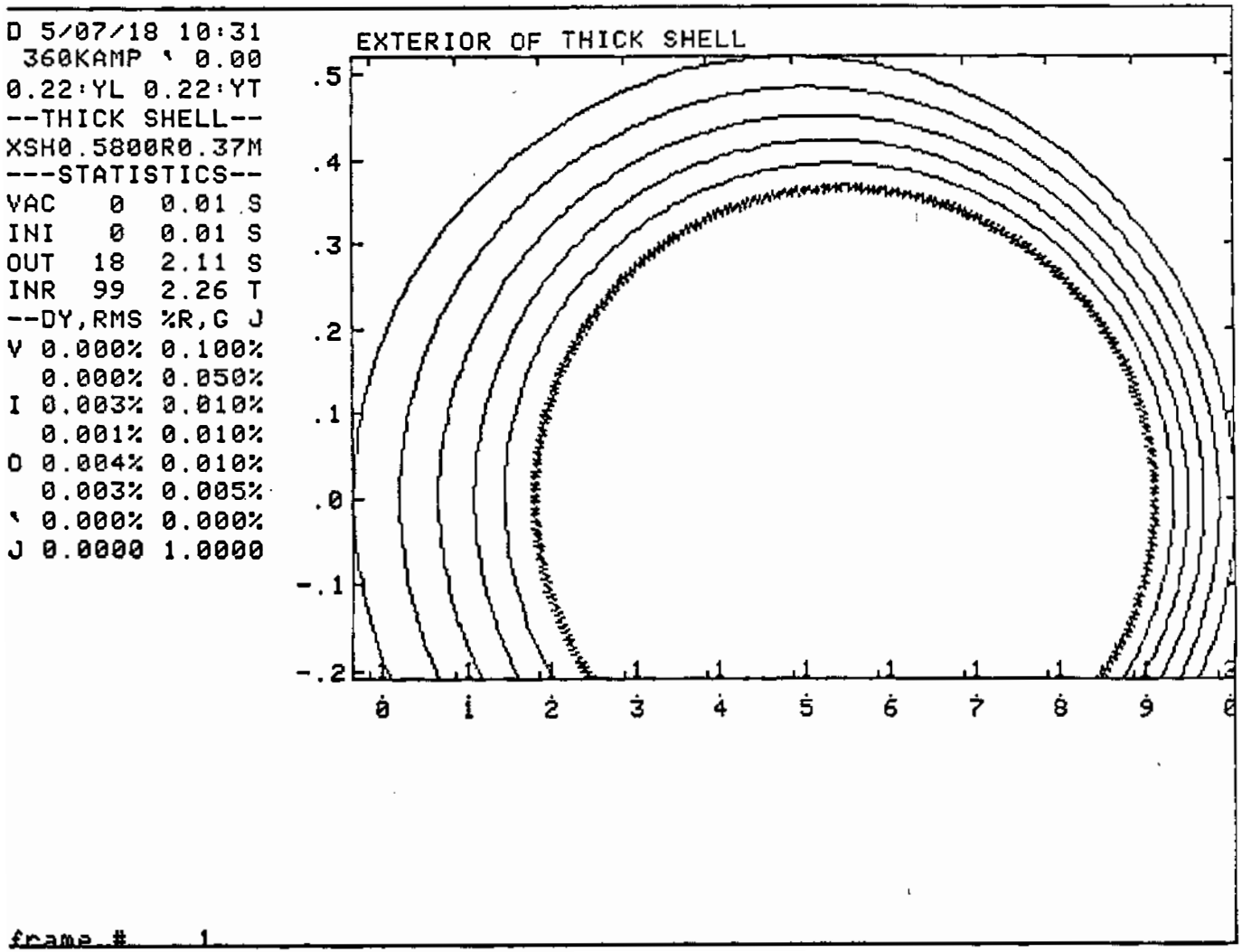
D 5/07/18 10:31
360KAMP ' 0.00
0.22:YL 0.22:YT
--THICK SHELL--
XSH0.5800R0.37M
---STATISTICS--
VAC 0 0.01 S
INI 0 0.01 S
OUT 18 2.11 S
INR 99 2.26 T
--DY,RMS %R,G J
V 0.000% 0.100%
0.000% 0.050%
I 0.003% 0.010%
0.001% 0.010%
O 0.004% 0.010%
0.003% 0.005%
' 0.000% 0.000%
J 0.0000 1.0000
EXTERIOR OF THICK SHELL
.5
.4
.3
.2
.1
.0
-.1
-.2
0 1 2 3 4 5 6 7 8 9
frame # 1

Fig. 3.4.16a

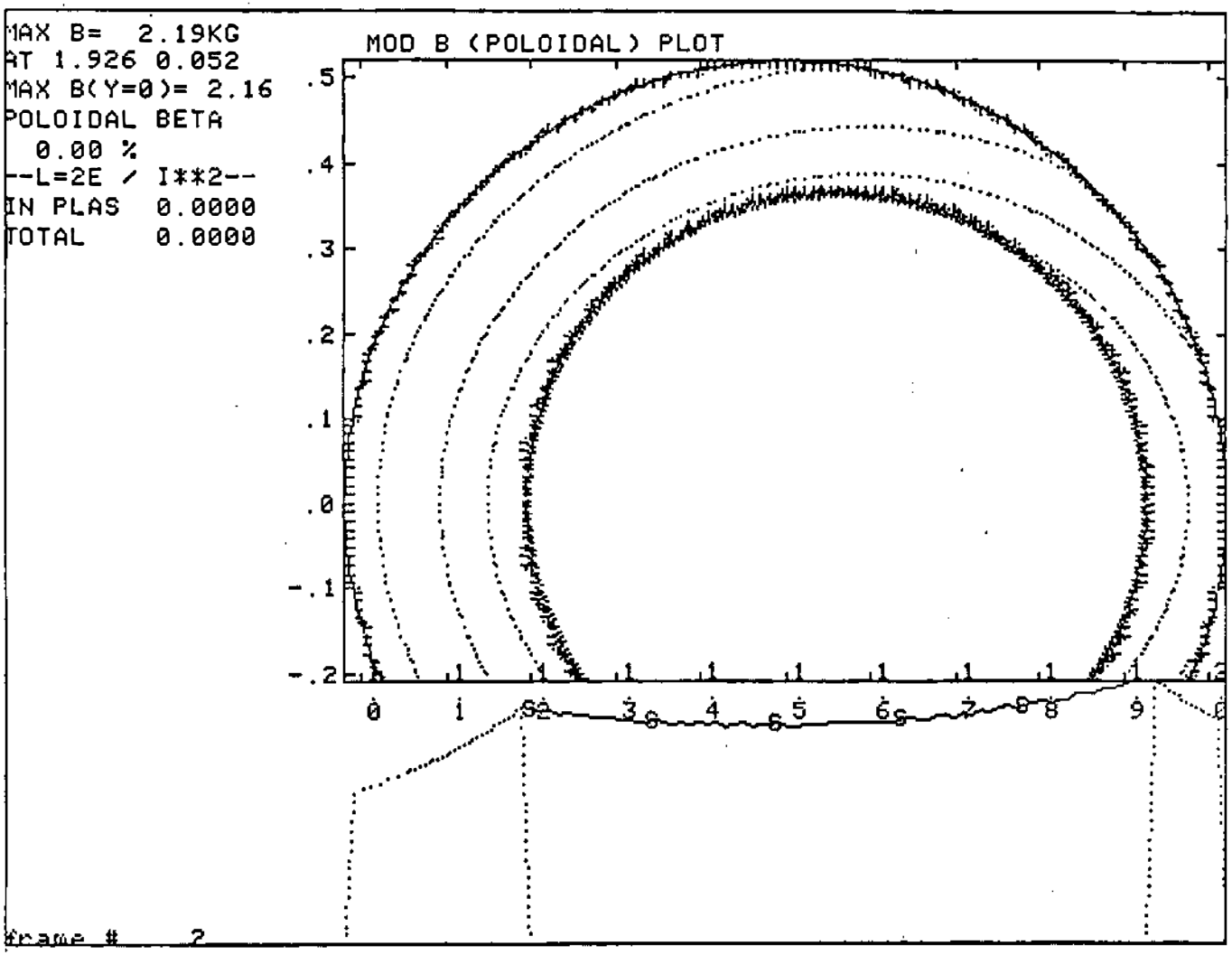
MAX B= 2.19KG
AT 1.926 0.052
MAX B(Y=0)= 2.16
POLOIDAL BETA
0.00 %
--L=2E / I**2--
IN PLAS 0.0000
TOTAL 0.0000
MOD B (POLOIDAL) PLOT
.5
.4
.3
.2
.1
.0
-.1
-.2
0
1
2
3
4
5
6
7
8
9
frame # 2

Fig. 3.4.16b

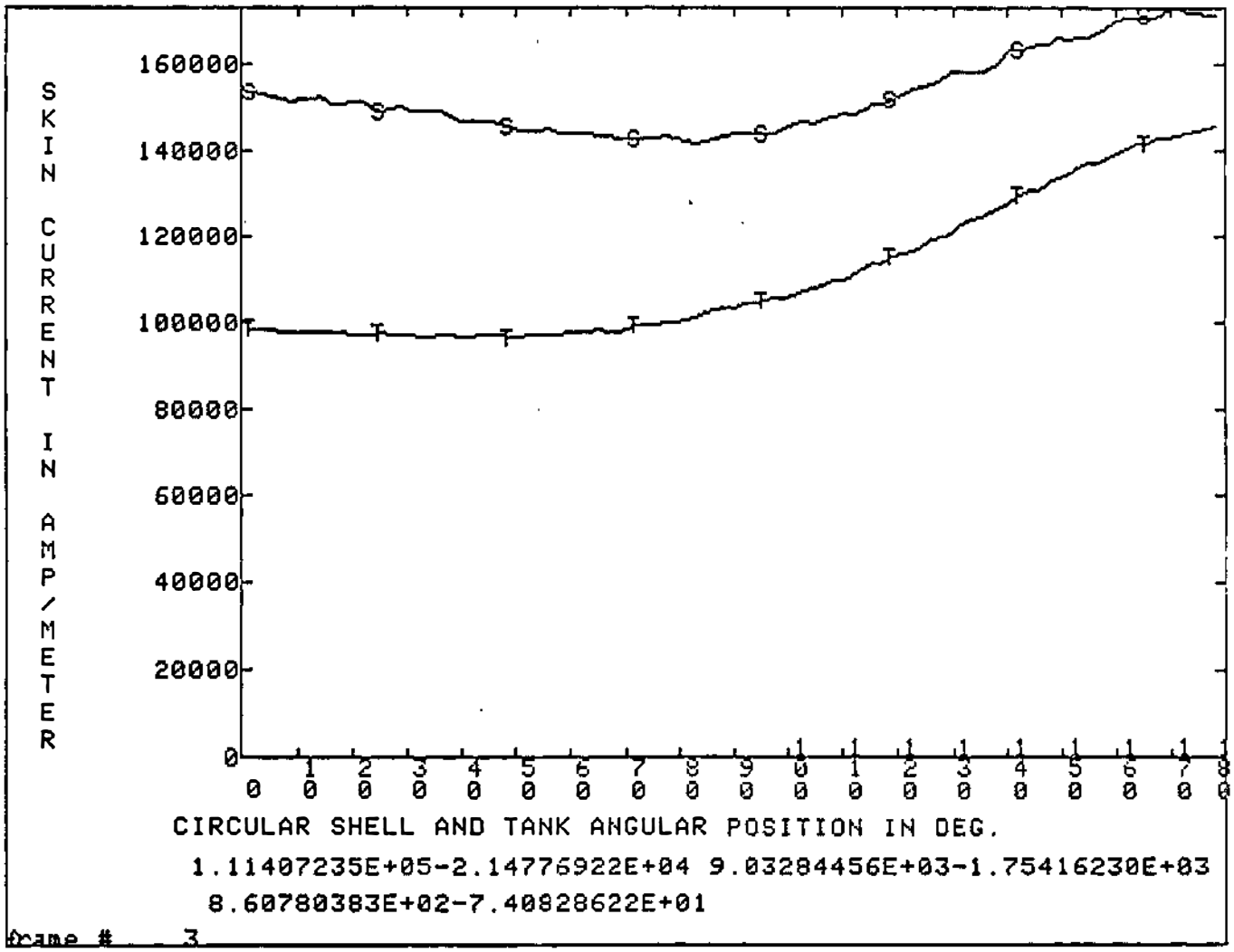
SKIN CURRENT IN AMP/METER
160000
140000
120000
100000
80000
60000
40000
20000
0
0 10 20 30 40 50 60 70 80 90 100 110 120 130 140 150 160 170 180
CIRCULAR SHELL AND TANK ANGULAR POSITION IN DEG.
1.11407235E+05-2.14776922E+04 9.03284456E+03-1.75416230E+03
8.60780383E+02-7.40828622E+01
frame # 3

Fig. 3.4.16c

current coupling will be considered separately. Dependence of inductance on θ) is found to be slightly higher than the theoretical Bessel function model, but agrees in general (see Fig. 3.4.17).

3.4.6.4 Radial Shift Due to Toroidal Effects

The plasma for the thin shelled case is found to be shifted outward in major radius by 6 cm ±2 cm. The uncertainty is due to the profile variation, plasma pressure and soak-in. Vertical field would be needed to correct this variation. Figure 3.4.18 shows the effect of soak-in, pressure, and profile on plasma radial position.

3.4.7 Vertical Field Coils

In the case of a plasma bound by a thin shell or by a limiter only, the plasma equilibrium is provided by the thick conducting vacuum tank. This thin shell is positioned to coincide with the outermost magnetic surface as predicted by the equilibrium code of Sec. 3.4.6. However, as the plasma pressure or current profiles vary, the plasma position will be expected to vary on the scale of 2 cm. Thus, a modest degree of plasma position control may be desirable. In addition, present devices such as ZT-40M indicate that a fine (but slow) control of the plasma position on the scale of a few mm can be very beneficial in decreasing plasma-wall interaction at the gap, thereby producing cleaner, higher quality discharges.

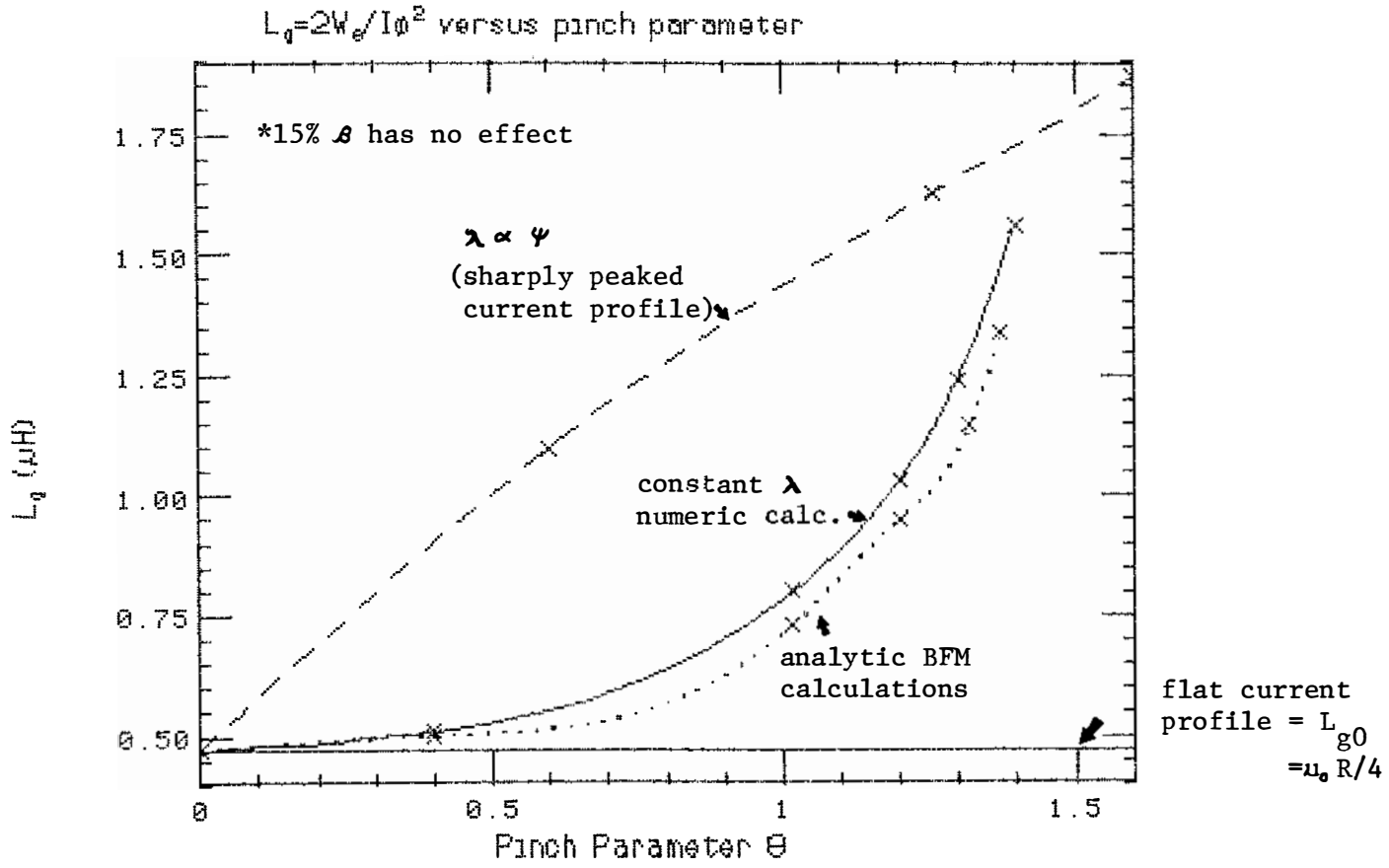
$L_g=2W_g/I\phi^2$ versus pinch parameter
*15% β has no effect
$\lambda \propto \psi$
(sharply peaked
current profile)
constant λ
numeric calc.
analytic BFM
calculations
flat current
profile = L_{g0}
$=\mu_0 R/4$
L_g (μH)
1.75
1.50
1.25
1.00
0.75
0.50
0
0.5
1
1.5
Pinch Parameter Θ

Fig. 3.4.17

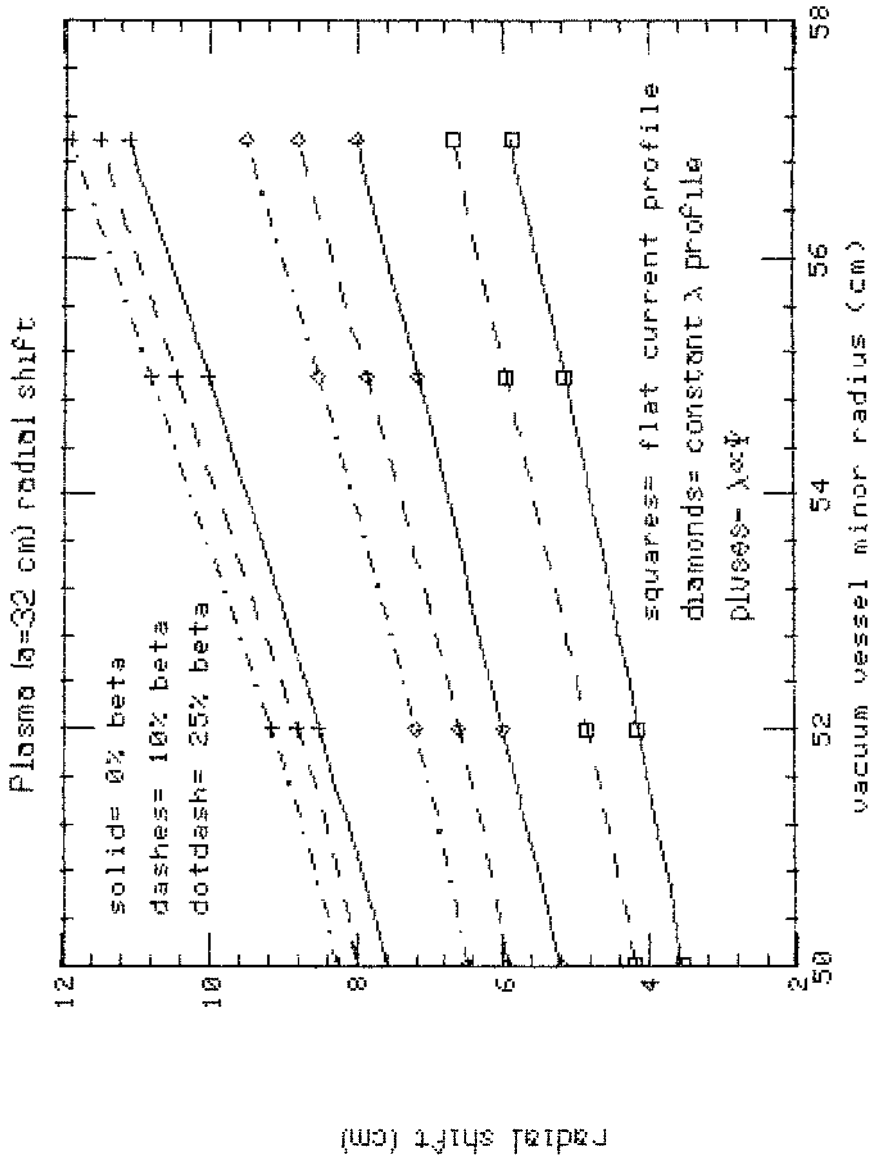
Plasma (a=32 cm) radial shift
solid= 0% beta
dashes= 10% beta
dotdash= 25% beta
squares= flat current profile
diamonds= constant λ profile
pluses= λ∝Ψ
radial shift (cm)
vacuum vessel minor radius (cm)
12
10
8
6
4
2
50
52
54
56
58

Fig. 3.4.18

We will therefore install four vertical field coils outside the vacuum tank. The field decay index, $n = -\frac{R}{B_{vert}} \frac{\partial B_{vert}}{\partial R}$, of the vertical field is $n \simeq 0$; i.e., the field is roughly straight at the location of the plasma. Thus, the applied vertical field will have a neutral effect on the stability of the plasma to axisymmetric modes. This is appropriate since the RFP plasma is extremely stable to such modes, due to its circularity and conducting boundary.

The required current in the windings is 4.6 kA-turns for each cm of plasma position control. Power will be provided, if necessary, to move the plasma over a range of several cm, either horizontally or vertically (by altering the relative current of the four coils).

3.5 Operations

3.5.1 Computer Monitor System

For tuning up the machine and monitoring gross electrical parameters such as plasma current, loop voltage, toroidal field, etc., an IBM-PC-based computer monitor system has been developed. It uses a 256K, dual disk drive IBM-PC with monochrome and enhanced color graphic display monitors and an 8087 math co-processor. A-to-D and D-to-A conversion are performed by a Data Translation DT2801-A analog/digital I/O card that fits into a single internal expansion slot in the computer. The system allows 16 channels of 12-bit analog input at a sample rate of 20 kHz (50 μsec/sample) with interrupt-driven direct memory access (DMA). Two analog output channels are available which will be used to control the gas puffing. An asynchronous communication

adapter (RS-232C) allows the IBM-PC to communicate with the main data acquisition computer (see Sec. 3.7) at a 9600 baud rate.

The software was written in a compiled BASIC that uses the math co-processor for floating point operations. The BASIC source code is about 23K bytes in length and is highly structured to facilitate modification. The software is menu-driven with defaults to allow the system to run in a routine manner without operator attention. Options provide for graphing various measured and derived quantities (such as F, θ, conductivity temperature, etc.) vs time, vs shot number at the time of peak current for the last 200 shots, or vs one another either during time for the previous shot or at the peak current for the last 200 shots. Data can be archived on floppy disks and hardcopy made of any text or graphic screen display. Most operations require only a few seconds to perform, and thus the information is available in ample time to reconfigure the machine for the next shot.

A version of the monitor system was developed during the Spring of 1985 for use on Tokapole II with the intent of transferring it ultimately to MST. The system is now fully debugged and in routine operation, and the entire system has been replicated and is ready for installation on the RFP. Figure 3.5.1 shows some sample output for a pulsed discharge cleaning shot on Tokapole II.

In principle, only five electrical quantities need be measured in order to construct all the gross plasma characteristics: 1) plasma current, 2) toroidal surface voltage at the shell (or shell poloidal

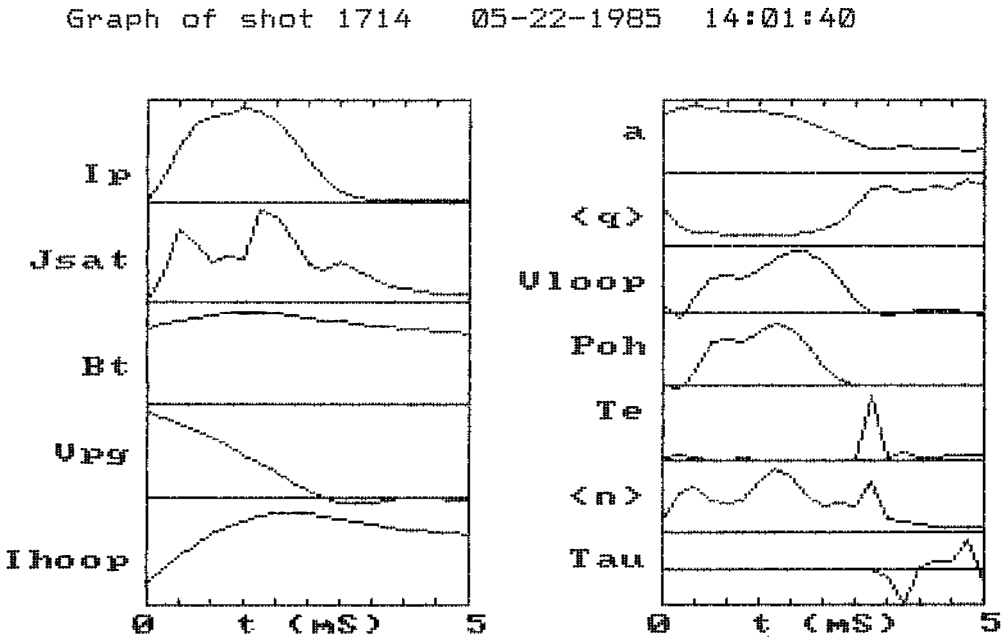

Fig. 3.5.1: Sample output of computer monitor system for pulsed discharge cleaning shot on Tokapole II.

gap voltage), 3) average toroidal magnetic flux, 4) toroidal magnetic field at the shell, and 5) plasma density. From these measurements, one can construct F, θ, ohmic input power, conductivity temperature, and energy confinement time using modeling similar to that described in Sec. 3.4.1. In practice we will monitor a variety of other voltages and currents to provide a cross-check on the modeling and to detect faults such as an arc across a shell gap which would show up as a difference in the signals detected by Rogowski loops inside and outside the shell. The monitor system will be thoroughly exercised during the construction-phase experiments where the problems are essentially the same.

3.5.2 Charging Controls and Interlocks

There will be two capacitor banks on the poloidal field system and two on the toroidal field that require independent charging control and interlocks. Except for the 30 kV startup bank, all the electrical circuitry is in place for charging, monitoring, and discharging these banks. The 30 kV bank was previously used on a neutral beam injector and will require the installation of a charging supply and circuit to control its voltage. All of these banks and their control circuitry will be tested with the Octupole vacuum chamber during the construction phase.

3.5.3 Timing Circuits

Machine recycling and other slow control functions will be handled by a rotating drum timer with 32 microswitch channels with a resolution of ~0.5%/cycle. The rotation period of the drum can be varied from 1/2 minute to 5 minutes. This controls the repetition rate of the machine. The drum rotation can be stopped at the end of a cycle for manual operation.

Fast timing for capacitor bank discharge, scope triggers, etc., is handled by 21 channels of digital timers that can be set to 1 μsec resolution over the range 1 μsec-1 sec. These timers as well as the rotating drum described above have been in routine use for many years on the Levitated Octupole.

3.5.4 Plasma Position Adjustment

The first shell that will be incorporated in the device will be sufficiently thick (5 cm) that it will produce the required vertical field for the plasma equilibrium for the duration of a 40 msec discharge. The subsequent thin shells will be placed in such a location that the vertical field produced by image currents in the vacuum vessel will keep the outermost flux surface concentric and adjacent to the shell to a good approximation. Thus we anticipate the need for small (±2 cm) radial position control only to accommodate changes in plasma current profile and beta with the thin shells. The vertical field system described in Sec. 3.4.7 will be outside the

vacuum vessel and thus will not be capable of tracking changes in the plasma position during a discharge. Rather, it will be used on a shot-to-shot basis to find an optimum dc value for each type of discharge. Plasma position will be monitored by an array of $\dot{B}$ coils of conventional design placed inside the shell.

3.6 Heat Loads, Disruptions, and Recycle Time

3.6.1 Construction Phase Experiments in VCV

For two or more years we propose to perform realistic RFP checkout experiments in the Levitated Octupole tank while MST is under construction. We particularly wish to test start-up methods, gap protection schemes, limiters, control of heat deposition, and first-wall conditioning. No increase in stored energy in capacitor banks will be used in the MST experiments, so that bank-charging recycle times will be no more than 3 minutes with the same power supplies, and heat deposition studies will be informative. Two electrically floating toroidal rail limiters have been installed in the Octupole tank. One is instrumented and capable of being inserted any variable distance up to 12 additional cm into the plasma. An insulated gap prevents flow of current, and separate current leads will permit the rail limiter to be heated for outgassing. Thermocouples will measure heat rise following plasma discharges, and provision has been made for adding POCO graphite, limiting surfaces consisting of 1" diameter rods around the entire circumference of both limiters. Initially, the tests will be made without graphite and only stainless steel will be exposed (except at the poloidal gaps where Macor

maintains the insulation). If the RFP boundary experiments in the Levitated Octupole tank are at all successful, we will be able to perform limited size-scaling studies with the movable rail limiter. Since the construction phase experiments are likely to deal with worse confinement cases than in MST we hope to see the worst features of localized energy deposition and learn to cope with them before installing the limiter and first wall of the first MST shell.

3.6.2 Experiments with Shells

All modeling calculations for the MST experiments indicate that 400 kJ will be a typical plasma energy content which must be dissipated in a single discharge. This heat removal between shots is non-trivial, even if spread uniformly on the first wall, since the innermost shell or liner is electrically and perhaps thermally isolated from the outer shell and VCV. The average temperature rise of about 25^{o}C per discharge for a 0.010 inch continuous liner would be unacceptable, so a cooling scheme must be added. Thermal conduction via heat conducting insulators or heat pipes will be provided. However, these schemes cannot solve problems arising from highly localized heat deposition on the first surface. Most RFP devices have been plagued by such localized events. Although our shells or liner do not function as vacuum containment vessels, holes produced by arcs or local erosion or melting could become a very serious problem if they resulted in intershell arcing, for example. As a consequence, our first-wall design considerations are maintaining parallel pathways, namely, planning for use of graphite armor plating or for a continuous liner

with localized limiters. Rapid progress in RFP studies with the use of graphite armor is being made; since we have about two years before a final decision must be made on these points we will have the opportunity to respond to the current state of knowledge.

3.6.3 Limiters in Shells

Two options were just described. The close interaction in these considerations of protection against gap arcing and localized heat deposition have made two realistic solutions come to our attention. A continuous liner would make it easier to keep plasma away from the voltage gaps but would require special treatment for heat dissipation and would complicate disassembly schemes. For this case we note that roughly 190 tubulation ports are used for vacuum pump-out and for diagnostic access. These tubulations can be anchored on the first wall with a localized graphite limiter which helps to prevent plasma flow into the intershell region. The limiters would probably extend 1 cm into the plasma region, restricting the minor radius to 31 cm. The regular poloidal and toroidal distribution of these limiters would provide some protection against localized energy loss and would help to dissipate the energy more uniformly around the first surface where it can be more easily removed from within the VCV. We discuss gap protection in Sec. 3.8.

The second option would provide the innermost shell with six voltage gaps protected with our most advanced designs; the protection features will extend about 2 cm into the plasma region. Around the

remaining m^2 of shell surface we would provide a full coverage of graphite armor plate in a manner not dissimilar from the present OHTE method, but of course our shell has no bellows convolutions. The innermost shell will have six segments toroidally and two full toroidal gaps; the limiter/armor plate will be attached locally to each shell segment affording a convenient method for installation.

3.7 Diagnostics and Data Acquisition

3.7.1 Data Acquisition Computer System

The demands of the boundary study pose a significant challenge to the data acquisition system. Many high-speed digitizers will be required for the observations of fluctuating magnetic fields and of the MHD activity as imaged through the soft xray observations. Further and somewhat unusual requirements arise owing to the large variety of plasma configurations which must be compared as shells are altered. The data base will be immense, and great importance is attached to data recovery since experiments with an earlier configuration cannot be repeated in practice. The standard group of diagnostics including those collected by the IBM-PC system described in Sec. 3.5.1 will be augmented on a daily basis by diagnostics specialized for the momentary research. Individual experiments will ordinarily require special arrangement of diagnostics, and individual data manipulation and display programs. An advanced data acquisition system compatible with all of these properties has been developed, and most portions are in use. The menu-driven system called DAS allows unsophisticated users to

setup arbitrary numbers of digitizers, provide full descriptive and quantitative information on each diagnostic channel, display raw or processed data as desired, store all raw and processed data as desired, and prepare these specialized programs with great speed and simplicity. A further feature is that the data and descriptive information are put in a format compatible with commercial DATABASE retrieval methods, such as the DEC-supported DATATRIEVE. Along with descriptive and data files for each shot there is the so-called super-index file which we have developed for convenient retrieval purposes. Portions of this file which contains keywords and parameters for quantitative search purposes are also utilized for a printed shotlog which is fully descriptive of the experiment in progress.

In order to accomplish such a powerful system with a very modest CPU requires that very little complicated data processing take place between plasma discharges. (A PDP 11/24 has been used for full test and operation of this DACS system.) In practice, most data manipulation is performed using the computer system at PSL; a major upgrade is being installed with the commercial Ethernet interconnection and a high-speed optical link to PSL. The PSL system is being further upgraded with optical data storage of immense capacity such that DATABASE methods will become available to us despite the limited features of the PDP 11/73 CPU which will probably form the heart of our local system. This system will serve several CAMAC crates, utilizing a large sealed disk for temporary data storage, magnetic tapes for storage of unevaluated data, and bulk archival store of evaluated data and the files used for data retrieval purposes.

3.7.2 Diagnostics

We distinguish several classes of diagnostics: (1) Diagnostics for machine operation with a stand-alone microcomputer incorporating modeling as discussed in Sec. 3.5.1. (2) Diagnostics for routine monitoring of impurities with a stand-alone microcomputer as discussed in Sec. 3.9.8. (3) Group-supported diagnostics, and (4) Special diagnostics. These will vary from day-to-day depending on the momentary needs and will be accommodated in the DACS to any reasonable demand but need no further discussion. The software development has been dominated by the desire to make addition of diagnostic channels so simple that significant alterations between shots may be easily accomplished. This goal has been met.

Group-supported standard diagnostics will be discussed here. Most of these are existing, and can be transferred intact from the Levitated Octupole. They are summarized in Table 3.7.2.1. Owing to the special problems associated with nested shells, installation of several diagnostics which utilize electrical connections to sensors at and between shells is not straightforward and will be discussed elsewhere. The major diagnostic now under development is a near-replica of the Thomson scattering unit used by Professor Navratil of Columbia University who has been generous with his advice (Levinton and Navratil, Rev.Sci.Instrum. 54, 35 (1983)). A measurement of T_e at a single time and plasma radius is intended at the first level, but enough radial ports will be provided, however, to permit a 7-point radial temperature profile. The detector selected (a 10x10 intensified

Table 3.7.2.1

Standard and Optional Diagnostics Channels for Primary DACS

DIAGNOSTIC	STATUS	CHANNELS
Thomson Scattering	Parts on order	5
Charge Exchange Analyzer	Functional	2
K-Band Interferometer	Functional	1
F,θ Flux Loops, Rogowski Loop	Under Design	3
Edge Langmuir Probe	Under Test	2
Permanent SXR Array	Prototype on Tokapole II	16
Permanent $\dot{B}$ Arrays	Under Design	20
VUV Monochromator	Functional	1
SXR Monochromator	Functional	1
Visible Monochromator	Functional	1
Visible Bremsstrahlung	Functional	1
H-Alpha Monitor	Functional	2
OPTIONAL DIAGNOSTICS		25 Total
Permanent SXR Array Channels	Prototype on Tokapole II	13
Permanent $\dot{B}$ Array	Under Design	40
Visible Light Fluctuation Array	Functional	16
Impurity Line Monitors	Functional	5
CO_2 Laser Scattering	GA Proposal	2
Operations Diagnostics	Prototypes on Octupole RFP	Arbitrary
Radiated Power Bolometer	Functional	1
Thermocouple Arrays	Prototypes on Octupole RFP	Arbitrary

multianode array) would permit development into a multi-point system at a later date. This system will be implemented and tested in construction-phase experiments; the laser and detector have long been ordered and will soon arrive. The difficulty of implementing a reliable T_e measurement is well known, and we are grateful for the assistance which we are receiving from several groups who successfully use Thomson scattering.

Fluctuating magnetic field measurements will be at the heart of the RFP boundary condition studies, and we intend to install several arrays of coils. Many of our present studies depend heavily on the comparison of B-dot and soft xray measurements, but the very large arrays common to RFP studies will be a new development for us. Printed circuit techniques have been used for these arrays at Los Alamos, GA Technologies, and on HBTX-1A, and we have obtained much advice and useful information from all of these groups. Arrays will be installed between shells, on the VCV, and inside the inner shell, but at any given time not all will provide signals which we will acquire. Our initial plans call for approximately 40 fluctuating B measurements, and approximately 34 soft xray signals from overlapping arrays. On Tokapole II we presently have two 17-channel and one 7-channel soft xray arrays, and this is a familiar technique in the group. However, we have little experience with advanced correlation methods, nor with advanced inversion methods, and have a lot to learn on the full exploitation of such large arrays. Several graduate students are now becoming familiar with such manipulations with multi-coil arrays using signals from Tokapole II plasmas.

We responded to review committee comments and submitted a modified cost proposal which permitted a DACS development in keeping with the ambitious goals of the boundary condition study. The number of CAMAC crates and modules to be installed is not yet clear since we are presently evaluating the performance of a particular 8-channel digitizer. However, the number of channels comparable to the LeCroy Model 8210 should be approximately 80 at the time when the boundary condition studies commence. The software development uses this number as a lower limit.

3.8 Voltage-Gap Protection Issues

3.8.1 Gaps in Vacuum Containment Vessel

Present designs call for the gaps in the VCV to be protected with a version of the advanced design gap protection presently being tested in the construction-phase experiments.

3.8.2 Gaps in the Shells

Gaps in the outer shell can be protected with a simple insulator as shown in figure 2.2.7.2.1. Transient pressure simulation has shown that the pressure in the space between the shell system and the VCV does not rise dangerously during the period of large gap voltages (see Sec. 3.9). Some ionized gas may stream through the port hole tubulations however, and in combination with any electron cyclotron resonance zones cause problems. This problem can be reduced through the placement of limiting baffles in the VCV shell system space. Use

of titanium gettering in that space would also reduce the pressure rise, but gap insulators would then have to be protected from sublimated titanium with shadow baffles.

Gaps in the inner shell can also be protected with a simple insulator if the continous liner option is chosen. If the continous liner is not used, the gap design will probably be a modification of the advanced design being tested in the construction phase experiments. A combination of graphite armor incorporated in the parts of the gap protector nearest the plasma, limiters to reduce plasma density in the region of the gaps, and a multiple gap design to reduce gap voltage could result in satisfactory performance.

Transient voltages on sudden termination of the plasma discharge must be carefully considered. Even with a continuous liner, the loop voltage can be as high as 5600 volts. Each poloidal gap would then see a voltage of ~900 volts. Without a continuous liner acting to dissipate the energy in the poloidal flux between the plasma and the wall (~80 kJ with a 400 kA discharge) these voltages could be much higher. Solutions in a linerless configuration include elements across the outer shell circuit poloidal gaps. These could be arrays of resistors, spark gaps, or thyrites.

3.8.3 Shell/Liner Protection During Faults

During a sudden interruption of the discharge current the full plasma energy of typically 20 kJ could be deposited in a small area of the shell or liner. Prevention of damage due to this localized energy deposition will probably require some formal limiter or armor. Graphite rings 10 cm in diameter and 1 cm in average thickness around each porthole tubulation could individually absorb the full plasma energy with ΔT of $\sim 200^{o}C$. The normal operation of such limiters would only result in ΔT of $\sim 25^{o}C$/shot.

3.8.4 Discharges Between Shells and VCV

As previously discussed the space between the shell system and the VCV remains at fairly low pressure during the high voltage period of the plasma pulse. Previously discussed protection against the production of plasma in this region in combination with an electrostatic grounding system should reduce the probability of shell VCV arcs. Good practice dictates that the insulator in the trestle legs have a broken surface.

3.8.5 Diagnostic Protection

Diagnostics mounted on the shell system, or protruding through the porthole tubulations will either have to be well insulated from the shell system or have all their wiring brought through the vacuum wall electrically isolated from the MST. Cabling of this wiring through the

vacuum will have to be carefully done to avoid arcs. Consideration of transient voltages on sudden termination of the discharge will require diagnostics to be insulated to >6 kV.

3.8.6 Preliminary Gap Tests in Tokapole II and the Octupole Tank

A program of gap design testing has been underway using the Tokapole II device (see Fig. 3.8.6.1). The poloidal gap on the Tokapole II has been tested up to voltages equal to the six segment shell gap voltages. A special-gap simulating apparatus has also been constructed and used in the Tokapole II device. Present experiments involve simulating the advanced gap design which is being installed in the construction-phase experiment. Results so far are inconclusive in the presence of plasma, but the experiment has shown very encouraging results with neutral gas. Special instrumentation has been installed around the Tokapole II poloidal gap to explore actual plasma conditions near a gap (see Fig. 3.8.6.2). Attempts will be made to operate the gap-simulation apparatus under these conditions. A problem exists in that the gap simulation apparatus tends to behave like a large Langmuir probe, placing huge current demands on the biasing capacitor bank. Preliminary results from instrumentation near the real poloidal gap shows no such behavior. The next stage in our testing program calls for simulating actual plasma conditions near the real gap in the vicinity of the gap simulator and driving the gap simulator directly from the poloidal field core. Additionally, some obvious insulation problems in the gap simulator are being cured. These problems would

Experimental Apparatus:

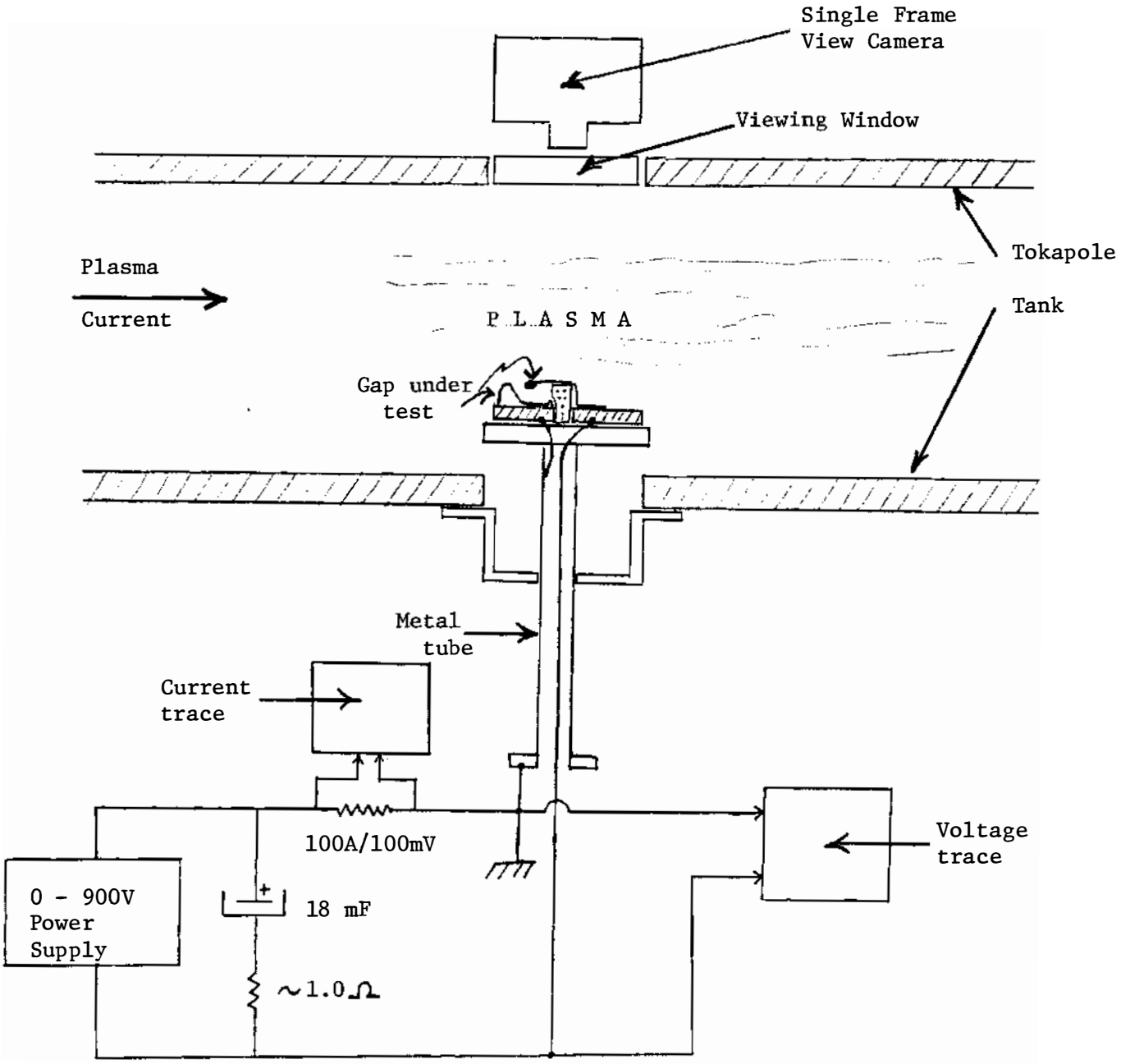

Fig. 3.8.6.1
Gap Simulation Experiment

Experimental Apparatus:

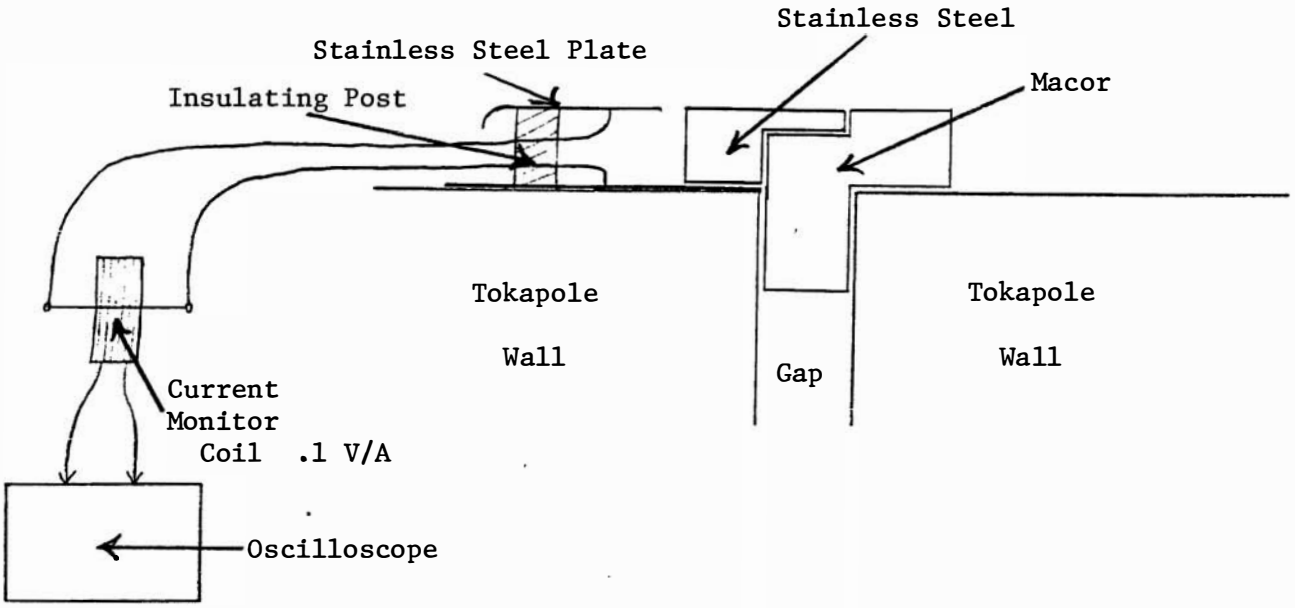

Typical Oscilloscope Trace:

Shot taken during standard Tokapole II discharge

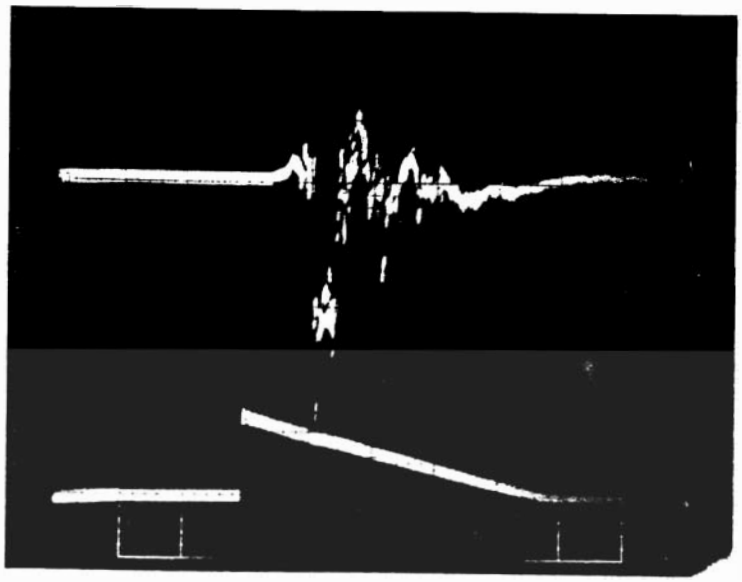

- 5 Amps - Collector Plate Current

- 50 Volts - Tokapole Gap Voltage

.5 ms/Div

Fig. 3.8.6.2
Gap Current Experiment
on Tokapole II Gap

not be encountered in an actual gap but are interfering with obtaining clear results from the simulation apparatus.

The advanced gap protection design being installed in the construction phase experiment is shown in figure 3.8.6.3. It is based on several hypotheses:

1) If the electric field near the plasma were principally perpendicular to the magnetic field some gain due to magnetic insulation might be obtained.
2) The materials of the gap protector nearest the plasma should have high melting points, low sputtering coefficients, and low coefficients of secondary electron production. These criteria would help prevent a catastrophic arc due to damage from corona like discharges or plasma bombardment.
3) Insulating materials should be shielded from plasma bombardment or titanium sublimation to prevent damage, carbonization, or local pressure rises.
4) Insulating materials should have broken surfaces.
5) The Paschen curve may be used to determine break-down voltages at least for neutral gas and no magnetic field. Since the protector will be operating on the low pd side of the breakdown minimum, the most likely place for a discharge will have the largest pd.
6) The areas most likely to break down should be near the outside of the gap protector to avoid pressure rises in the gap protector and to limit any damage to insulating materials.

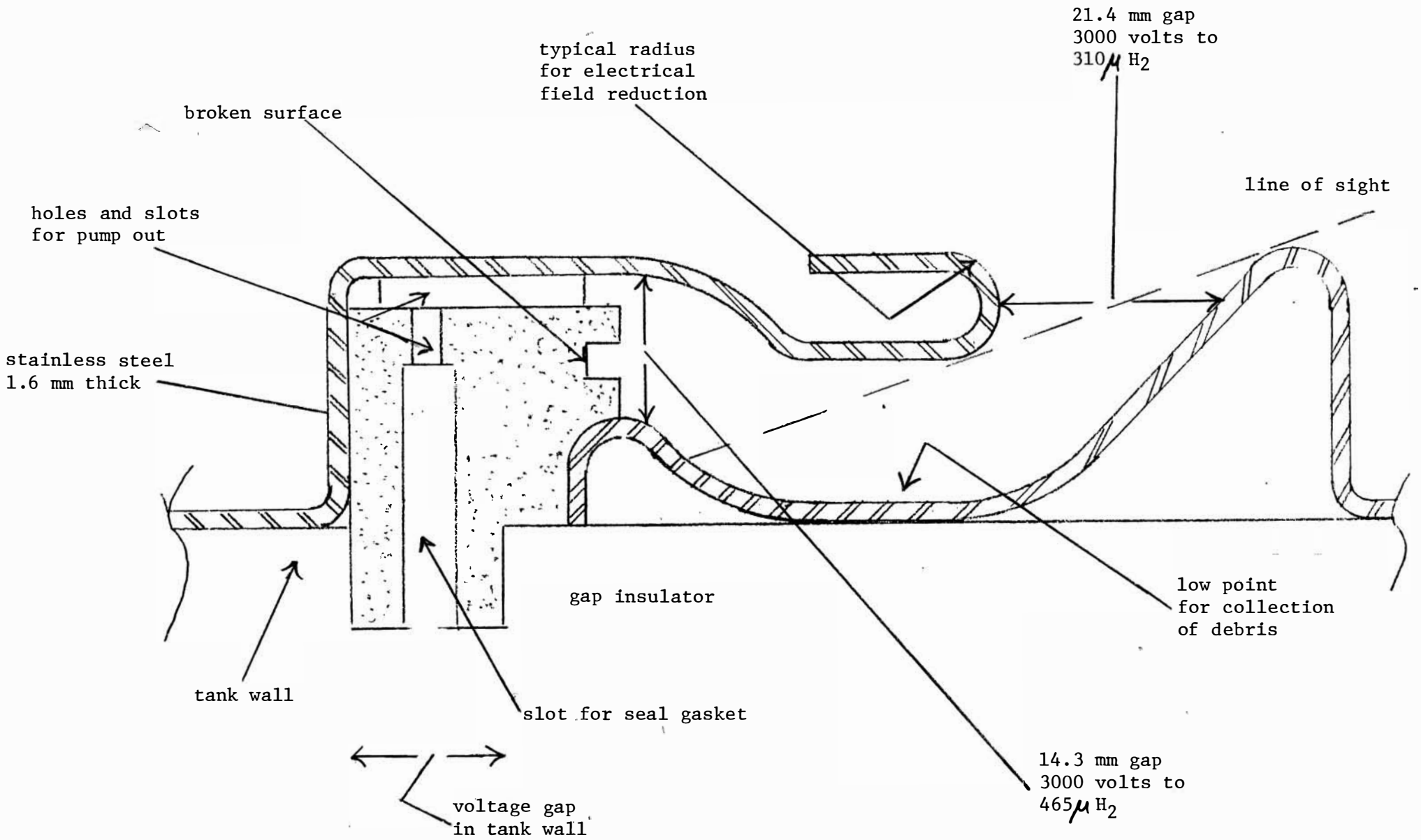

Fig. 3.8.6.3:
cross section:
advanced gap protector
for construction
phase experiments

7) Good practice should be used to reduce large local electric fields due to sharp edges.
8) Good vacuum conductance should be provided to all parts of the gap protector so that the lowest possible gas pressures will be present.
9) Low areas that would trap machine trash such as titanium flakes must be avoided or placed in harmless positions. Such trash could initiate a discharge.

The design shown is calculated to be able to withstand 1kV at hydrogen pressures up to 0.31 Torr in the absence of plasma. This includes a 3X safety factor for electric field concentration. Arcs induced in a similar design on the gap simulator indeed appeared to occur in the outer region of the protector, and damage was very limited.

3.9 Vacuum, Conditioning, and Fueling

3.9.1 Vacuum Requirements

3.9.2 Pumping Stations

Three turbomolecular pumping modules will be assembled for MST removal pumping. Each module is to be complete in itself with individual roughing pump and vacuum monitoring and is to have an interlocked, hydraulically operated valve. These modules are intended to be fully operational in time for transportation to PSL and use in vacuum acceptance tests. Owing to the raised elevation of MST there will be adequate space for an efficient vertical stacking of the module components. We are accustomed to the use of titanium slug getters to

maintain high base vacuum in the Levitated Octupole and Tokapole II. The MST vacuum vessel design incorporates getter ports compatible with our motor-driven getter unit design; however, we intend to install but not necessarily use titanium gettering in original MST experiments. Owing to our unconventional proposal to confine the plasma within the shells it may be desirable to provide this very high pumping speed to maintain low pressures in the VCV while adding gas within the shells. No line-of-sight path will be available for titanium to enter the shells from the heated getters.

3.9.3 Vacuum Interlocking

Vacuum monitoring will be provided at the VCV, at each of the pumping modules, and in each of the separate diagnostic beam lines. Each separate pumping station will be interlocked to close hydraulically operated valves. The master vacuum sensor in the VCV will close all hydraulic valves, and the local sensors will shut down turbomolecular or ion pumps depending on the vacuum within the pumping station. In present usage, diagnostics with filaments, such as the RGA or fast ion-gauge, are interlocked with the master ion gauge.

3.9.4 Roughing Lines

Each pumping station will be provided with its own roughing or backing pump. A separate pump will be utilized to provide an electrically insulated roughing line which will be available at all toroidal angles for rough pumping each probe port and for pumping between the double o-rings which will be required at each insertable probe. In addition, it is probable that after an up-to-air the VCV

will be roughed out through a trapped, high-speed roughing line, rather than through the turbomolecular pumps.

3.9.5 Discharge Cleaning

It is expected that the RFP performance will depend significantly on the cleanliness of the first-wall owing to the effect of impurities on resistivity and their effect on power balance through their radiation. As commonly used on Tokapole II and all other tokamaks both pulsed and glow discharge cleaning methods are utilized for wall conditioning. Provision is made for high-repetition rate pulsed discharge cleaning in our plans for the VCV and, later, shell clean-up. Glow discharge cleaning within the shells will also be incorporated, requiring an insertable electrode and careful gas control. Optimum settings of voltages and gas pressure have been facilitated through monitoring of the impurity evolution using the standard diagnostics described in Sec. 3.9.8.

3.9.6 Provision for Baking of Limiters and Walls

No provision will be made initially for baking limiters and walls in situ, but, as discussed elsewhere, there will be a natural temperature rise of the thermally isolated shell walls during normal discharges. Only high-temperature insulators will be incorporated into the shell, limiter, and supporting trestles, and limited baking could be incorporated since all vacuum seals are well isolated at the VCV walls. Preliminary studies on baking limiters will be performed in the construction-phase experiments in the Levitated Octupole tank as discussed in Sec. 3.6.1.

3.9.7 Fueling Considerations

Existing RFP's run in the range of 1-10 mtorr hydrogen fill pressure. In MST, the fill pressure will be controlled by means of three Veeco PV-10 piezoelectric valves distributed around the torus with existing programmable waveform power supplies. However, to reduce the risk of electrical breakdown of the insulated gaps in the vacuum vessel and shell, gas will be puffed into the region inside the liner just before the application of the ohmic heating pulse in order to maintain a low pressure in the region between the liner and vacuum vessel. The region inside the liner has a volume of 3.15 m^3 and thus can be filled to 3 mtorr in 7 msec with a puff rate of 1,500 torr-l/sec with the valves backed by 1520 torr of gas (see Fig. 3.9.7.1 and 3.9.7.2).

Most RFP's rely on wall recycling to replenish the plasma lost to the walls. In MST, the recycling will be supplemented by programmed gas puffing if required. In the worst case, with no recycling, and a particle confinement time of 2 msec, a puff rate of ~750 torr-l/sec would suffice to maintain a volume-averaged density of 3×10^{13} cm^{-3}, and thus we would have a factor of two margin on our gas puffing capability. The piezoelectric valves have a response time of ~1-2 msec, and so it will be possible to feedback control the puff rate to maintain a constant density, if desired, such as is presently done on Tokapole II.

In order to get the required 500 torr-l/sec flow rate per valve, the standard valves are modified by machining and continuing their orifice, adjusting their spring tension, and applying up to 200 pulsed

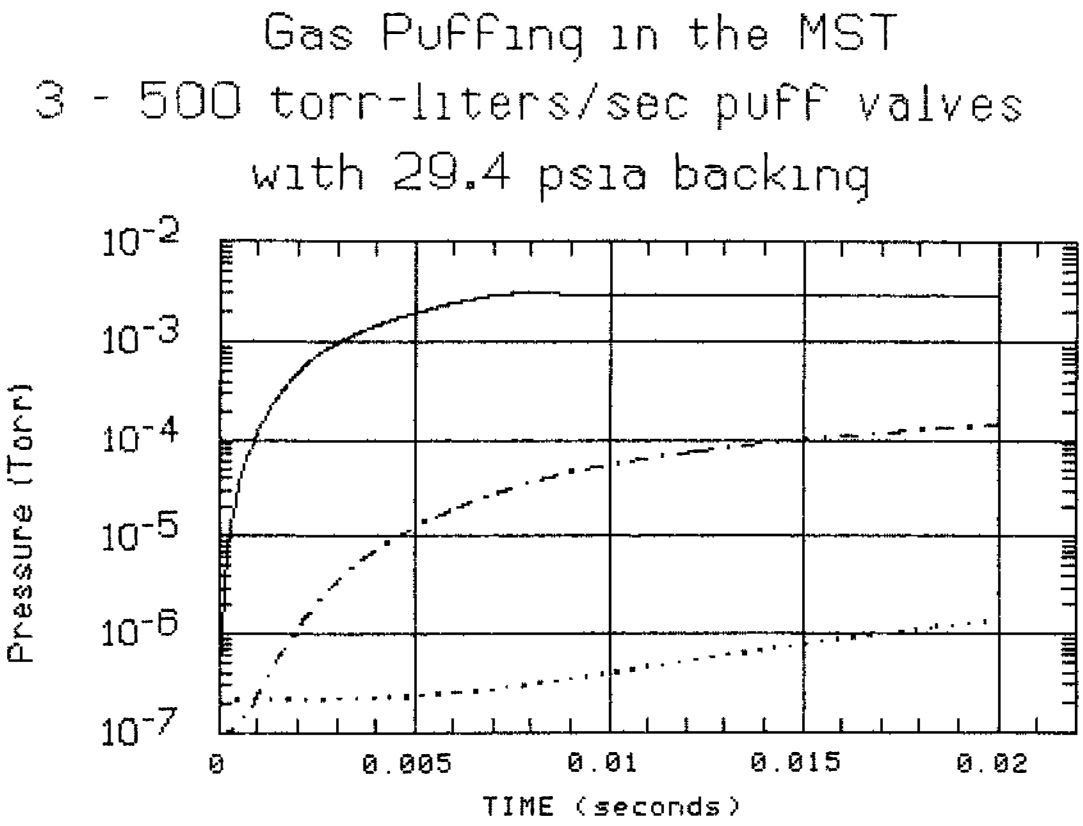

Fig. 3.9.7.1: Pressure rise at various places within the VCV during gas puffing.

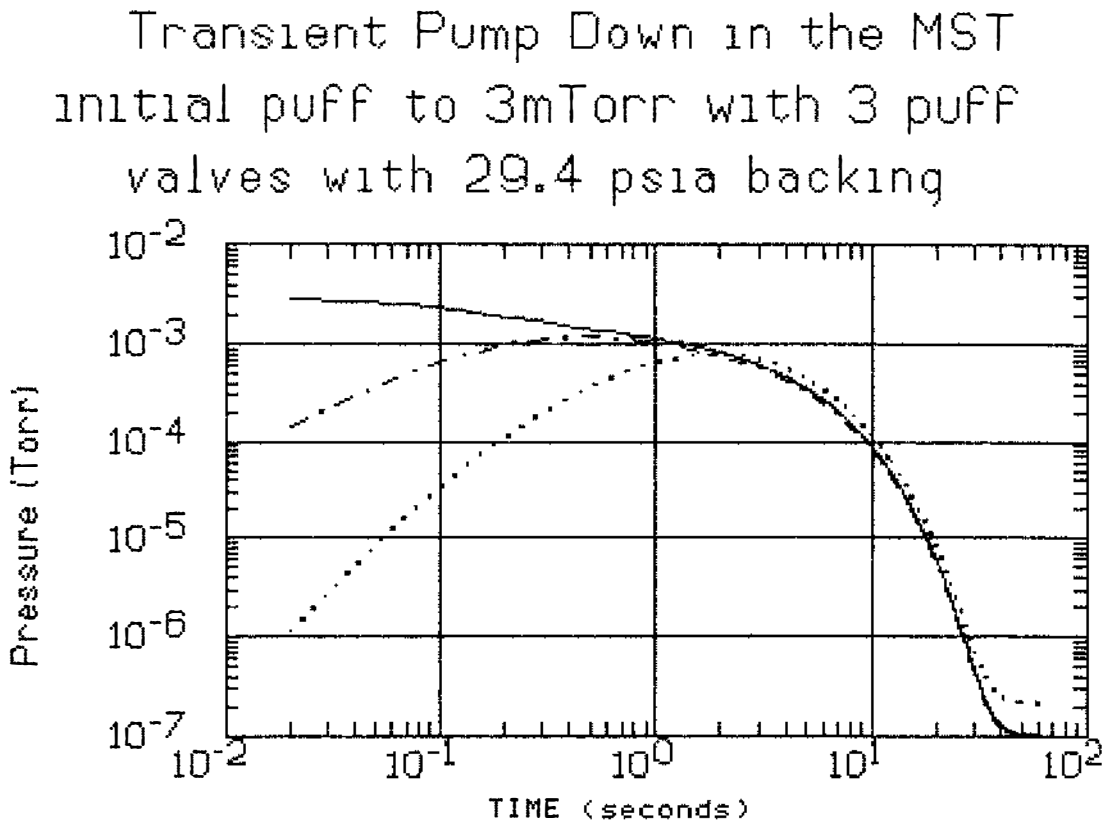

Fig. 3.9.7.2: Pumpdown at various places within the VCV after gas puffing.

volts with a pressure of 80 psig. These techniques have been used routinely for many years on Tokapole II and the Levitated Octupole.

3.9.8 Impurity Monitoring and Control; Spectroscopy and RGA

In support of wall conditioning and impurity control, several schemes for monitoring will be utilized. All are traditional in our program. Radiation by major impurities is monitored using photomultiplier/interference filter combinations selected for important transitions in the near UV and visible. Output vs. time is acquired for several channels (16 available) with a stand-alone microcomputer which records and prints the time variations and integrated signals. The signals are also commonly recorded by the major DACS. The instrumentation is available from the Octupole program as is a residual gas analyzer (RGA) which is especially useful for monitoring the water vapor in the machine. Water being the usual source of oxygen, the major impurity, can be controlled to some degree by plasma cleaning and bake-out methods. Routine monitoring and archiving of impurity signals is helpful in assessing progress. Impurity control methods are notoriously complex, and we will continue to be guided by progress in the field.

APPENDIX I

WORK STATEMENT

The grantee shall initiate a program to study the boundary condition required to operate a reversed field pinch. The program in the first year shall include:

- o Operation of magnetic limiter experiment with existing rings.
- o Experimental test of vacuum gap designs in the presence of plasmas, and presentation of results at the design review.
- o Completion of a design of a plasma discharge chamber of circular cross section according to the concept included in the addendum to the proposal.
- o Presentation of the completed design to an OFE sponsored design review team. Final design to be submitted to OFE for approval before fabrication begins.
- o Initiation of fabrication of new discharge chamber.
- o Modifications of the existing octupole experimental facility in order to achieve an RFP without divertor rings.

The program in the second year shall include:

- o Modifications of the octupole experimental facility to conduct magnetic limiter experiments with new divertor rings if the need for such modifications is determined from first year results.
- o Installation of Thomson scattering diagnostic on magnetic limiter experiment.
- o Operation of RFP with magnetic limiter boundary.

The program in the third year shall include:

- o Completion of the circular cross section discharge chamber.
- o Completion of installation of circular cross section discharge chamber.
- o RFP operation without liner at full 52 cm radius.
- o Initiate fabrication of 5 cm thick conducting shell.

Grantee will prepare an administrative plan related to the fabrication of circular discharge chamber.

APPENDIX II

MST PROJECT MILESTONES

Schedule Baseline and MST Fabrication Milestones

Job	Milestone	Original	Latest-Revision	Completion
ME-600	Vacuum Vessel RFQ Submission			6/85
	Internal Review of RFQ Alternatives			
PR-600	Completion of Management Plan*	9/85	8/85	
PR-601	Engineering Design Review*	9/85	8/85	
OF-500	Movable Limiter Installation	8/85		
PS-400	Operations Computer Installation	8/85		
	Begin Non-Circular RFP Experiments*	10/85		
SP-100	Survey and Layout in High Bay	10/85		
MA-100	New BT Core Design	10/85		
ME-200	Contracts Let for Fabrication*	10/85		
MA-110	Design Optimized Divertor Rings	12/85		
DA-400	Install New DACS	2/86		
SA-600	Complete Plan for System Safety	2/86		
DG-400	Complete Plan for Diagnostic Set	3/86		
ME-300	Begin Building Optimized Divertor Rings	3/86		
ME-110	Design Core-Keeper Hoist	3/86		
SP-110	Design False Floor and Second Deck	3/86		
OF-510	Install Rings*	6/86		
OF-610	Report on RFP plasmas without rings*	6/86		
	Commence Experiments with Rings*	8/86		
DG-500	Install Thomson Scattering Diagnostic*	9/86		
VA-400	Vacuum Module Completion	12/86		
ME-400	Delivery of MST Assembly at PSL			
ME-410	Acceptance of MST Assembly			
ME-310	Finish Machining of Pump and Portholes			
VA-410	MST Vacuum Checkout and Acceptance			
ME-500	Gap Protection Installation			
ME-510	Limiter Installation			
SP-600	Empty High Bay*	4/87		
OF-620	Report on magnetic limiter studies*	4/87		
ME-520	Install Core-Keeper Hoist			
PS-500	Operating Controls Installed			
SP-610	Final Placement of Iron Core			
MA-500	New BT Core Installation			
ME-530	Delivery and Installation of MST			
DA-600	Complete Stage-II of DACS			
PS-510	Transmission Lines Installed			
VA-600	Complete Leak Check			
PS-600	Electrical Tests of Toroidal, Poloidal, and Vertical Field Systems			
ME-120	Initiate Shell and Trestle Final Design			
SA-610	Final Safety Checkout			
PS-610	First Plasma*	10/87		
ME-130	Submit RFQ for First Shell Configuration			
ME-320	Complete First Shell Configuration*	11/87		
DG-310	Complete Fabrication of Shell Diagnostics	11/87		
ME-420	Delivery and Acceptance of First Shell			
ME-540	Install Shell, Shell Diagnostics, and Liner in Vacuum Vessel			
SA-620	Final Safety Checkout			
PS-620	First Plasma			

* Level-1 Milestone

APPENDIX III

TREATMENT OF PERTURBATIONS DUE TO WINDINGS, IRON, AND POLOIDAL AND TOROIDAL GAPS

A. General Consideration

A plasma carrying a toroidal current can be imagined to be ideally maintained in position by a closed superconducting toroidal boundary. The outer poloidal flux surface coincides with the conducting boundary, and current column motion toward the wall increases the image or boundary current density and forces the plasma back, or we can say that an equivalent vertical field is generated which repositions the plasma. Without a conducting boundary numerous "primary" (or so-called ohmic heating) toroidal wires placed to give the same current density as a conducting boundary would supply the equilibrium force; but, if the plasma moved and the currents in the wires did not change, the equilibrium would be unstable. If the wire currents are separately readjusted by feedback to keep the outer poloidal flux surface fixed, thus terminating the containing flux plot, then the equilibrium can be stable for a simple n = 0 plasma displacement. A conducting boundary, however, keeps the flux surface fixed for all manner of distortions. A network of fed-back conductors would be required to approach the stabilization of a conducting boundary.

In practice, a boundary of finite resistivity will suppress distortions at high frequencies and can be said to be in the shielding regime, while lower frequencies can be said to be in a leaking regime

where the current column flux plot slides through the shield and is ultimately terminated on the external primary wires. Hence, feedback for such wires, in combination with a resistive shield, can operate at conveniently lower frequencies. The resistance of the shield is chosen by judging what frequencies one wants to delegate to the feedback system.

In the case of the MST experiment, shields alone can be used for the time expected, with the plasma being always in the shielded phase, or a variety of resistive shields of short time-constant can be added to examine different frequency responses and plasma behavior.

The use of any shield which operates in the high frequency regime for the ohmic heating voltage or for field programming requires voltage gaps; and such gaps, whether poloidal or toroidal, require design to minimize their perturbations on the plasma. Tokamaks, such as the TFCX design, have such low loop voltages (corresponding to slow startup) that no gaps are necessary; but RFPs typically require high frequencies. Shield and gap design information which have used is given below.

If there must be a voltage induced in the plasma, then a flux linkage and its additional transformer action coils must be supplied. These coils and their flux leakage must be separated from the OH coils so a perturbing field is not created within the controlled flux plot within the plasma column walls.

B. Errors Due to the Iron Core

Iron for such a transformer can be incorporated so that it makes no perturbation. If we succeed in making the "primary" or OH winding current with its shield and feedback exactly cancel the plasma current so there is no flux plot external to the plasma chamber, then nearby iron surfaces will not be excited by plasma motion, and thus they can produce no perturbing field. However, since the iron (or an air core flux region) must be driven to provide the flux linkage for the loop voltage, its exciting winding must be placed on the iron exactly where the magnetizing ampere turns are required (to confine the magnetomotive force found within the iron body). This properly placed exciting winding then produces no field external to the iron (or air core region) which might perturb the plasma volume. This central core flux produces only a curl-free vector potential at the plasma, $A = \frac{\psi}{2\pi R}$, with $\nabla \times \vec{A} = \vec{B} = 0$ since 1/R has zero curl; and it produces the loop voltage $V_\ell = \int E d\ell = -\int \frac{\partial A}{\partial t} d\ell = -\frac{d\psi}{dt}$. Since the flux linkage is time-varying, split copper shields over the iron core can be used to transpose misplaced magnetizing wires where necessary. However, two cases remain:

1) Butt joint air gaps in the core require extra ampere turns which are supplied by a bundle of extra wires or a split copper shield; or, if the plasma chamber has a sufficiently thick shield with treated gaps, the shield will protect the plasma from stray pulsed flux with the shielding currents running on the outside of the chamber.

2) If dc bias is used, the dc bias wires must be placed where the magnetizing ampere turns are required on the iron. Otherwise fringing flux will stray into the plasma chamber, and this dc perturbation cannot be shielded by a conducting boundary. Extra turns are needed at the iron butt joints.

To ensure that there is no field between the core area and the confinement volume, "flux forcing" can be used. This is in principle merely connecting the plasma primary OH coil in parallel with the core magnetizing winding of an equal number of turns. Then the voltage on the core magnetizing winding equals the voltage on the plasma primary winding. Thus (since $I_{plasma} = NI_{OH}$):

$$N\Psi_{CORE} + I_{MAG}\, R_{MAG} = N\Psi_{LOOP} + \frac{I_{PLASMA}}{N} R_{OH\ COIL}$$

and

$$\Psi_{CORE} = \Psi_{LOOP\ AT\ PLASMA} + \int \left(\frac{I_P\, R_{OH}}{N} - I_{MAG}\, R_{MAG}\right)dt$$

and the core flux is completely separated from the region between the plasma chamber exterior and the core winding, and to the extent that $\int (I_P\, R_{OH}/N - I_{MAG}\, R_{MAG})dt = 0$ there is no field present outside the plasma boundary to intrude as a perturbation.

These field controlling techniques were fully exercised and perfected on the 350 ton iron core of the University of Illinois 300 MeV betatron, with 1.4 tesla dc bias within the iron creating no field perturbation in the transformer window larger than 10 percent of

the earth's field. This is the pulsed, biased core Dr. James Tuck of Los Alamos coveted at one time for a large upgrade of pinch devices.

In practice, the chamber shield with plasma will help stop external pulsed perturbations.

Proper treatment of the vertical field coils above and below the plasma is to backwind the ampere-turns where they pass under the iron return yoke to remove most magnetomotive force where the vertical field is returned through low reluctance iron.

C. Errors Due to Shell Gaps

When an isolated wall (shell) in the shielding phase is inserted into the vacuum tank attached to its toroidal current drive and to its toroidal field drive, the shell too must have toroidal and poloidal gaps. These shells have an external surface current to terminate the inner tank wall current's flux plot, and the shell's external current stream lines go over the gap rim and travel back on the inner surface of the shell where they terminate the flux plot due to the plasma current. If the flux plots inside and outside the shell match at the poloidal gap (current densities inside and immediately outside are equal), then current stream lines pass radially (minor) across the shell gap rim without generating a radial perturbing field component. If the inner and outer flux plots do not match at a gap, a perturbing field is driven through the gap by the currents running around the rim. Since these mismatches are expected, we shield the gaps of the floating shells, when necessary, to minimize the field perturbation. However, with two median plane toroidal gaps plus a poloidal gap interrupting the toroidal current a new type of perturbation occurs. A vertical

plasma displacement is driven farther by a transverse perturbing field entering one gap and leaving the other. This is one of the several cases of poloidal-toroidal gap interactions which must be recognized and treated. The perturbation cannot fully destabilize the vertical position; but it weakens the wall restoring force, and the wall restoring force dies out quickly because the necessary horizontal field lines soak edgewise into the shell. The results can be summarized as follows: A second shell or lamination nested with the first one, but with its toroidal gaps at the top or bottom instead, will take care of either vertical or radial displacement of the plasma column. The shell would relax with a characteristic time of 260 milliseconds, for a 5 cm wall example. For a horizontal displacement, midplane gaps do not inhibit the wall currents from generating an effective vertical restoring field. Thus, the nested shells stabilize both components of a plasma displacement.

In these cases where lines of force pass through a gap and soak into the conductor, thereby opening the gap wider and thus increasing the perturbing flux which passes through, it is found that the lines ultimately soak into the gap rim at a speed 2.2 times the speed with which they soak into either surface of the shield. The determination of these speeds from which a variety of shield configuration time constants can be derived are discussed in the next section.

Uniform dynamo effect reversing the toroidal field would cause only orthogonal stream lines and no field error. However, helical distortions or sinuous distortions of the current column would send flux in and out along the toroidal gap. This has the effect of forcing the plasma toward the slot with an equivalent vertical field of

$B_V \leq \frac{I}{10\pi r_0} \frac{G}{d}$ (amps, cm, gauss) where G is the gap width, r_0 is the chamber minor radius, and d is the wall thickness for a no-flange shell or $d \sim \frac{\pi R}{n}$ when there is a flange. The trouble is that without a flange this equivalent field can be larger than the variation of vertical field needed to position the discharge off the wall for a single slot and flange. The outer tank of the MST has a single slot, but there is a wide flange which helps.

It is conceivable that feedback current distribution control, as mentioned for the poloidal gap, may be applicable on the toroidal gap as well.

D. Field Diffusion Through Shields from the Point of View of Field Line Speed

A field applied to a surface as a step function of time diffuses inward. For finite shield thickness, d, the solutions of internal field strength as a function of depth, speed with which the applied flux plot moves into the shield, final limiting speed of entry, rate at which flux emerges from the back of the shield into the shielded region, and the extent of the applied flux plot which has moved into the shield have been derived. The result is shown in Fig. A.III.1. Complicated time dependences can be composed of step functions.

There is what might be called a shielding phase at early times, when flux is moving into the shield, but very little has leaked through, and a leaking phase when flux leaks past the shield at about the same rate as flux enters. This approaches a limiting speed at late times. In terms of the dimensionless time, τ, defined in the figure,

the shield phase occurs for $\tau < 0.1$ or 0.2, while the leaking phase would be for $\tau > 0.2$ or 0.3.

The limiting speed of field line entry in the leaking phase in cgs units is: $V_L = 10^9\rho/(4\pi\mu_R d) = 48$ cm/sec. The entering speed in the shielding phase is $V = 5000(\rho/[\mu_R t])^{1/2} = 8.7/\sqrt{t(\text{sec})}$ cm/sec. The extent of the flux plot which has moved into shield surface (flux influx) is $\Delta X = 48\ t(\text{sec}) + 1.7$ cm in the leak phase, and $\Delta X = 17.3\sqrt{t}$ cm in the shielding phase. The flux rate emerging from the back of the shield (after $\tau = 0.1$) is $\frac{d\Psi}{dt} \simeq B_0(2V_L - V)$. This latter parameter, when read off the curve for early times, will tell how responsive an external pickup coil of given sensitivity will be through a shield.

Another example of the application of field line speed to time constants of certain configurations is for imposing or changing an external vertical positioning field through a shield (or the inverse problem of how long will a shield hold the self generated stabilizing vertical field due to a displaced plasma column).

The rate at which applied field lines pass into a cylindrical wall from the outside where $B = 2B_o$, with B_o the applied vertical field, is (per unit length) $\frac{d\Phi}{dt} = 2B_oV_L$. Define a time constant, T, such that $T = \Phi/\frac{d\Phi}{dt} = \frac{B_o a}{2B_oV_L} = \frac{a}{2\times 48\ \text{cm/sec}} \simeq 0.3$ sec for our wall material and where Φ_o is the shield. Or in general using the limiting speed of a field line in terms of wall thickness, d, resistivity, ρ, we obtain $T = \frac{2\pi\mu_R ad}{10^9\rho}$. This agrees well with much more elaborate computations.

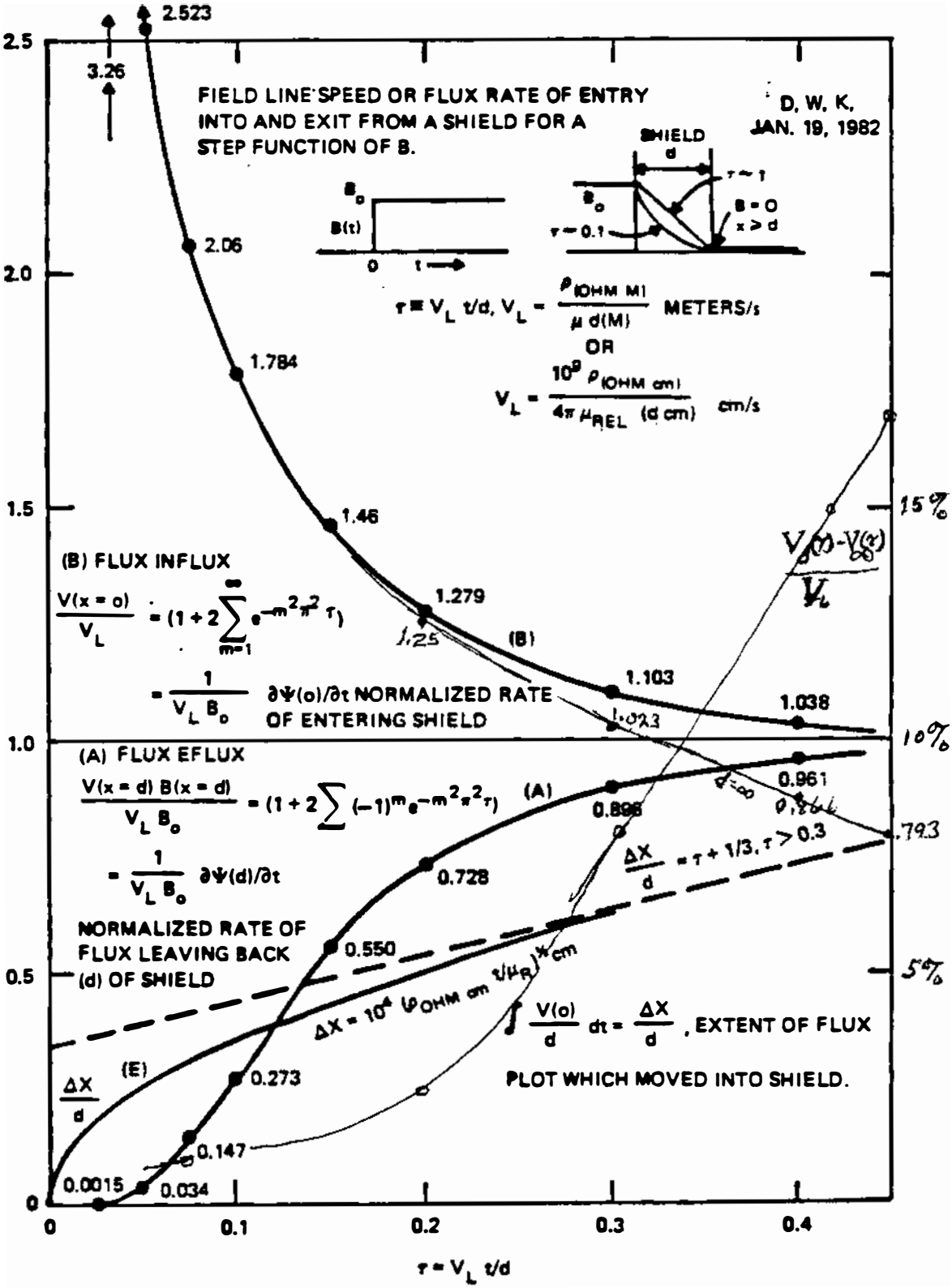

Fig. A.III.1

The ratio of field line speed to limiting field line speed (A) at the shielded side of A shield, (B) at the line entering side of shield for a field step function of time. (E) is the extent, Δx divided by shield thickness d, by which the driving flux plot's field lines have moved into the shield. (A) ≃ $1 - e^{-(5.7\tau)^2}$; (B) ≃ $(1 - e^{-9\tau})^{-1}$.

APPENDIX IV

RFP TESTS IN TOKAPOLE II AND LEVITATED OCTUPOLE

For about the past two years, experiments have been underway in which the RFP state has been transiently produced in Tokapole II and in the Levitated Octupole. Although these tests have been done in a non-circular, poloidal divertor configuration, they are of relevance to the MST design because they suggest the possibility of reaching the RFP state with relatively low gap voltage (~100 volts) with gaps inside the vacuum and in contact with the plasma. The Levitated Octupole tests also make use of the same capacitor banks and waveform programming capabilities that will be directly transferred to MST.

The earliest and most detailed experiments were done on Tokapole II, a small (R_o = 0.5 m) toroidal device which is normally operated as a poloidal divertor tokamak. For these studies the toroidal magnetic field is rapidly reversed shortly (~600 μsec) after the ohmic heating voltage is applied as shown in Fig. A.IV.1. The toroidal plasma current reaches a peak value of ~30 kA just before reversal occurs. This condition is achieved with a poloidal gap voltage of 170 volts, of which the plasma sees only 85 volts because the internal rings partially short-circuit the gap. The low-voltage startup is possible because of the application of 50 W of 2.45 GHz ECRH preionization which is resonant on an 800 gauss contour near the minor axis when the ohmic heating voltage is applied.

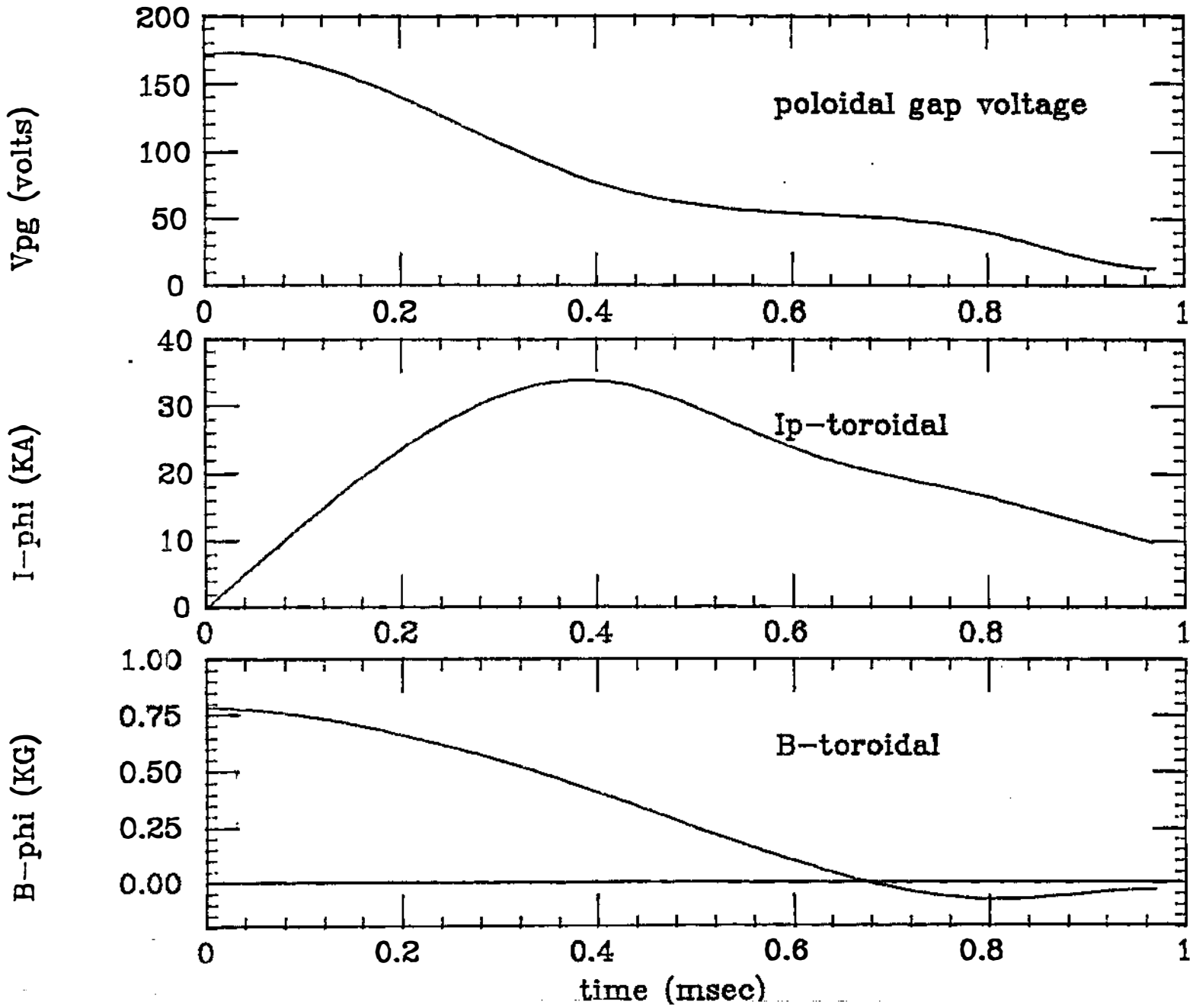

Fig. A.IV.1: Electrical waveforms in Tokapole II operated in an RFP mode.

Evidence for a reversed field state is provided by internal magnetic probe measurements. For example, Fig. A.IV.2 shows the local toroidal field vs minor radius for various times (640-760 μsec) near reversal. The substantial paramagnetic effect is evident, and it appears that a reversal surface is within the plasma for ~50 μsec. The failure of the reversed field state to sustain may have to do with the absence of a close-fitting, conducting boundary, but equally plausible is the rapid decay of the ohmic heating voltage and plasma current caused by the back-emf of the internal rings.

Over the past year, these experiments have been repeated on the Levitated Octupole with similar results as shown in Fig. A.IV.3. The gap voltage used was actually somewhat smaller (110 volts) and the plasma current higher (~50 kA), but the reversal would still persist for only ~100 μsec, for presumably the same reasons as in Tokapole II.

The internal rings have now been removed from the Levitated Octupole and better gap insulation added. We are thus in a position to begin tests in a large non-circular cross-section configuration with internal gaps similar to those proposed for MST. Eventually, during the construction of MST, the plan calls for installing smaller, optimized rings in the Octupole to obtain a test of an RFP with poloidal divertor.

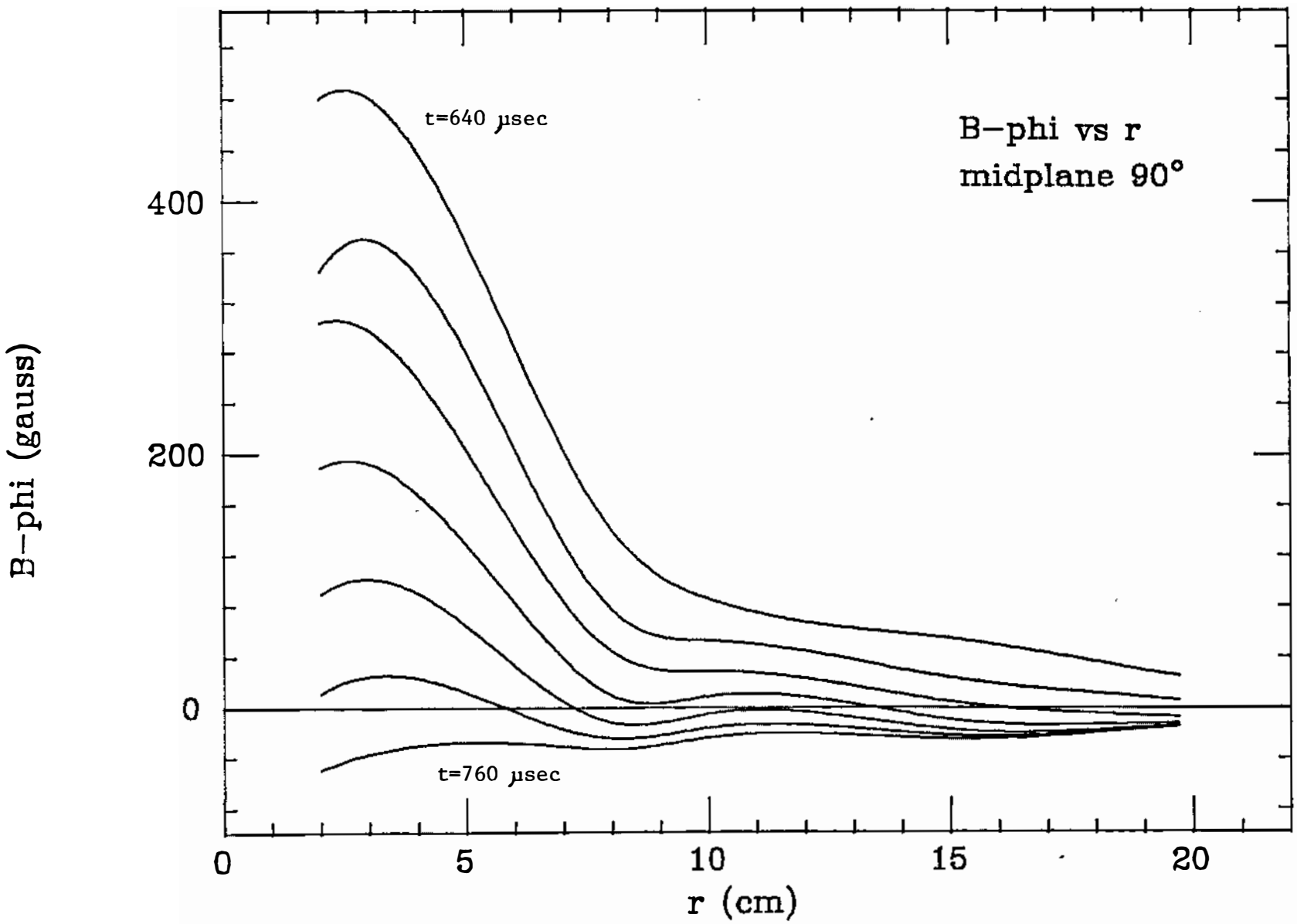

Fig. A.IV.2: Toroidal field profile from 640-760 μsec in 20 μsec intervals in Tokapole II obtained from magnetic probe measurements.

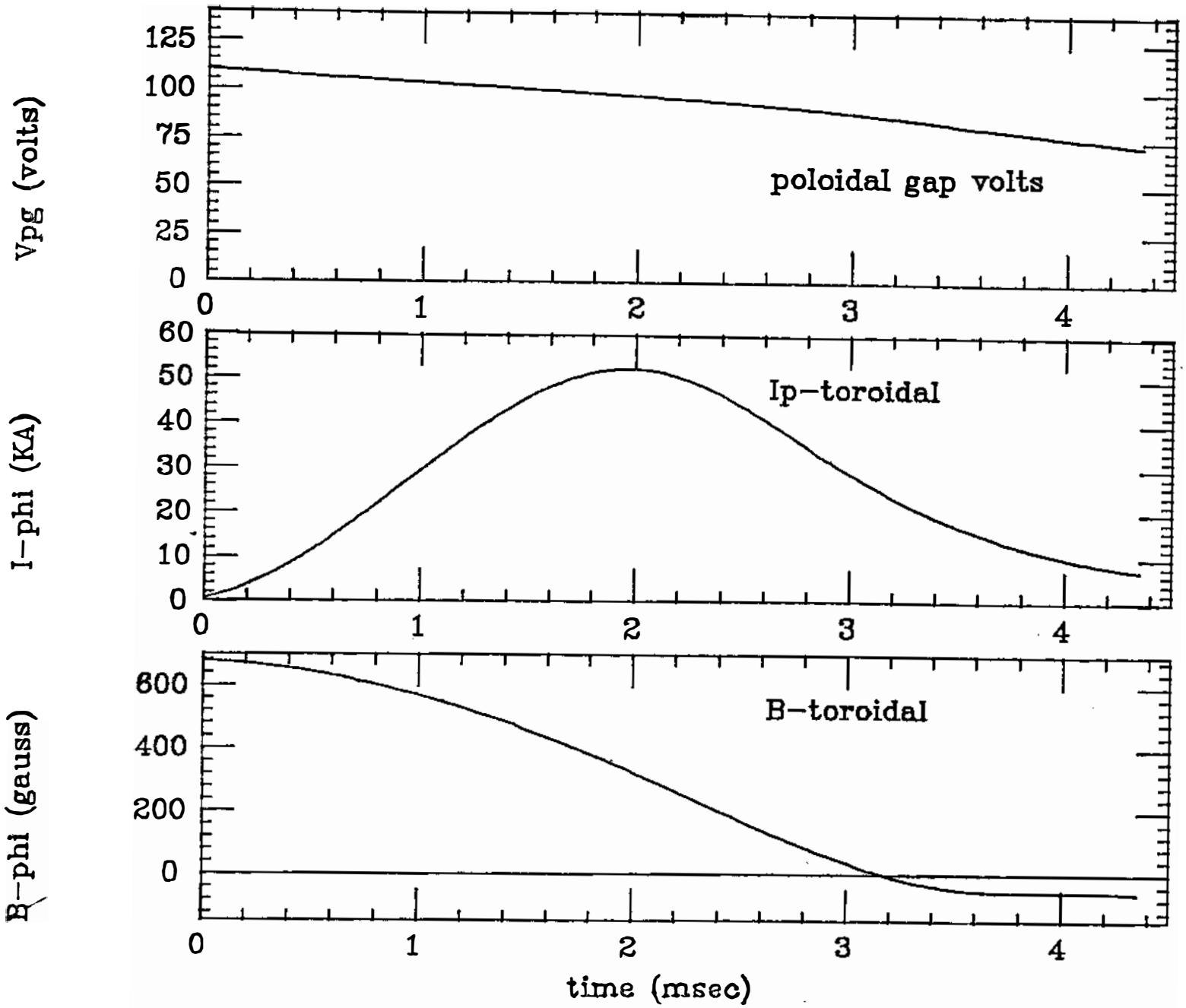

Fig. A.IV.3: Electrical waveforms in the Levitated Octupole operated in an RFP mode.